Distribution de cellules piézoélectriques semi-actives pour l'optimisation d'interfaces vibroacoustiquesDistributed shunted piezoelectric cells for vibroacoustical interfaces optimization

Flaviano Tateo

▶ To cite this version:

Flaviano Tateo. Distribution de cellules piézoélectriques semi-actives pour l'optimisation d'interfaces vibroacoustiquesDistributed shunted piezoelectric cells for vibroacoustical interfaces optimization. Génie mécanique [physics.class-ph]. Université de Franche-Comté, 2013. Français. <NNT : 2013BESA2011>. <tel-01068815>

HAL Id: tel-01068815

https://tel.archives-ouvertes.fr/tel-01068815

Submitted on 26 Sep 2014

SPIM

Thèse de Doctorat

école doctorale **sciences pour l'ingénieur et microtechniques**

UNIVERSITÉ DE FRANCHE-COMTÉ

DISTRIBUTED SHUNTED PIEZOELECTRIC CELLS FOR VIBROACOUSTIC INTERFACE OPTIMIZATION

Flaviano Tateo

SPIM

Thèse de Doctorat

école doctorale **sciences pour l'ingénieur et microtechniques**

UNIVERSITÉ DE FRANCHE-COMTÉ

Thèse présentée par

Flaviano Tateo

pour obtenir le

GRADE DE DOCTEUR

DE L'UNIVERSITÉ DE FRANCHE-COMTÉ

spécialité Mécanique

DISTRIBUTED SHUNTED PIEZOELECTRIC CELLS FOR VIBROACOUSTIC INTERFACE OPTIMIZATION

Soutenue le 19 Decembre 2013 devant la Commission d'Examen:

Rapporteurs	F. Scarpa	Professeur, ACCIS, University of Bristol
	J.-F. Deü	Professeur, LMSSC, le CNAM de Paris
Examinateurs	B. Troclet	Professeur, LMT, École Normale Supérieure de Cachan
	M.N. Ichchou	Professeur, LTDS, École Centrale de Lyon
	K.A. Cunefare	Professeur, IAL, Georgia Institute of Technology
Directeurs	M. Collet	Directeur de Recherche, LTDS, École Centrale de Lyon
	M. Ouisse	Professeur, FEMTO-ST, Université de Franche-Comté

Acknowledgements

I would like to express my gratitude to my advisor, Dr. Manuel Collet, for his support and sage guidance. A special thank is for Dr. Morvan Ouisse, for his invaluable support and constant enthusiasm which was critical to the completion of this work; Dr. Mohamed Ichchou for his thechnical and material support that allowed me to complete my experimental investigation and finally I would like to thank Dr. Kenneth A. Cunefare for his valuable help that allowed me to finalize this work.

I owe my parents and my all family, a debt of gratitude for their unceasing support and for letting me find my way even if it was far from them. I dedicate this thesis to Kathleen, who supported me throughout the thesis and finally Alberto a long-time friend.

I must thank all my current and former labmates for the beautiful time spent together both inside and outside the Femto-st laboratory.

Finally, I am grateful to all the Thesis committee members Dr. Fabrizio Scarpa, Dr. Jean-François Deü and Dr. Bernard Troclet for their time and insightful suggestions which were invaluable for the completion of this thesis.

Contents

List of Figures

List of Tables

Chapter 1

Introduction

1.1 Overview

The research investigates the design of a smart interface made of piezoelectric transducers arranged in a two-dimensional lattice. Each transducer is individually shunted to an external electric circuit synthesizing a negative capacitance effect. The proposed device find applications in the area of adaptive vibration suppression systems and smart materials. It allows to control waves propagating inside a structure taking advantage of the multi-field coupling between the structural plate and the electrical circuits shunting the piezoelectric patches.

The following sections have the purpose of presenting some basic ideas on vibration control and guided waves in complex media. After mentioning the context in which the work was conducted, motivations for the present study will be presented along with the research objectives and the contributions to the existing knowledge on this discipline. Finally, the chapter concludes with the organization of the research.

1.2 Background

1.2.1 Vibration Control

The design of innovative structures incorporating multiple physical functionalities represents a big challenge for both industrial and academic communities. Some examples of this new trend can be found in the aeronautic sector, where an intensive effort is made in order to integrate lightweight structures made of composite material. These composite structures bring new fatigue and damage risks, as well as vibration and acoustics problems. Thus, adding smart capabilities to integrated structural health monitoring systems and passive or active vibroacoustic control devices appears to be a viable solution to the problem.

To control complete structures, the classically adopted methodologies are based on the use of a small number of transducers and embedded electronics. For vibroacoustic applications (stabilization or isolation) such components can be easily designed and manufactured.

Over time, different passive solutions were proposed for both isolation and stabilization. The classical passive stabilizing solutions include, among others, the optimization of viscoelastic materials or the addition of tuned mass dampers.

Tuned mass damper is one of the most popular passive control devices used in many different engineering applications [75, 51]. The corresponding device is normally mounted onto a host structure to absorb the structural mechanical energy when the structure vibrates at its resonant frequency.

Passive damping technologies use viscoelastic elements to reduce the vibration of the structure, taking advantage of the dissipative mechanism within the viscoelastic material attached to the surface of the controlled structure [33].

These passive strategies have several advantages such as as the integrability, the effectiveness and the robustness. However, for some application this control strategy may be less interesting because of the narrow band efficacy (tuned mass dampers) or the necessity to introduce massive elements (damping materials or massive absorber) inside the considered structure. Moreover passive control strategies are not suitable for smart materials applications, these systems are unlikely to change their behavior in response to an external signal. In this case other strategies seem more appropriate, in the following of the chapter a brief review of these different methods is presented and analyzed.

Active vibration control

A widespread strategy is the active control technique where vibrations reduction is achieved, acting on mechanical actuators (force, inertial, strain) managed by a controller that process information delivered by a sensor (strain, acceleration, force) [81, 31, 74, 85].

These approaches have received increasing attention in the academic community and promising results have been reported using high performance piezoelectric actuators [67, 66, 37]. However, it is generally acknowledged that there is still a gap to be filled in order to make this technology more practical. This is due to global performance, robustness issues, complexity of the controller and energy cost of the system. [42, 9]

Semi-active vibration control

Piezoelectric shunt damping is an attractive semi-active technique employed to control vibrating structures; in fact, this technique offers a simpler and more cost-effective solution to drive piezoelectric transducers if compared to the fully active solution [29, 32]. Contrary to active control strategies, the key feature is the potential for using a passive electrical network directly connected to the electrodes of the piezoelectric element. As such, no error sensing device is required and the stability of the coupled system can be easier to achieve. Furthermore, shunted piezoelectric systems offer a very attractive feature; that is, the possibility of the integration and distribution of several electromechanical devices on the hosting structure.

Numerous works have been published [72] that present analyses of the capability and efficiency of a single shunted piezoelectric patch for structural stabilization and wave cancellation. An elegant formulation of passive shunting was first proposed by Hagood and Von Flotow [45] and is still commonly used. The study showed how a piezoelectric material shunted through a series RL circuit, i.e., a resonant shunt, which exhibited a behavior very similar to the well-known mechanical tuned mass absorber. A resonant shunt is simple to design and it offers effective damping in the vicinity of a selected mode of the underlying structure.

Since the initial introduction of single-mode resonant shunts, more complex shunting circuits have been investigated for suppressing multiple structural modes. Hollkamp [46] was able to suppress two modes of a cantilever beam using a system of RLC circuits connected in parallel. The whole circuit requires as many parallel branches as there are modes to be controlled. Since no closed-form tuning solution is available for determining the component values, the method relies on the numerical optimization of a nonlinear objective function fully parametrized by all of the circuit elements. The complexity of the circuit topology greatly increases as the number of modes to be simultaneously damped increases. More recently, the current-flowing concept was presented by Behrens et al. [12]. Compared to current-blocking schemes, the current-flowing method is easier to tune and involves less electrical components; however, it appears less effective for densely-spaced modes [70].

In addition to the RL-based shunting techniques described so far, other different strategies are available for multi-mode vibration reduction with piezoelectric shunts. One of the most effective method is based on the use of negative capacitance shunts, as originally proposed by Forward [40]. In this configuration, a piezoelectric patch is shunted through a passive circuit to a negative impedance converter. In this way, the internal capacitance of the piezoelectric ceramic is artificially canceled and the impedance of the shunt circuit reduces to that of the passive circuit. Optimization of the electrical impedance for modal damping is well described in [59]. Although the negative capacitance shunting strategy has been experimentally validated, it must be used with caution since it requires active elements that can destabilize the structure if improperly tuned. In order to achieve best performance, the circuit should be tuned very close to the stability limit [41, 54].

Nonetheless, these different solutions have proven to be efficient only in particular cases and may lack sufficient robustness for practical application. To successfully control structural or acoustic properties, these different solutions require increased complexity in terms of wiring, electronics, controllers and modifications of the baseline structure. Hence, among the problems to be considered, the broadband nature (from the low frequency LF up to the high frequency HF and including the mid frequency MF range) of vibration and noise associated with composite structures and their assembly is still a pending and challenging concern.

1.2.2 Wave Propagation in Periodic Media

Periodic media are defined as heterogeneous domains characterized by a recursive pattern obtained through the translation in space of a fundamental unit cell.

Figure 1.1 illustrates some examples of periodic structures: the Alhambra mosaics (left) and a bees honeycomb (right), two interesting examples of human and nature ability.

Extensive research is devoted to the analysis and design of periodic structures for wave management applications [57, 18]. Such assemblies may exhibit interesting wave propagation properties such as bandgaps [68, 69], response directionality [78, 79] and so-called negative acoustic

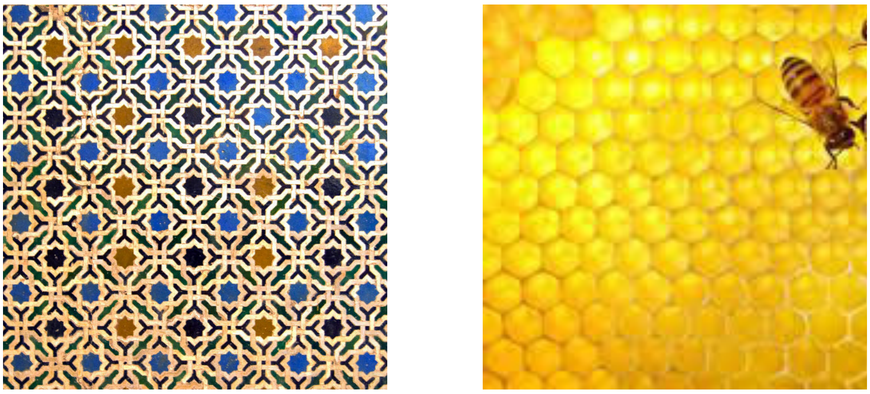

Figure 1.1: Examples of periodic media.

refraction [83, 73, 84]. The application of such concepts to the design of filters, waveguides, logic ports and ultrasonic transducer arrays can, for example, be used to perform a variety of acoustics-based signal processing functions.

In conjunction to telecommunication and signal processing, potential implications of the acoustic wave guiding technology include among others active sensing of structural integrity and vibration control [80].

Other novel structural configurations may be exploited for devices which exhibit acoustic super-lensing, super-focusing or cloaking characteristics [35, 89].

In the field of light propagation, several efforts were made in order to design and construct photonic crystals showing band gaps that prevent light from propagating in certain directions with specified frequencies. Many other efforts were made in order to create photonic crystal able to propagate light in anomalous and useful ways (i.e. negative refraction and artificial magnetism). In the acoustic domain, similar studies were carried out with the aim of preventing the propagation of elastic waves within the medium. In both cases, the band gap is obtained by periodically modulating some electromagnetic or mechanical properties [90, 56].

This technique, based on the theory of periodic structures, presents two characteristics:

- the spatial modulation must be of the same order as the wavelength in the gap;
- the position of the band gap cannot be easily changed since it strongly depends on the materials involved (Bragg's band gap).

A possible solution to overcome these physical limitations is found using composites with locally resonant units. The periodicity of the crystal creates a stop band that can be shifted by modifying the properties of the resonators. Liu et al. [58] have shown that a resonant sonic crystal with building blocks of rubber-coated lead balls exhibits a low-frequency sonic band gap, and the resonance can provide a maximum impedance mismatch to shield the airborne sound. The same effect can be obtained using Helmoltz resonators as shown by Fang et al. [34, 5] or Hu [48].

1.2.3 Programming the Matter

Piezoelectric patches and periodic structures thus seem to be good candidates for a novel class of intelligent materials able to modify their properties according to an external stimulus.

For example an adaptive metacomposites can be designed to create local resonances by coupling piezoelectric patches to a resonant external circuit, as illustrated in [86]. This concept involves a periodic array of simple RL-shunted piezoelectric transducers mounted on the structure to passively control the propagation of elastic waves and the subsequent vibration field. Periodically induced impedance-mismatch zones generate broader stop bands, i.e., frequency bands where waves are attenuated. The tunable characteristics of shunted piezoelectric patches allow the equivalent mechanical impedance of the structure to be tuned so that stop bands are generated over desired frequency ranges. The presence of a resistance in the shunt circuit generates a damped resonance of the electrical network. The resistance also allows the energy dissipation mechanism of shunted piezoelectric ceramics to be exploited, which dampens the amplitude of vibration also outside the stop bands. The original periodic shunting concept was numerically demonstrated on rods and fluid-loaded axisymmetric shells in [87]. More recently, this strategy was extended to flat plates [21, 82, 24], where the Bloch theorem was used to predict the dispersion properties of the resulting periodic assembly. It is therefore clear that shunted piezoelectric materials, employed simultaneously with electronic components and controllers can achieve new functionalities, such as adaptive vibration control. The aforementioned examples delineate an important feature: the possibility to programming the matter in order to attain more desirable properties. More specifically, the notion of programmable matter addressed by Toffoli [88] is extended to vibroacoustic programming problems.

1.3 Motivations

The vibrations suppression techniques presented in the previous sections using piezoelectric actuator is a mature technology although the integration of the control feedback responsible for a sharp enhancement of the overall performances is still a challenging aspect. Having said that it is clear that a suitable mathematical method is required in order to correctly design such a complex systems. Moreover the theoretical outcomes must be verified through experimental evidence so as to show the performances and the limitation of the real system. In the following subsection these two aspects are further analyzed.

1.3.1 The Necessity of a Suitable Theoretical Framework

For the study of wave propagation in complex media suitable mathematical models must be conceived in order to correctly describe these phenomena in the low frequency and the mid frequency range. The two most popular numerical approaches that can be distinguished for computing dispersion are the Semi-Analytical Finite Element method (SAFE) [8, 61, 22] and the Wave Finite Element (WFE) method [52, 49, 17].

In the former approach, the displacement field is modeled exactly in the direction of wave propagation by using a harmonic function and approximately in the directions perpendicular by using finite elements. An eigenvalue problem is then formulated by introducing the displacement field into the governing equations. Solving the eigenvalue problem for a given frequency gives the wave numbers of all the propagating modes. The main disadvantage of the SAFE method is that FE used are not standard so they must be specifically defined for each application.

As an alternative, the WFE method can be considered. By using the periodic structure theory introduced by Mead [63], an eigenvalue problem can be formulated from the stiffness and mass matrices of the FE model to find wave numbers of all the propagating waves. Contrary to SAFE method, the displacement field is approximated in the direction of propagation. Thus, some numerical issues can arise when the size of FE are too coarse. One of the main problems of these two approaches is the difficulty to deal with complex mechanical wave propagation specifically of multi-modal nature. Indeed, the existence at each frequency step of a number of wave-modes that potentially exchange energy make the computation and characterization of wave attenuation a delicate task.

One of the aims of this research is, indeed, to provide a numerical tool for computing wave dispersion in two-dimensional periodic systems incorporating damping and/or active devices (visco-poro-elastic materials, controlling electronics devices, etc). A suitable numerical formulation is introduced for computing the multi-modal damped wave numbers in the whole first Brillouin domain of periodical multi-dimensional structures with non homogeneous and generic frequency dependent damping terms.

1.3.2 Design and integration of a distributed adaptive metacomposite

In literature it is possible to find several articles devoted to the study of these type of systems. Just to cite a few, we can mention the work of Beck [11] performed on a cantilever shunted to an active circuit (negative capacitance shunt), which can control broadband flexural vibrations. Two different configurations have been taken into account: single and periodic arrays of shunted piezoelectric elements. The main outcomes are the capacity of the smart beam to dampen or selectively filter the incoming waves in a mono-dimensional waveguide.

Similar results were obtained by Airoldi [2, 3] on a beam equipped with periodic piezoelectric patches shunted to a resonant circuit. The configuration considered encompasses a beam undergoing longitudinal and transverse motion, and a periodic array of piezoelectric patches with electrodes connected to a resonant electric circuit. The resulting acousto-electrical system is characterized by an internal resonant behavior that occurs at the tuning frequency of the shunting circuits and is analogous in its operation to other internally resonating systems previously proposed, with the addition of its simple tunability, which makes this system a real example of one-dimensional metacomposite.

The two concepts were finally merged in the work of Casadei [21] where a periodic array of hybrid shunted piezoelectric actuators are used to suppress vibrations in an aluminum plate. Commonly, piezoelectric shunted networks are used for individual mode control, through tuned, resonant RLC circuits, and for broad-band vibration attenuation, through negative impedance converters. Periodically placed resonant shunts allow broadband reduction resulting from the attenuation of propagating waves in frequency bands which are defined by the spatial periodicity of the array and by the shunting parameters considered on the circuit. Such attenuation typically occurs at high frequencies, while negative capacitance circuits are effective in reducing the vibration amplitudes of the first modes of the structure providing broadband attenuation in the high frequency regimes and the reduction of the amplitudes of the low frequency modes.

An important goals is to show how would be possible to improve the performances of this type of systems considering a two-dimensional lattice of piezoelectric actuators arranged so as to form a truly active interface able to control the incident structural energy flows.

1.4 Objectives

The use of piezoelectric patches shunted to an external circuit, as mentioned before, is a widespread practice. In literature several design procedures have been proposed with the aim to qualify the most appropriate set of parameters fulfilling some specific criteria [26, 76].

The analyzed structure includes several actuators, it is clear that the study of wave propagation in such complex media requires a suitable mathematical models able to correctly describe these phenomena. This model, in order to provide meaningful results, must be able to take into account all the multiphysics couplings occurring between the structure and the control system.

Given the motivations above, the objectives of the thesis are:

- to formulate a strategy for the design of periodic lattice of piezoelectric actuators with inherent controlling capabilities;
- to validate the concept of control of structural energy flows through adaptive shunted piezoelectric metacomposites both numerically and experimentally;
- to prototype and test a novel composite structure.

To accomplish these objectives, the work first employs numerical methods to qualify and design the proposed vibration control strategy.

Next, prototyping of the smart metacomposite allows an experimental analysis that validates the numerical predictions and illustrates the real applicability of the proposed strategy in the industrial context.

1.5 Contributions

This work is a contribution to the challenges of designing and implementing a new class of integrated smart metacomposites capable of improved engineering performances in terms of mechanical and vibroacoustic behavior as compared to strictly passive structures.

The metacomposite structure of interest consists of an array of piezoelectric patches periodically arranged over a limited region of the surface of a two-dimensional waveguide. This array of patches is intended to serve as an active interface between regions of the waveguide, formed from a plate. This active interface allows modification of the scattering properties of the waveguide in terms of reflected and absorbed energy. This controlling capability is obtained by correctly tuning the parameters of the external circuit by which almost arbitrary effective structural impedance may be obtained. The selection of the electric component is made according to the methodologies developed by Collet et al. [26] and subsequently extended to more complicated cases involving fluid-structure interaction [27]. During the optimization procedure, the parameters are the real and the imaginary part of a generalized impedance. This procedure resulted in a quasi-constant resistance in series with a negative capacitance. The nominal values of these components are modified according to the criterion used during the optimization. Unlike the distributed resonant circuits, which are based on the energy exchange between the controlled structure and the resonant circuit, the negative capacitance circuit represents the optimal solution for controlling either energy velocity or wave absorption properties.

Experimental validation of this approach has been made on a beam [11] and subsequently extended to a flexible plate completely covered by piezoelectric patches [21]. The novelty of the manuscript at hand is to use an array of periodic shunted patches to create a controllable impedance boundary between an upstream and downstream section of the two-dimensional plate waveguide.

1.6 Organization of the work

The remainder of this work is organized into six sections included this introduction. The second chapter describe the design procedure used to characterize the smart interface using the Bloch theorem. The third chapter concern the prototyping and the manufacturing of the plate equipped with a finite array of piezoelectric patches and provides some recommendations about the implementation of the external shunt circuit. The fourth section describes the experimental procedures used to investigate the system and the related outcomes. The fifth chapter presents a numerical model able to describe the dynamical behavior of the finite-extent plate. Finally, the last chapter summarizes the major findings and provides recommendations for future investigations.

Chapter 2

Design of the Smart Interface

2.1 Overview

The present chapter details the analytical tools necessary to predict the wave dispersion in multi-dimensional periodic lattices.

A two-dimensional periodic lattice consists of unit cell that repeats itself indefinitely along two spatial coordinates. A number of physical systems are modeled as two-dimensional periodic structures as an example we can mention a simple bar grillage, a stiffened shell or graphene sheets at atomic level. A comprehensive approach to studying wave propagation in such periodic systems is provided by Brillouin [19].

In the present study the theory developed by Floquet for mono-dimensional structures and then extended by Bloch [13] in the case of multi-dimensional structures is adapted to a two-dimensional viscoelastic structure containing piezoelectric actuators and electronic components. This approach allows one to evaluate the wave dispersion of a periodic smart system incorporating complex frequency-dependent characteristics [26, 27].

This approach also allows one to estimate the wave directionality of the waveguide, in comparison to one-dimensional periodic structures, to completely characterize the wave propagation in two-dimensional case, one of the most important parameter to be considered is the propagation direction [79].

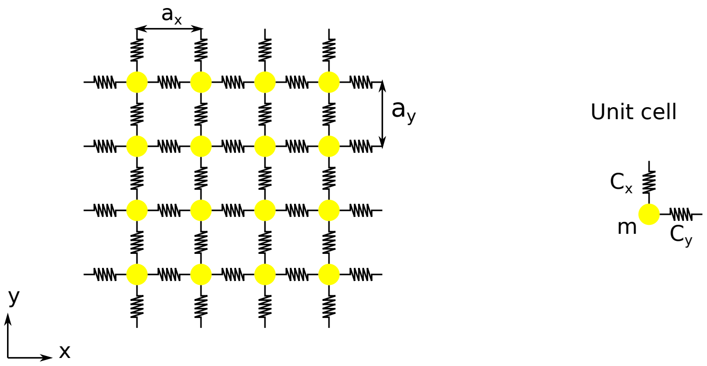

Figure 2.1: Two-dimensional periodic lattice of masses and springs.

2.2 Wave Propagation in a 2D Spring-mass System

In order to delineate some features related to the propagative properties of a two dimensional periodic structure let us consider the linear mono-atomic lattice shown in Figure 2.1. Such structure is modeled as an array of $p \times q$ equal masses interconnected by linear springs.

The out-of-plane displacement is the single degree of freedom describing the motion of each mass, so that the springs are assumed to act in shear with a force which is related to the relative displacements of neighboring masses. The equation of the harmonic motion of a representative unit cell can be expressed as:

$$-\omega^2 m u_{p,q} + (2C_x + 2C_y)\, u_{p,q} - C_x\,(u_{p+1,q} + u_{p-1,q}) - C_y\,(u_{p,q+1} + u_{p,q-1}) = 0 \tag{2.1}$$

where C_x is the spring stiffness between two adjacent masses m along x vector and C_y represent the spring stiffness along y direction. The direct and reciprocal lattice vector for the present lattice are given by

$$\begin{aligned} \vec{a} &= a\vec{i} + a\vec{j} \\ \vec{b} &= (2\pi/a)\,\vec{i} + (2\pi/a)\,\vec{j} \end{aligned} \tag{2.2}$$

where $\vec{i}$ and $\vec{i}$ denote the unit vectors along x and y axes. The term a represents the distance between two adjacent masses, we implicity assumed that the masse are placed at the same distance along Ox and Oy directions ($a_x = a_x = a$).

The provided example allows one to better understand the mechanism associated to the propagation of acoustic waves in such two-dimensional periodic structures. Moreover, it allows to better understand the characteristics and limitations of the mathematical approach classically used in this type of problem [57, 69].

2.2.1 Dispersion Relation

For the mass defined by the label p and q (Figure 2.1) we assume a solution of the form

$$u_{p,q}\left(\omega\right) = u_0\left(k\left(\omega\right)\right) e^{j\left(pk_x a_x i + qk_y a_y j\right)}. \tag{2.3}$$

For the adjacent masses the expected solution is slightly modified, according the following formula

$$u_{p\pm1,q\pm1}\left(\omega\right) = u_0\left(k\left(\omega\right)\right) e^{j\left((p\pm1)k_x a_x i + (q\pm1)k_y a_y j\right)}. \tag{2.4}$$

Equation (2.4) can be modified by means of the Euler's formulas

$$u_{p\pm1,q\pm1}\left(\omega\right) = u_0\left(k\left(\omega\right)\right) e^{j\left(pk_x a_x i + qk_y a_y j\right)} e^{j\left(\pm k_x a_x i + \pm k_y a_y j\right)}. \tag{2.5}$$

This manipulation allows to point out the relation between a given mass and the surrounding masses

$$u_{p\pm1,q\pm1}\left(\omega\right) = u_{p,q}\left(\omega\right) e^{j\left(\pm k_x a_x i + \pm k_y a_y j\right)}. \tag{2.6}$$

Substituting Equation (2.3) and (2.6) in Equation (2.1) we obtain

$$\left(\left(-\omega^2 m + 2C_x + 2C_y\right) - C_x\left(e^{-j(k_x a_x)} + e^{j(k_x a_x)}\right) - C_y\left(e^{-j(k_y a_y)} + e^{j(k_y a_y)}\right)\right) u_0 = 0. \tag{2.7}$$

Equation (2.7) can be further simplified to obtain

$$\left(-\omega^2 m + 2C_x\left(1 - \cos\left(k_x a_x\right)\right) + 2C_y\left(1 - \cos\left(k_y a_y\right)\right)\right) u_0\left(k_x, k_y\right) = 0. \tag{2.8}$$

This eigenvalue problem has a solution $u_0\left(k_x, k_y\right)$ different from zero providing that

$$-\omega^2 m + 2C_x\left(1 - \cos\left(k_x a_x\right)\right) + 2C_y\left(1 - \cos\left(k_y a_y\right)\right) = 0. \tag{2.9}$$

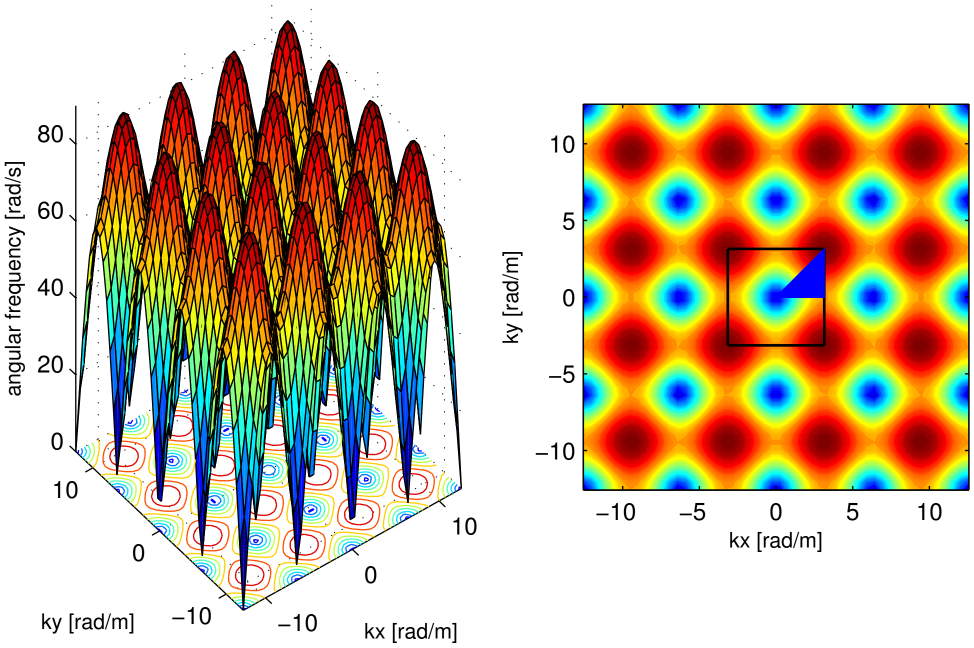

Figure 2.2: Dispersion relation for the two-dimensional periodic lattice.

Equation (2.9) clearly shows the existing relation between the angular frequency ω and the wave numbers k_x and k_y namely

$$\omega = \omega\left(k_x, k_y\right) = \pm\sqrt{\frac{2C_x\left(1-\cos\left(k_x a_x\right)\right)+2C_y\left(1-\cos\left(k_y a_y\right)\right)}{m}}. \tag{2.10}$$

Figure 2.2 represents the solution of equation (2.10), the results is presented in terms of a contour plot associating a color level with a frequency value. This structure and the associated solution exhibit discrete translational symmetry. That is, the solution is not invariant under translations of any distance, but rather, only distances that are a multiple of a fixed step length (Figure 2.2).

The basic step length is the lattice constant a in the direct lattice and $2\pi/a$ in the reciprocal lattice, the basic step vector is called the primitive lattice vector. Because of this discrete symmetry, the property $P\left(r\right)$ is equal to $P\left(r \pm a\right)$. By repeating this translation, we see that $P\left(r\right) = P\left(r + R\right)$ for any R that is an integer multiple of a.

The considered unit, which is repeated over and over, highlighted in Figure 2.2 with a box, is known as the unit cell. In this example, the unit cell is a portion of the periodic lattice containing one mass and a couple of springs. Because of the translational symmetries, the differential operator must commute with all of the translation operators in the x direction, as well as the translation operators for lattice vectors $R = ay$ in the y direction. We can begin to classify the modes by specifying k_x and k_y. However, not all values of k_i yield different eigenvalues. Consider two modes, one with wave vector k_i and the other with wave vector $k_i + 2\pi/a_i$. A quick insertion into (2.9) shows that they have the same eigenvalues. In fact, all of the modes with wave vectors of the form $k_i + p(2\pi/a)$, where p is an integer, form a degenerate set, they all have the same eigenvalue. Augmenting k_i by an integral multiple of $b = 2\pi/a$ leaves the state unchanged. We call $\vec{b} = b\vec{i}$ the primitive reciprocal lattice vector.

This crystals might have symmetries other than discrete translations. Suppose the operator (3×3 matrix) $R\,(n, \alpha)$ rotates vectors by an angle α about the n axis. If rotation by R leaves the system invariant, then we conclude that when there is rotational symmetry in the lattice, the frequency bands $\omega_n\,(k)$ have additional redundancies within the Brillouin zone. In a similar manner, we can show that whenever a crystal has a rotation, mirror-reflection or inversion symmetry, the $\omega_n\,(k)$ functions have that symmetry as well. This particular collection of symmetry operations (rotations, reflections, and inversions) is called the point group of the crystal.

Since the functions $\omega_n\,(k)$ possess the full symmetry of the point group, we need not consider them at every k point in the Brillouin zone. The smallest region within the Brillouin zone for which the $\omega_n\,(k)$ are not related by symmetry is called the irreducible Brillouin zone (shaded zone in Figure 2.2). For example, a crystal with the symmetry of a simple square lattice has a square Brillouin zone centered at $k = 0$, as depicted in Figure 2.2. The rest of the Brillouin zone consists of redundant copies of the irreducible zone.

In many occasions the study of the band structure of a crystal is reduced to the analysis of the solution in correspondence with the edges of the irreducible Brillouin zone. This is mainly due to the fact that the minima and the maxima of a given band (which determine the band gap) almost always occur at the zone edges and often at a corner. While this is not guaranteed, it is true in most cases of interest, such as all of the structures discussed in this chapter.

2.2.2 Group Velocity

The group velocity defines the way in which energy flows in the structure in response to an external perturbation. The group velocity c_g is defined as the gradient of the dispersion surface

$$c_g = \nabla\omega\left(k_x, k_y\right) \tag{2.11}$$

with $c_g = c_{g_x} i + c_{g_y} j$ where

$$c_{g_x} = \frac{\partial}{\partial k_x}\omega\left(k_x, k_y\right) \quad c_{g_y} = \frac{\partial}{\partial k_y}\omega\left(k_x, k_y\right). \tag{2.12}$$

The vector can be expressed in the reciprocal lattice space or Cartesian space and the gradient of the scalar dispersion relation results in a group velocity vector expressed in the same space. The dispersion relations for a 2D lattice can be represented as surfaces defining the frequencies associated with an assigned pair of wave vector components. Such surfaces can be represented as iso-frequency contours, which effectively visualize the group velocity as a vector perpendicular to each frequency contour for the considered pair [44, 1]. This representation is effective at identifying preferential directions of wave propagation, or the existence of forbidden directions along which waves do not propagate. Of particular interest is the existence of caustics, which are identified as cusps in the group velocity distributions of the kind observed in anisotropic media [7]. Such caustics are associated with strong energy focusing of the propagating wave packets, resulting from the interference of the various wave components propagating in the lattice plane. The group velocity pattern exhibited by the considered system is represented by the two components of the group velocity

$$\begin{aligned}
c_{g_x} &= \frac{a_x}{2}\frac{k_x/m\sin\left(k_x a_x\right)}{\sqrt{k_x/m\left(1-\cos\left(k_x a_x\right)\right)+k_y/m\left(1-\cos\left(k_y a_y\right)\right)}} \\
c_{g_y} &= \frac{a_y}{2}\frac{k_y/m\sin\left(k_y a_y\right)}{\sqrt{k_x/m\left(1-\cos\left(k_x a_x\right)\right)+k_y/m\left(1-\cos\left(k_y a_y\right)\right)}}.
\end{aligned} \tag{2.13}$$

It worth to point out that the group velocity represents also the velocity of energy flow. In the plane it is therefore possible to describe the direction dependent transport of energy within the

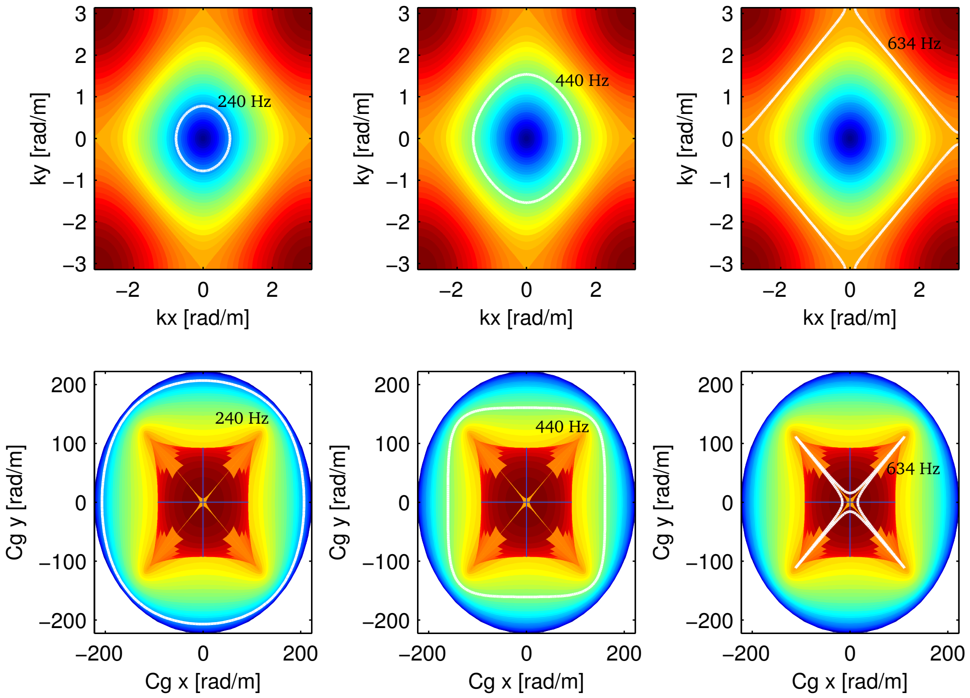

Figure 2.3: Dispersion relation and group velocity diagram for the two-dimensional periodic lattice: isotropic case.

waveguide in terms of the angle θ by

$$\tan\theta = \frac{a_x k_x \sin\left(k_x a_x\right)}{a_y k_y \sin\left(k_y a_y\right)}. \tag{2.14}$$

Moreover, the direction of energy flow at a given frequency and direction is orthogonal to iso-frequency contour. Propagation of waves may be strongly directional, waves propagate only in certain directions at specified frequencies. Under these conditions the associated energy is very focused although localized in a narrow frequency band.

Figure 2.3 depicts the dispersion relation of the two-dimensional periodic lattice along with its group velocity plot for wave-numbers belonging to the first Brillouin zone. For the case under consideration we have assumed that each mass is connected to two equally stiff springs arranged along the x and y direction. In the top of the figure the dispersion relation is expressed using the iso-frequency plots representation. A white line complete the plot highlighting the set of wave-numbers associated to the considered frequency. Comparing the shape of the white

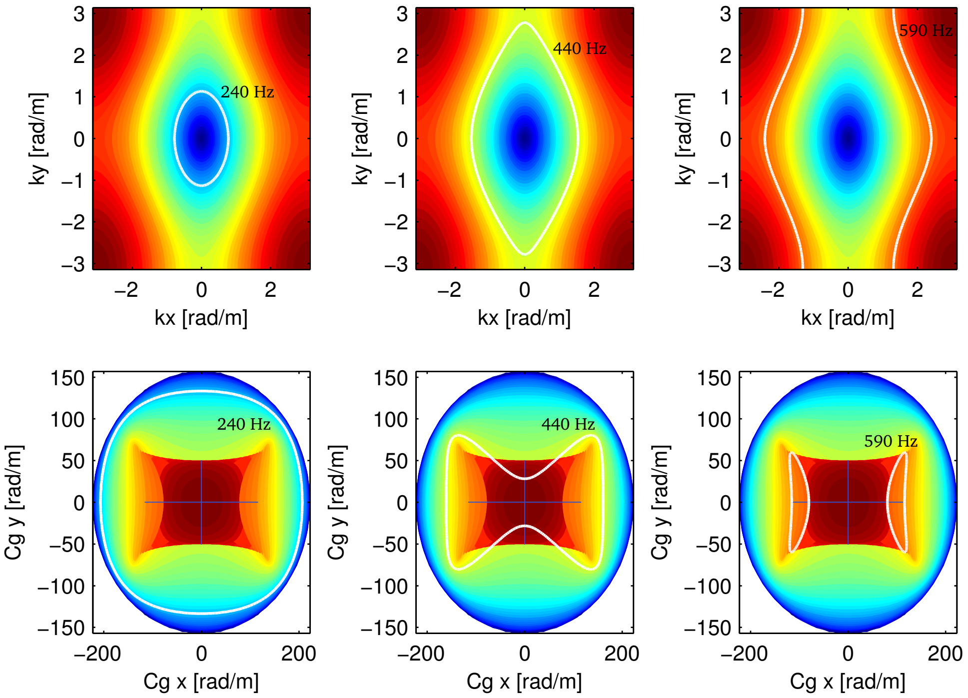

Figure 2.4: Dispersion relation and group velocity diagram for the two-dimensional periodic lattice: anisotropic case.

curve it is easy to understand that for particular frequency value the allowed wave-numbers lie along specific direction. The 240 Hz contour plot is almost isotropic (there are no preferred propagation directions), whereas at 642 Hz the propagation of the waves with wave-numbers components close to zero is completely forbidden both in the x and y direction (the white line splits in correspondence of the x and y axes). This behavior is further confirmed in the diagrams below in which the group velocity is expressed as a function of the group velocity c_{g_x} and c_{g_y}. At 642 Hz we observe a variation of the group velocity and therefore of the energy flow with the propagation direction, at this frequency the periodic lattice exhibits a strongly anisotropic behavior.

Figure 2.4 depicts the dispersion relation of the two-dimensional periodic lattice along with its group velocity plot for the anisotropic case where the stiffness along x direction is different from the stiffness along y direction. In the top of the figure the dispersion relation is expressed using the iso-frequency plots representation. The 240 Hz contour plot does not shows any band

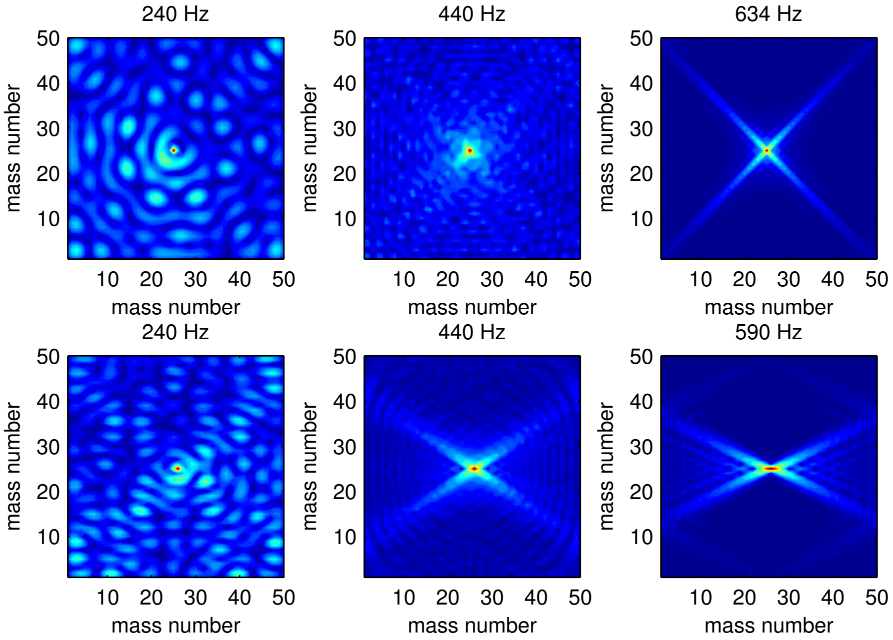

Figure 2.5: Harmonic response of two-dimensional spring mass system: isotropic lattice (top), anisotropic lattice (bottom).

gap, there are no preferred propagation directions. The system shows a behavior comparable with the isotropic case although the dispersion relation exhibits a more distorted shape. At 522 Hz the propagation of the waves in the y is completely forbidden (the white line separates in correspondence of a bigger range). This behavior is further confirmed in the diagrams below in which the group velocity is expressed as a function of the group velocity c_{g_x} and c_{g_y}. At 522 Hz we observe a variation of the group velocity and therefore of the energy flow with the propagation direction, at this frequency the periodic lattice shows regions where energy can not propagate at all along y direction.

This phenomenon can be illustrated calculating the harmonic response of the bounded periodic system formed by 50×50 lattice of punctual masses. The excitation is located at the center of the structure. Tuning the excitation source at 240 Hz we observe an out-of-plane displacement field almost isotropic. When the excitation frequency is increased up to 642 Hz the displacement field is strongly modified and the energy can exclusively flows in the two perpendicular directions oriented at 45 degrees with respect to the x axis. Of course, the direction of energy propagation can be modified acting on the stiffness of the structure as depicted in Figure 2.5.

2.3 The Bloch theorem

The example involving the simple spring-mass system introduces some important concepts related to the study of two-dimensional periodic systems. Unfortunately the described approach lacks of generality, the transition to the mathematical formulation including distributed media is not straightforward.

Keeping this in mind a different technique based on the Bloch theorem [60, 6] has been proposed. The well-known formulations of Bloch theorem [13] valid for two-dimensional systems governed by differential equations with periodic coefficients are here specifically revisited in light of their application to the analysis of damped periodic mechanical systems. Bloch theorem was originally introduced to represent the form of homogeneous states of Schrodinger equation with periodic potential. This theorem can be considered as a multidimensional application of the Floquet theorem [39], as indicated by Joannopoulos et al. [53]. For illustration purposes, we consider a medium whose generic property M satisfies the periodicity condition:

$$M\left(x + mR\right) = M\left(x\right) \tag{2.15}$$

where $m \in \mathbb{Z}^3$, and $R = [r_1, r_2, r_3] \in \mathbb{R}^{3\times3}$ is a matrix containing the three lattice vectors r_i. The primitive cell is defined as a convex polyhedron of $\mathbb{R}^3$ called Ω_R. The reciprocal unit cell, denoted by Ω_G is defined by the reciprocal lattice vector basis g_j for which the following holds:

$$r_i \cdot g_j = 2\pi\delta_{ij} \tag{2.16}$$

where δ_{ij} is the Kronecker symbol. $G = [g_1, g_2, g_3]$ is the reciprocal lattice matrix in the later. If Ω_R is the irreducible primitive cell, Ω_G corresponds to the first Brillouin zone of the lattice (see Kittel [55] for details).

The Bloch theorem stipulates that any functions $u(x)$ can be expressed as

$$u(x) = \int_{\Omega_G} \widehat{u}(x, k) e^{ik\cdot x} dk \tag{2.17}$$

where the Bloch amplitude $\widehat{u}(x,k)$ is Ω_G-periodic in k and can be represented as

$$\widehat{u}(x,k) = \sum_{n\in\mathbb{Z}^3} \widehat{u}(k+Gn)e^{iGn\cdot x} = \frac{\Omega_R}{(2\pi)^3}\sum_{n\in\mathbb{Z}^3} \widehat{u}(x+Rn)e^{-ik\cdot(x+Rn)} \tag{2.18}$$

where $\widehat{u}(x)$ stands for the Fourier transform of $u(x)$. It can also be demonstrated that the mean value of the Bloch amplitude is the Fourier amplitude of $u(x)$ for the corresponding wave vector

$$\langle u(.,k)\rangle_{\Omega_x} = \widehat{u}(k) \tag{2.19}$$

where $\langle u(.,k)\rangle_{\Omega_x}$ denotes for the spatial mean value computed on domain Ω_x.

The application of Bloch theorem for the representation of solutions of partial differential equations with periodic coefficients allows for all derivatives to be shifted by k in the sense given by the considered spatial operator. Consider for example the second order elliptic operator

$$\mathcal{A}(x) = -\sum_{p,q=1}^{N} \frac{\partial}{\partial x_p}\left(A_{pq}(x)\frac{\partial}{\partial x_q}\right) + W(x) \tag{2.20}$$

defined on smooth functions of $\mathbb{R}^N$ where $A_{pq}(x)$ is a symmetric, smooth and uniformly positive matrix with Ω_R-periodic coefficients. Indices p and q denote each basis vector of the considered $\mathbb{R}^N$ domain. $W(x) \geq 0$ is a real smooth function Ω_R-periodic. A spectral resolution of the closure of this operator can be found in $L^2(\mathbb{R}^N)$, and can be expressed in terms of Bloch waves associated with $\mathcal{A}(x)$.

Indeed, let $k \in \Omega_G$, and define

$$\mathcal{A}(x) = -\sum_{p,q=1}^{N} \left(\frac{\partial}{\partial x_p} + ik_p\right)\left(A_{pq}(x)\frac{\partial}{\partial x_q} + ik_q\right) + W(x). \tag{2.21}$$

The shifted cell eigenvalue problem is then considered:

$$\mathcal{A}(x)v_j(x,k) = \omega_j^2 v_j(x,k) \tag{2.22}$$

for $k \in \Omega_k$ with $v(x,k)$ in $H^1(\Omega_R)$ and Ω_R-periodic.

The essentially self-adjoint operator $\mathcal{A}(x)$ is non negative and the eigenvalue problem (2.22) has a discrete sequence of eigenvalues ω_j^2 whose corresponding eigenfunctions are the Bloch waves $v_j(x,k)$. These eigenvalues are smooth functions of x and are complete in $L^2(\Omega_R)$. More details in mathematical properties of this eigen-solution can be found in Bensoussan et al. [71] and Wilcox [23]. Based on these results, the Bloch expansion of any function $v_j(x,k)$ can be expressed as:

$$u(x) = \int_{\Omega_G} \sum_{j=1}^{+\infty} u_j(k) e^{ik\cdot x} v_j(x,k) dk \tag{2.23}$$

and

$$u_j(k) = \int_{\mathbb{R}^N} u(x) e^{-ik\cdot x} v_j^*(x,k) dx \tag{2.24}$$

where v_j^* is the complex conjugate of v_j. Moreover, Parseval identity holds

$$\int_{\mathbb{R}^N} |u(x)|^2 \, dx = \int_{\Omega G} \sum_{j=1}^{+\infty} |u_j(x)|^2 \, dx. \tag{2.25}$$

The spectral resolution of operator $\mathcal{A}(x)$ can also be expressed as:

$$\mathcal{A}(x)u(x) = \int_{\Omega_G} \sum_{j=1}^{+\infty} u_j(k) e^{ik\cdot x} \omega_j^2(k) v_j(x,k) dk \tag{2.26}$$

Examples of applications of these results can be found in Bensoussan et al. [71].
An original application to bidimensional viscoelastodynamic problem has been proposed recently by Collet et al. and extended to piezoelastodynamic problem [26]. This formulation leads to a very general numerical implementation for computing wave dispersion into periodically smart distributed mechanical systems incorporating electronic components, damping effects, or any frequency-dependent characteristics. The main ideas of the approach are described here, together with the specific points related to the inclusion of piezoelectric effects in the model.

2.3.1 Piezo-elastodynamic Formulation

Let us consider a piezoelastodynamic problem made of infinite periodic distribution of unitary cell described in Figure 2.6. The harmonic homogeneous dynamical equilibrium of system is

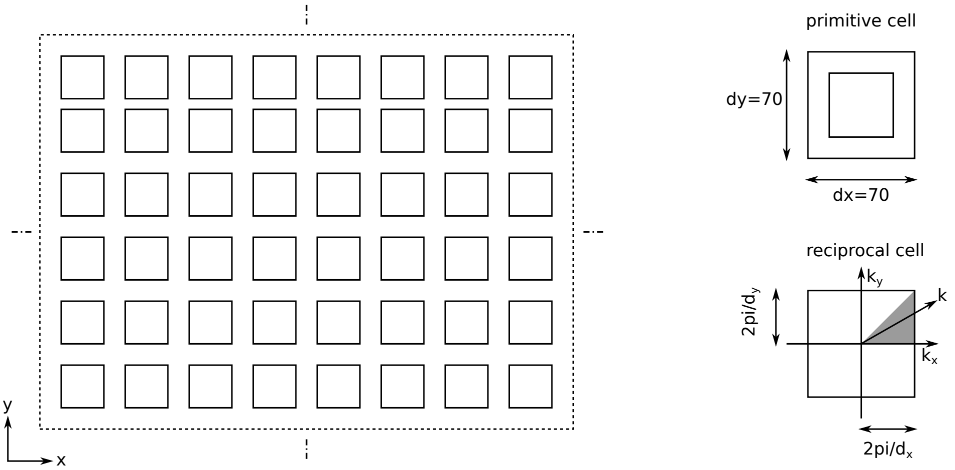

Figure 2.6: Generic 3D piezocomposite periodic cell.

driven by the following partial derivative equations

$$\begin{aligned} \rho\frac{\partial w}{\partial t^2} - \nabla \cdot \sigma = 0 \\ \nabla \cdot D = 0 \end{aligned} \tag{2.27}$$

where $w(x,t)$ is the displacement vector, ρ is the density, σ represents the Cauchy stress tensor, $\varepsilon = \nabla_s w$ the Green strain tensor, and $D\,(x,t)$ the electric displacement.

The linear constitutive material behavior relationships can be written as

$$\begin{aligned} \sigma = C_E\varepsilon - e^T E \\ D = e\varepsilon + \epsilon_S E \end{aligned} \tag{2.28}$$

where $E = -\nabla V$ is the electric field vector (V being the voltage), C_E the elasticity tensor at constant electrical field, e the piezoelectric coupling tensor and ϵ_S the dielectric permittivity at constant strain. We add to this set of equilibrium equations an output expression

$$q^0 = -\int_{S_t} D \cdot n dS \tag{2.29}$$

allowing the introduction of the charge measurement on the piezoelectric top electrode and hence the dual counterpart of the imposed electrical Dirichlet boundary condition for applying the shunt impedance operator. The equations above are consistent for each kind of material to the extent that null piezoelectric and permittivity tensors can be used when passive materials are considered. All these tensors also depend on the spatial location vector x and are Ω_x periodic. By applying a Fourier transformation, the piezoelastodynamic equilibrium can also be written as

$$\begin{gathered}\rho\frac{\partial w}{\partial t^2}-\nabla\cdot\Big(C_E\varepsilon+e^T\nabla V\Big)=0\\ \nabla\cdot(e\varepsilon-\epsilon_S\nabla V)=0.\end{gathered}\tag{2.30}$$

As the problem is 2D infinitely periodic, mechanical boundary conditions are included in the formulation, while electrostatic boundary conditions have to be considered on each cell

$$\begin{aligned}V&=0 &&\forall x\in S_b\\ V&=V^0 &&\forall x\in S_t\\ D\cdot n&=0 &&\forall x\in S_l\end{aligned}\tag{2.31}$$

where S_b is the grounded bottom electrode of the piezoelectric layer, S_t is the top electrode connected to the external shunt and S_l the lateral electrode. The top electrode applied feedback voltage V^0 depends on the shunt characteristic and on the collected charges q^0 given in equation (2.29) and can be expressed in the Fourier space by

$$V^0=-Zq^0\tag{2.32}$$

where Z defines the general impedance associated to the shunted electric circuit. Considering a primitive cell of the periodic problem Ω_x, the Bloch eigenmodes and the dispersion functions can be computed by searching the eigensolutions of the homogeneous problems (2.30) with mechanical periodic boundary conditions and electric ones given by equation (2.31) as

$$u(x)=\begin{bmatrix}w\\ V\end{bmatrix}=\begin{bmatrix}w_{n,k}\\ V_{n,k}\end{bmatrix}e^{ik\cdot x}=u_{n,k}e^{ik\cdot x}.\tag{2.33}$$

The vector $u_{n,k}$ contains the functions $w_{n,k}$ and $V_{n,k}$ which are periodic in Ω_x. By introducing expression (2.33) in the piezoelastodynamic equations (2.30), $w_{n,k}$ $V_{n,k}$ and ω_n can be found by solving the generalized eigenvalues problem

$$\begin{aligned}
&\rho\omega^2 w_n - \nabla\cdot\left(C_E\nabla_s w_n + e^T\nabla V_n\right) + \\
&ik\left(\left(C_E\nabla_s w_n\right)\cdot\Phi + \nabla\cdot\left(C_E\Xi_{n,k}\right)\right) + \\
&ik\left(\left(e^T\nabla V_n\right)\cdot\Phi + \nabla\cdot\left(e^T\nabla V_n\right)\cdot\Phi\right) + \\
&-k^2\left(\left(C_E\Xi_{n,k}\right)\cdot\Phi + \left(e^T\nabla V_n\cdot\Phi\right)\cdot\Phi\right) = 0
\end{aligned} \tag{2.34}$$

$$\begin{aligned}
&-\nabla\cdot\left(e\nabla_s w - \epsilon_S\nabla V\right) + \\
&-jk\left(\nabla\cdot\left(e\Xi_{n,k}\right) + \left(e\nabla_s w\right)\cdot\Phi\right) + \\
&+jk\left(\nabla\cdot\left(\epsilon_S\nabla V\right)\cdot\Phi + \left(\epsilon_S\nabla V\right)\cdot\Phi\right) + \\
&+k^2\left(\left(e\Xi_{n,k}\right)\cdot\Phi - \left(\epsilon_S\nabla V\cdot\Phi\right)\cdot\Phi\right) = 0
\end{aligned}$$

with the associated boundary conditions

$$\begin{array}{ll}
w_{n,k} = w_{n,k} & \forall x \in S_R, S_T \\
V_{n,k} = 0 & \forall x \in S_b \\
V^0_{n,k} = -Zq^0_{n,k} & \forall x \in S_t \\
D\cdot n = 0 & \forall x \in S_l.
\end{array} \tag{2.35}$$

In these equations

$$k = k\begin{bmatrix}\cos\theta \\ \sin\theta \\ 0\end{bmatrix} = k\Phi \tag{2.36}$$

where Φ represents the direction angles into the reciprocal 2D lattice domain and

$$\Xi_{n,k} = 1/2\left(w_{n,k}(x)\cdot\Phi^T + \Phi\cdot w^T_{n,k}(x)\right) \tag{2.37}$$

is the symmetric dyadic tensor or the dyadic, product of the displacement $w_{n,k}$ and direction vector Φ. S_r are the interfaces of the cells continuum and R is the matrix grouping the basis vectors of the two lattices.

In the electrical boundary conditions, $q_{n,k}^{0}$ is given by

$$q_{n,k}^{0} = -\int_{S_t} \left(\left(-e\nabla_s w + ik \right) \cdot ndS + \epsilon_S \nabla V ik \epsilon_S V \cdot \Phi \right) \cdot ndS \tag{2.38}$$

where n is the surface outpointing unitary normal vector.

The proposed formulation is then based on the computation of the Floquet vectors given in equations (2.34), instead of computing the Floquet propagators commonly used for elastodynamic applications. The full 2D wave dispersion functions can then be obtained, while damping and electrical impedances can clearly be introduced into the piezoelastodynamic operator. The adopted methodology allows the computation of the complete complex map of the dispersion curves incorporating computation of evanescent waves and allowing the introduction of damping and shunt operator if any.

Let us consider the partial derivative equations (2.34) on a unit cell Ω_x. It stands for a generalized eigenvalue problem leading to compute the dispersion functions ω_n and the corresponding Floquet eigenvectors $u_{n,k}$. For computing the 2D dispersion curves, we need to introduce a suitable weak formulation.

If $u_{n,k}$ is a solution of equations (2.34), then

$$\begin{aligned}
&\int_{\Omega} [\rho\omega^2 \delta w_{n,k} w_{n,k} - \left(\delta\varepsilon_{n,k} - jk\delta\varXi_{n,k}\right) C \left(\varepsilon_{n,k} + jk\varXi_{n,k}\right) + \\
&- \left(\delta\varepsilon_{n,k} - jk\delta\varXi_{n,k}\right) e^T \left(\nabla V_{n,k} + jkV_{n,k}\Phi\right) - \left(\nabla\delta V_{n,k} - jk\delta V_{n,k}\right) e \left(\varepsilon_{n,k} + jk\varXi_{n,k}\right) + \\
&- \left(\nabla\delta V_{n,k} - jk\delta V_{n,k}\Phi\right) \epsilon_S \left(\nabla V_{n,k} + jkV_{n,k}\Phi\right)] d\Omega - \frac{\delta V_{n,k} V_{n,k}}{Z} = 0
\end{aligned} \tag{2.39}$$

This weak formulation is simply obtained by integrating equations (2.34) projected onto any test function δu. The boundary integral vanishes as the test functions are chosen so that $\delta w(x - Rm) = \delta w(x)$ on S_r. For a polyhedron cell, each boundary is generally a polyhedral plane subdomain that can be associated with a parallel opposite one. The symmetry conditions called $\delta w(x - Rm) = \delta w(x)$ on S_r explicitly link these associated surfaces.

2.3.2 Numerical Computation

The numerical implementation is obtained by using a standard finite elements method to discretize the weak formulation. The assembled matrix equation is given by:

$$\left(K + \lambda L - \lambda^2 H - \omega_n^2 M\right) w_{n,k}\left(k, \Phi\right) = 0 \tag{2.40}$$

where $\lambda = ik$, M and K are respectively the standard symmetric definite mass and symmetric semi-definite stiffness matrices, L is a skew-symmetric matrix and H is a symmetric semi-definite positive matrix:

$$\begin{aligned} M &\leftarrow \int_{\Omega_R} \left(\rho \omega_n^2 \delta w_{n,k} w_{n,k}\right) d\Omega \\ K &\leftarrow \int_{\Omega_R} \left(\delta \varepsilon_{n,k} C \varepsilon_{n,k}\right) d\Omega \\ L &\leftarrow \int_{\Omega_R} \left(\delta \kappa_{n,k} C \varepsilon_{n,k} - \delta \varepsilon_{n,k} C \kappa_{n,k}\right) d\Omega \\ H &\leftarrow \int_{\Omega_R} \left(\delta \kappa_{n,k} C \kappa_{n,k}\right) d\Omega. \end{aligned} \tag{2.41}$$

When k and Φ are fixed, the system (2.41) is a linear eigenvalue problem allowing us to compute the dispersion functions ω^2 and the associated Bloch eigenvector $w_{n,k}$. This approach has been widely used for developing homogenization techniques and spectral asymptotic analyses like in the work of Allaire and Conca [4]. It can also be applied for computing wave's dispersion even if Floquet propagators are preferred for 1D or quasi 1D computation, as indicated by Ichchou et al. [52], Houillon et al. [47] or Mencik and Ichchou [64, 65]. Nevertheless these approaches have been only developed for undamped mechanical systems that is to say represented by a set of real matrices. In this case, most of the previously published works present techniques based on the mesh of a real k-space (i.e $\vec{k}$ or k and Φ) inside the first Brillouin zone for obtaining the corresponding frequency dispersion diagrams and the associated Floquet vectors. For undamped systems, only propagative or evanescent waves exist, corresponding to families of eigensolutions purely real or imaginary. Discrimination between each class of waves is easy in this case.

If a damped system is considered, that is to say if matrices K, L, H are complex, evanescent part of propagating waves appear as the imaginary part of ω comes very difficult to distinguish the two families of waves but also to compute the corresponding physical wave's displacements by applying spatial deconvolution.

Another possibility much more appropriate for computing damped system, dedicated for time-space deconvolution and for computation of diffusion properties as defined by Collet et al. [28] or Mencik and Ichchou [65], is to consider the following generalized eigenvalue problem:

$$\left(K + \lambda L - \lambda^2 H - \omega_n^2 M\right) w_{n,k}\left(\omega, \Phi\right) = 0. \tag{2.42}$$

In this problem, the angular frequency ω and the propagative angle Φ are fixed real parameters. Wave's numbers $\lambda_n = ik_n$ and associated Floquet vectors $w_{n,k}$ are then computed by solving the quadratic eigenproblem.

This approach allows introduction of frequency dependent matrices corresponding to generalized damping terms (viscoelasticity), multi-physic coupling (especially electromechanical with electronic ordinary differential equation), foam (Biot-Allard model).

Based on this approach, an inverse Fourier transformation in the k-space domain can lead us to evaluate the physical wave's displacements and energy diffusion operator when the periodic distribution is connected to another system, like in the work by Collet et al. [25]. Another temporal inverse Fourier transformation can furnish a way to access spatio-temporal response for non-homogeneous initial conditions. As L is skew-symmetric, the obtained eigen values are quadruple $(\lambda, \overline{\lambda}, -\lambda, -\overline{\lambda})$ collapsing into real k; or imaginary pairs (or a single zero) when all matrices are real (i.e. for an undamped system). In this case a real pair of eigenvalues correspond to evanescent modes oriented in two opposite directions on the k-space and imaginary values to two traveling waves propagating in opposite direction. The obtained eigensolutions are similar, in 1D for homogeneous material (non periodic), to those given by SAFE method and additional important properties can be extrapolated from Gavric [43].

As previously mentioned, the real part of $\vec{k} = k\Phi$ vector is restricted to stand inside the first Brillouin zone (see Fig. 2.6). In the quadratic eigen value problem (2.42) nothing restricts computation to only find eigen values satisfying this condition. For direction vector orthogonal to the lattice facelets, the periodical conditions expressed for one dimensional waveguide are still valid. Thus, for undamped systems, all obtained eigenvalues are periodically distributed in the k-space along its principal directions.

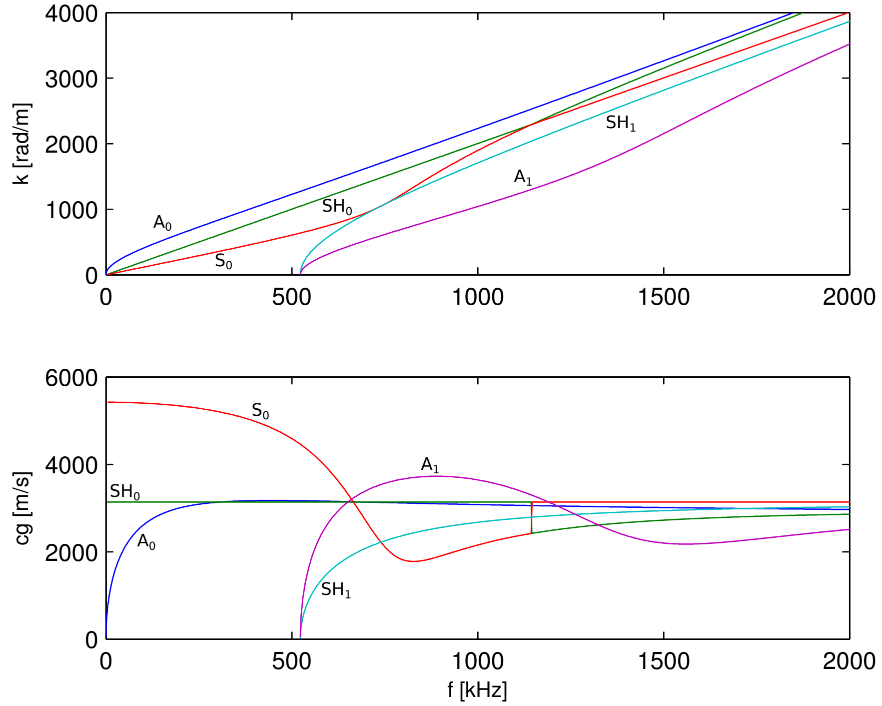

Figure 2.7: Lamb waves in an isotropic plate: dispersion relation (top), group velocity (bottom). Solution obtained using SAFE method.

2.4 Wave Dispersion in an Isotropic Plate

In order to verify the method and illustrate some features of the solution, an isotropic plate 3 mm thick with the following material properties: $\nu = 0.33$, $E = 70$ $[GPa]$, $\rho = 2700$ $[kg/m^3]$ has been considered. By using symmetry of the unit cell, the corresponding first Brillouin zone is described in Figure 2.6 where the irreducible zone is the shaded area. The method allows us to compute eigenfrequencies corresponding to any $\vec{k}$ vector described in cylindrical coordinates system by its radius k and its angle Φ.

Lamb waves are a type of ultrasonic waves that can be supported by this type of waveguide (two parallel free surfaces). Lamb waves can exist in two basic types, symmetric and antisymmetric. It will be shown that for each propagation type there exist a number of modes corresponding to the solutions of the Rayleigh-Lamb equation. The symmetric modes are designated as S_0, S_1, S_2 waves whereas the antisymmetric are designated as A_0, A_1, A_2 waves at these set of wave-modes we can add the shear wave-modes SH_0, SH_1, SH_2. The symmetric Lamb waves resemble the axial waves, whereas the antisymmetric Lamb waves resemble the flexural waves. Lamb waves are highly dispersive. Their characterization pass trough the solution of the Rayleigh-Lamb equation:

$$\frac{\omega^4}{c_T^4} = 4k^2q^2\left(1 - \frac{p}{q}\frac{\tan(ph+\alpha)}{\tan(qh+\alpha)}\right) \tag{2.43}$$

where p and q are defined as follows

$$p = \frac{\omega^2}{c_L^2} - k^2 \quad q = \frac{\omega^2}{c_T^2} - k^2. \tag{2.44}$$

The coefficient α allows one to select the solutions corresponding to the symmetric waves S ($\alpha = 0$) or anti-symmetric waves A ($\alpha = \pi/2$).

By using the SAFE method it is possible to calculate all the solutions of equation (2.43) for the bare plate. In Figure 2.7 the dispersion relation and the group velocity of the Lamb waves in the $0 - 2$ MHz. At low frequencies A_0, S_0, SH_0 modes exist, the higher order modes such as A_1 are originated far from the origin of the diagram, precisely above 500 kHz.

Figure 2.8 compares the dispersion relation obtained using the SAFE method and the solution obtained using the Bloch theorem. The two solution perfectly match over the entire frequency range.

The application of Bloch theorem is well justified since the infinite plate can be considered as a spatial repetition of a portion of itself. According to the size of the primitive cell a larger zone of the dispersion relation can be investigated. With the considered parameters, the first Brillouin zone lies approximately in the range of -100 and 100 rad/m.

The propagation characteristics of plane waves in an elastic solid may be found, for example, by considering the Christoffel equation [7]. A dispersion relation is then obtained solving the associated eigenvalue problem. At fixed ω we obtain a surface in the k-space that gives k as a function of its direction. This is called the wave vector surface. The wave vector is always proportional to the angular frequency ω it is therefore more convenient to consider the slowness surface which gives the inverse of the phase velocity k/ω as a function of propagation direction. This method easily apply to isotropic or anisotropic solids, by knowing the material constants of the crystal is therefore possible to calculate its directional properties.

However, this method no longer apply when more complex structures are considered. For example

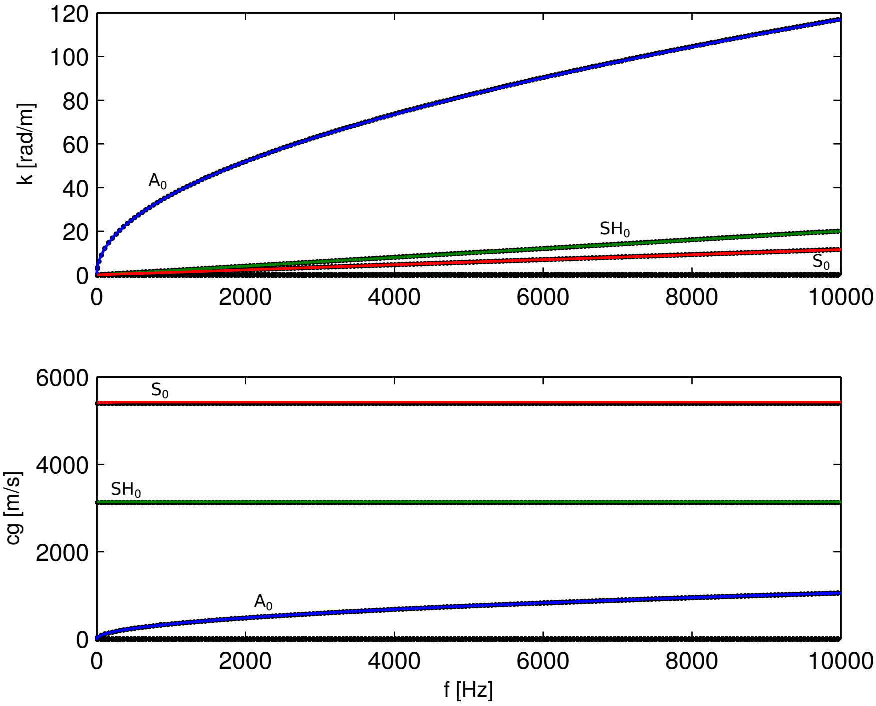

Figure 2.8: Lamb waves in an isotropic plate: dispersion relation (top), group velocity (bottom). SAFE (solid lines) and Bloch solutions (dots) are compared.

the effect of the control feedback on the directivity of the waveguide it difficult to estimate with this basic tool. On the other hand, using the Bloch theorem it is possible to retrieve the same information by simply calculating the velocity group c_g associated to each wavemode.

In Figure 2.9 the directivity diagram of c_g calculated using the Bloch theorem is compared to the analytical solution carried out using the slowness surface method. For the considered plate the circle obtained analytically (solid line) and the curve calculated by means of the Bloch theorem perfectly match, illustrating the relevance of the method. The result's consistency is preserved in the whole Brillouin zone for different angular position (the whole first Brillouin zone has been inspected). These results are also useful because they show the impossibility to focus the energy along specific direction, this is still true modifying the excitation frequency ω (images in Figure 2.9).

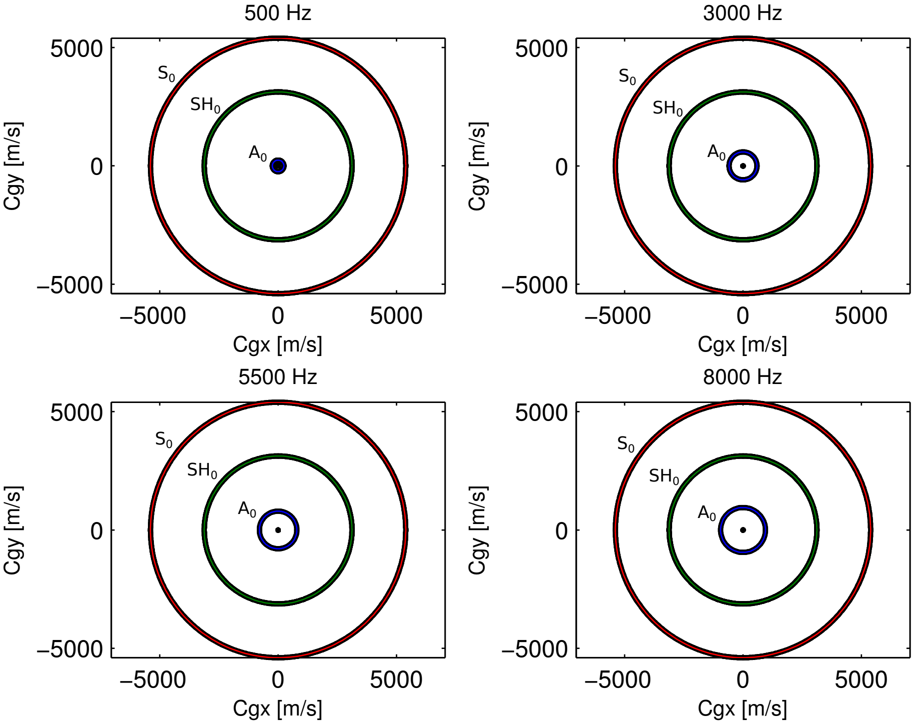

Figure 2.9: Analytical (solid line) and numerical (markers) A_0 and S_0 mode group velocity circles of a 3 mm aluminum plate at different frequencies: 500 Hz, 3000 Hz, 5500 Hz and 8000 Hz

2.5 Wave Dispersion in a Periodic Stubbed Isotropic Plate

The dynamic behavior of the hosting system can be modified by adding some inclusions (elastic stubs) periodically arranged over the top surface of the plate. The plate has an infinite extension in the x and y direction and a thickness of 3 mm, the elastic stubs are brick of 50 mm wide with a thickness of 10 mm. Both structures are made of an isotropic Aluminum with the following properties: $\nu = 0.33$, $E = 70$ $[GPa]$, $\rho = 2700$ $[kg/m^3]$. By using symmetry of the unit cell, the corresponding first Brillouin zone is described in Figure 2.6 where the irreducible zone is the shaded area.

Figure 2.10 represents the dispersion relation of the slightly damped system along the Ox direction ($\theta = 0$, see Figure 2.6). For sake of completeness no preliminary sorting procedures have been performed: propagative and evanescent waves coexist in the same diagram and solutions outside the first Brillouin zone were retained. This choice was deliberately made with the aim of pointing out the main features of the solutions. The symmetry of the diagram with respect the

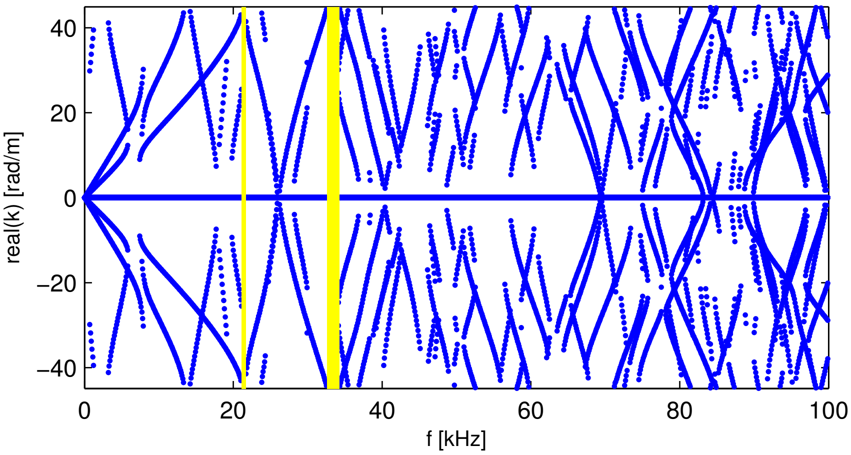

Figure 2.10: Dispersion relation of stubbed plate. Frequency f vs propagative part of the wavenumber k. The yellow stripes represent the band-gaps generated by the interaction between the waveguide and the stubs.

Ox axes can be considered as an indicator of the consistency of the obtained results, outsides the irreducible zone the wave solutions are just repeated and basically re-labeled.

From the physical standpoint this diagram establish the relation between the wavelength and the frequency associated at each wave mode. The regions highlighted by yellow rectangles represent frequency band where waves can not propagate, there is no wavenumber that satisfies the eigenvalue problem (2.42). By creating an impedance mismatch within the waveguide it is possible to create band gaps where waves can not propagate. The wideness and the position of the band gap in Figure 2.10 can be modified by varying some geometric or material parameters. With the aforementioned parameters the location of the first two stop bands of the system are observed from 21 to 22 kHz and from 32 to 34 kHz. The precision of these results depend on the frequency step and the discretization of the associated finite element model.

2.6 Wave Dispersion in a Periodic Piezocomposite Lattice

In the previous section we shown how is possible to modify the dynamic of the considered two-dimensional waveguide introducing elastic stubs periodically arranged over the whole plate. This layout is able to modify the dispersion relation of the waveguide, if the size of the intrusion is comparable to the wavelength of the incident wave a band gap associated to that wave mode

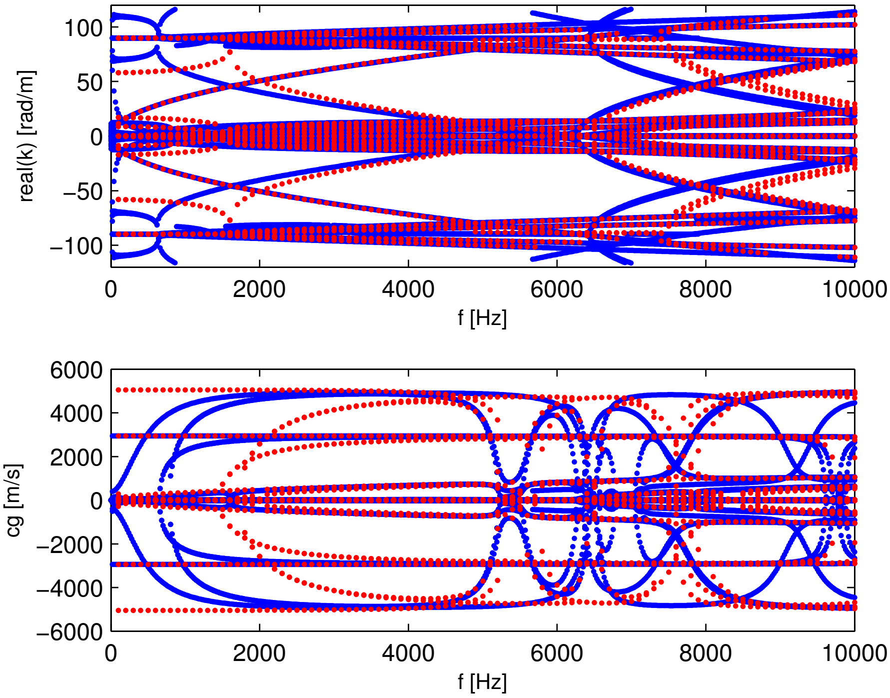

Figure 2.11: Dispersion curves (top) and group velocity (bottom) of the metacomposite. Two meshes have been analyzed: coarse mesh (red dots), refined mesh (blue dots).

is observed. The limitations related to this approach is the lack of control capabilities at low frequencies and their effectiveness limited to a narrow frequency band.

For this reason a different approach has been considered. Replacing the elastic intrusion with piezoelectric ceramic shunted to an external electric circuit is possible to achieve better performances overcoming the aforementioned limitations.

The piezoelectric ceramic have a length and width of 50 mm and a thickness of 0.5 mm the associated material properties are summarized in appendix A. The piezoelectric ceramic are bonded on the top surface of the plate.

In Figure 2.11 the dispersion relation of the metacomposite is compared for two different mesh size: the red dots correspond to a coarse mesh, the blue dots correspond to a refined model. The analyzed model provides two solution that sensibly differ over the considered frequency band, this is justified by convergence problem that can occur when poorly meshed models are considered. This is a well-known fact, however, the thickness of piezoelectric ceramic imposes

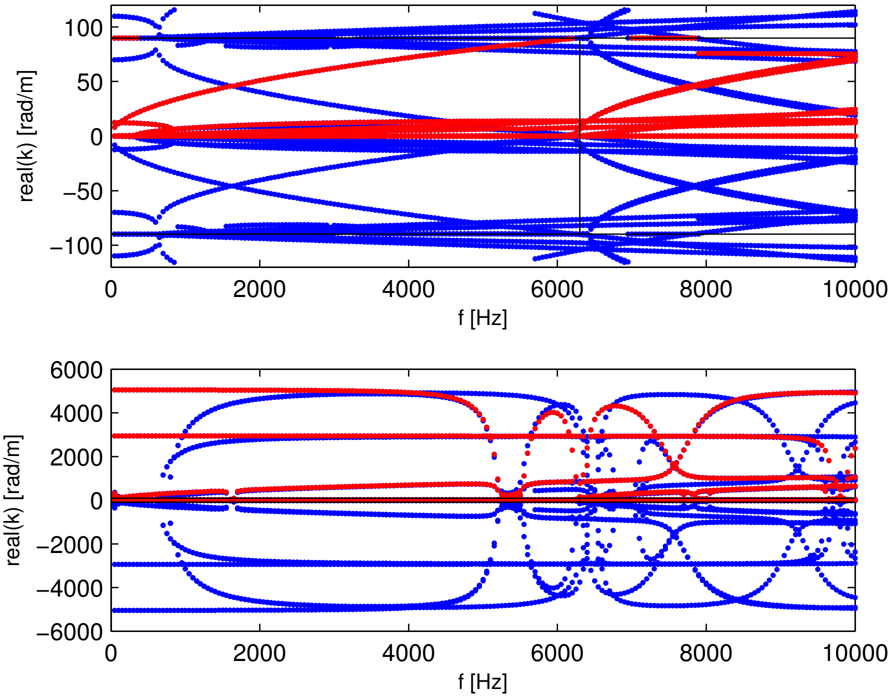

Figure 2.12: Wave filtering according to criteria 1,2 and 3.

a restraint on the overall size of the mesh. In particular, a request for a better mesh density determines an increase of the number of model's degrees of freedom and therefore a greater computational effort. The limitation associated to the mesh density determines also the frequency shift observed for the higher order periodic branches. As an example let us consider the A_0 mode the dispersion relation shows that the first branch located in the vicinity of the x axes starts at 0 Hz as expected, while the origin of the twin branch located at the edge of the Brillouin zone is shifted toward higher frequencies. The same effect is observed for the rest of the modes. This effect is more evident for the red curves, the blue curves associated to the refined model tends to mitigate this phenomenon. For sufficiently dense meshes the higher order branches will shift up to align to the main set of solutions. The results presented in Figure 2.11 are not immediately exploitable, the propagative and the evanescent wave-modes are mixed together, there is no way to distinguish the flexural from the axial modes and finally the solution lying in the first Brillouin zone are mixed with the solution located in the adjacent bands.

It is absolutely necessary to filter all the generated waves in order to retain just a subset of them.

Different filtering criteria can be considered:

1. the nature of the wave;
2. the ability to propagate;
3. the necessity to keep the solutions in the first Brillouin zone exclusively.

The piezo-actuator can offer a control capability only if it is excited by flexural waves, for that reason a preliminary sorting must be performed in order to keep only the designated wave-modes having, for example, the following property:

$$Ind_z > 0.9 \tag{2.45}$$

where Ind_z represent the portion of the kinetic energy associated to the degrees of freedom in the out-of-plane direction, it is calculated as

$$Ind_z = \frac{T_z}{T_{tot}} \tag{2.46}$$

where T_z is the averaged kinetic energy along the z direction and T_{tot} the total averaged kinetic energy. The averaged kinetic energy is calculated as

$$\langle T \rangle = \int_\Omega \rho v v^* dV \tag{2.47}$$

where v represents the velocity field and v^* its conjugate.

The ability of propagating is determined considering the group velocity of each wave-mode, by imposing a threshold value. By imposing the following constraint

$$c_n^g > c_g^{thr} \tag{2.48}$$

it is possible to discriminate the propagative and the evanescent waves. As mentioned before the solutions obtained solving the associated eigenvalue problem are periodic in the sense that the wavenumbers outside the first Brillouin zone are the same obtained within the Brillouin zone and just re-labeled. For that reason it is mandatory to select among all these modes the correct set of eigen-solution. This is achieved by imposing the following constraint

$$real\left(k\right) > \frac{2\pi}{d_x \cos\theta + d_y \sin\theta} \tag{2.49}$$

where d_x and d_y is the length of the primitive cell in the x and y direction respectively. However, even if all these conditions are met it is not always possible to distinguish the different incoming waves, as depicted in Figure 2.12. The red curve represents the set of eigensolutions respecting the filtering conditions, beyond the cut frequency (6300 Hz) it is no longer possible to follow the A_0 mode. Besides beyond this frequency two branches of the dispersion curve are selected.

2.6.1 Impedance Optimization

One aim of this work is to provide a numerical methodology for optimizing the piezoelectric shunt impedance $Z(\omega)$ for controlling energy flow into the periodically distributed piezocomposite structure. To do so, we need to define suitable criteria against which to perform the optimization. The first criterion which is considered for describing the capability of the metacomposite for transmitting structural energy is based on the computation of the wave group velocities. Indeed, they indicate how energy is transported into the considered system and allow to distinguish the propagative and evanescent waves. If a Bloch eigensolution (i.e. $u_n\left(\omega, \Phi\right)$, $k_n\left(\omega\right)$) is considered, the associated group velocity vector (Maysenholder [62]) is given by

$$c_n^g = \nabla_k \omega = \frac{\langle\langle S\rangle\rangle}{\langle\langle e_{tot}\rangle\rangle} = \frac{\langle I\rangle}{\langle E_{tot}\rangle} \tag{2.50}$$

where $\langle\rangle$ is the spatial and time average, on one cell for period of time, S is the density of energy flow, I is the mean intensity and e_{tot} and E_{tot} are the total electromechanical energy and its time average on a period. In this problem, we only consider mechanical energy transportation as the electrostatic coupling is decentralized on each cell and cannot induce spatial energy transportation. The electromechanical coupling effect is also condensed into the mechanical behavior as explicitly introduced in Hagood and Von Flotow [45] and extended to FE model in Collet and Cunefare [25].

The intensity vector I is expressed as

$$\langle I \rangle = -\frac{\omega}{2}\text{real}\left(\int C_E\left(\varepsilon + ik\Xi\right)w^* d\Omega\right). \tag{2.51}$$

As the spatio-temporal average of the system Lagrangian is null, the total energy average is approximated by only computing the kinetic energy average

$$\langle E_{tot} \rangle = 2\langle T_{tot} \rangle. \tag{2.52}$$

The group velocity vectors c_n^g are computed for all wave numbers at each frequency. In order to focus our analysis on only flexural modes (S and SH ones), we use the Ind_z indicator allowing to track them by computing the ratio of the averaged kinetic energy on out-of-plane direction and the total averaged kinetic energy.

Optimization of the shunt impedance $Z(\omega)$ is based on the minimization of the maximal group velocity collinear to the wave number vector for waves having a ratio of transported flexural kinetic energy greater than 0.9. The criterion can then be written as

$$Crit_1\left(\omega, \Phi\right) = \max\left(c_g\left(\omega, \Phi\right) \cdot \Phi\right). \tag{2.53}$$

The second criterion for optimizing the structural energy absorption is based on the maximization of the damped electric power, expressed as the active electrical power

$$P_{el}\left(\omega, \Phi\right) = \frac{1}{2}real\left(V_0 j\omega q_0^*\right). \tag{2.54}$$

In order to increase the damping effects inside the smart metacomposite, this term needs to be sufficiently large. In the second case, the criteria are then

$$Crit_2\left(Z\left(\omega\right), \Phi\right) = \max\left(\frac{1}{P_{el}\left(\omega, \Phi\right)}\right). \tag{2.55}$$

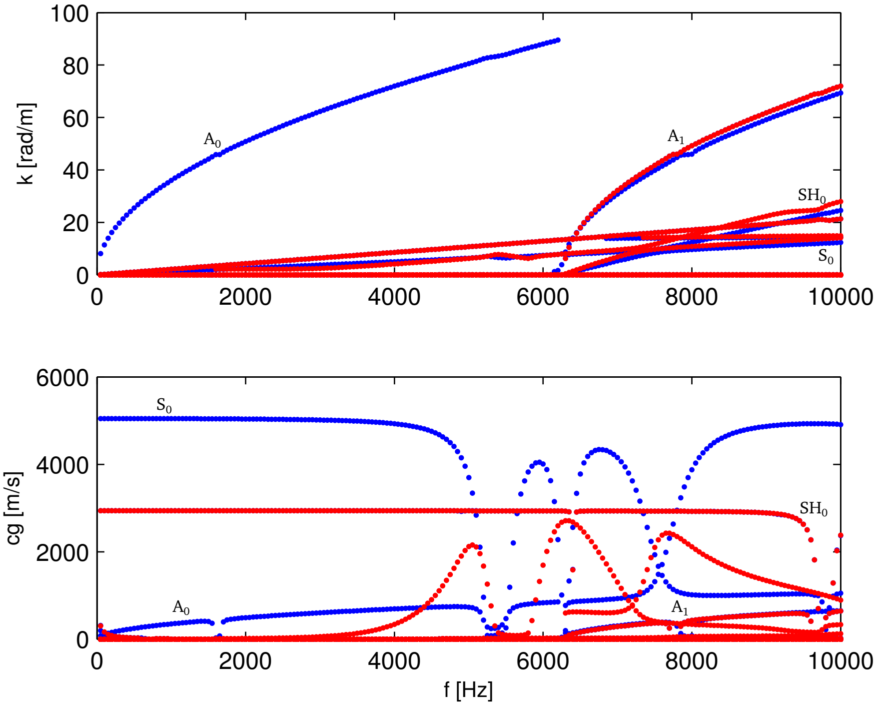

Figure 2.13: Dispersion curves (top) and group velocity (bottom) of the metacomposite for the reflecting configuration: uncontrolled system (blue dots), controlled system (red dots).

2.6.2 Group Velocity Minimization (Reflecting Configuration)

In this part, optimization of the transmission capability of the designed smart interface is considered by using $Crit_1$ given in equation (2.53).

The objective is to avoid the energy transportation of flexural waves (A_0, A_1, SH) once excited into the periodically distributed shunted piezocomposite cells.

The numerical optimization procedure is based on a multidimensional unconstrained minimization algorithm (Nelder-Mead). The optimization is performed by considering an electric circuit represented by its impedance

$$Z(\omega) = Z_r + jZ_i. \tag{2.56}$$

The analysis is initialized with an arbitrary value for both Z_r and Z_i components. Optimization steps are then proceeded using criterion (2.53) and lead us to obtain frequency-dependent complex impedance for describing the circuit behavior.

Figure 2.13 shows the dispersion curves using the propagative parts (here the real one) of the

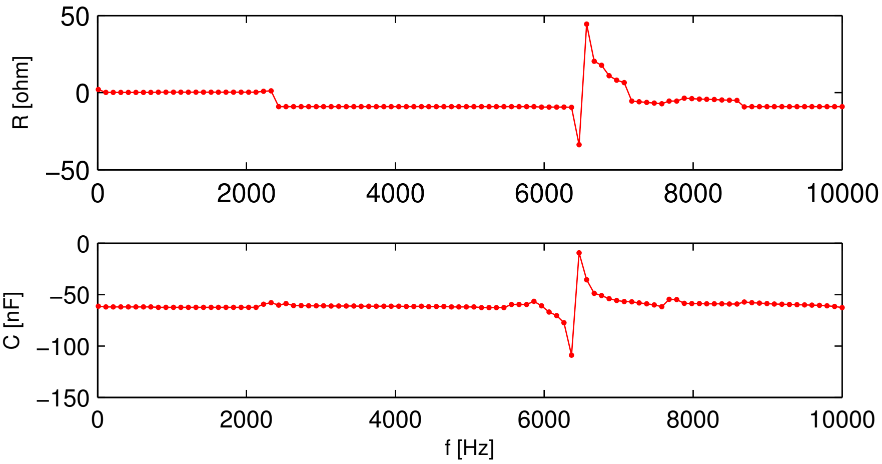

Figure 2.14: Optimal electric impedance expressed in term of the equivalent resistance and capacitance. The optimization (group velocity minimization) is carried out considering waves propagating in x direction.

wave numbers $k_x(\omega)$ along Ox axis, for both initial and optimal impedance shunts. These results have been filtered in order to only retain the propagative parts of the wave number $k_x(\omega)$ along x direction. It then becomes easy to observe branches similar to standard S_0, A_0, A_1 and SH waves. The corresponding group velocities along Ox are presented in Figure 2.13. It can be immediately observed that the optimization of the shunt impedance leads to a larger decrease of the group velocity of the A_0 mode, while the A_1 wave, which becomes propagative at 6700 Hz, is not controlled by the optimal configuration (see Figure 2.13). The bending waves also propagate energy with a very slow velocity and can be considered as evanescent. Flexural energy is, also, only transported by the A_1 mode after the cutting frequency. The propagative part of the controlled wave is strongly modified, as illustrated in Figure 2.13: from two complex conjugated solutions, the A_0 wave changes after control to four solutions (two complex conjugates and their opposites). This situation is described in Gavric [43], which corresponds to high-order evanescent wave solutions.

It can also be observed from Figure 2.13 that a non-dispersive symmetric wave is also affected by the control even if it was not targeted by the optimization procedure.

The value of the optimal impedance are plotted in Figure 2.14. The components of the optimal impedance can be transformed in an equivalent frequency varying resistance and capacitance. The equivalent capacitance and assumes a negative value almost everywhere in the considered

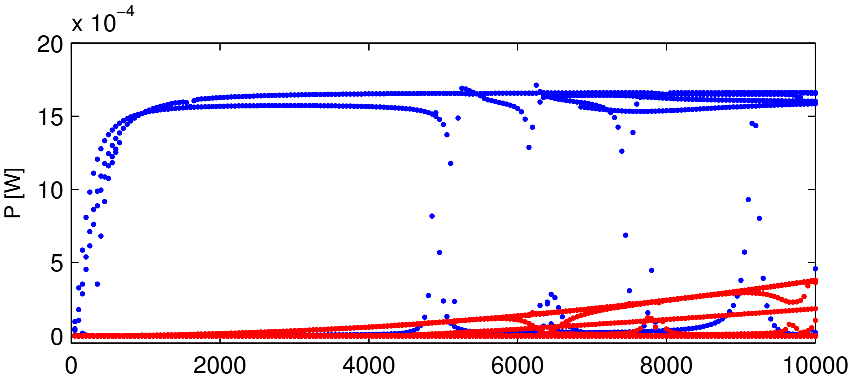

Figure 2.15: Dissipated power flow of the metacomposite for the reflecting configuration: uncontrolled system (blue dots), controlled system (red dots).

frequency band. The averaged capacitance value is $-51.21\ nF$ which is in good agreement with the theory and experimental evidences, the measured intrinsic capacitance for the piezo-ceramic is 50 nF. The active part part of the impedance (the resistance) get a negative value in a large frequency band which means that the control system tries to compensate the dissipative phenomena within the controlled system, converging toward an almost conservative system. The external circuit delivers a certain amount of electric energy to the waveguide in order to reduce the mechanical damping effects introduced by hysteretic terms in the model. The curve describing the two components of the optimal impedance show some discontinuities around 2000 and 6000 Hz. The first discontinuity is justified by the the problem of convergence observed and described in Figure 2.11, the intersection of two identical branches (A_0 mode) shifted of same extent determines a perturbation in the optimal impedance. The discontinuity observed at 6000 Hz is due to a different problem that can be motivate in the following manner: beyond the 6300Hz the the wave filtering procedure switch from the A_0 to S_0 and A_1 modes causing loss in the smoothness of the solution as depicted in Figure 2.12. The controlling capabilities of the system are also confirmed in Figure 2.15 where the electrical dissipated energy appears negative when the optimal shunt is connected to the patch. The final controlled system tends to achieve an almost fully reactive configuration.

This last point is of paramount importance in both physical and technological points of view. Indeed, this result tends to show that a pure band gap effect is only reachable if the system is completely reactive, which means that no dissipation occurs in the system. The technological

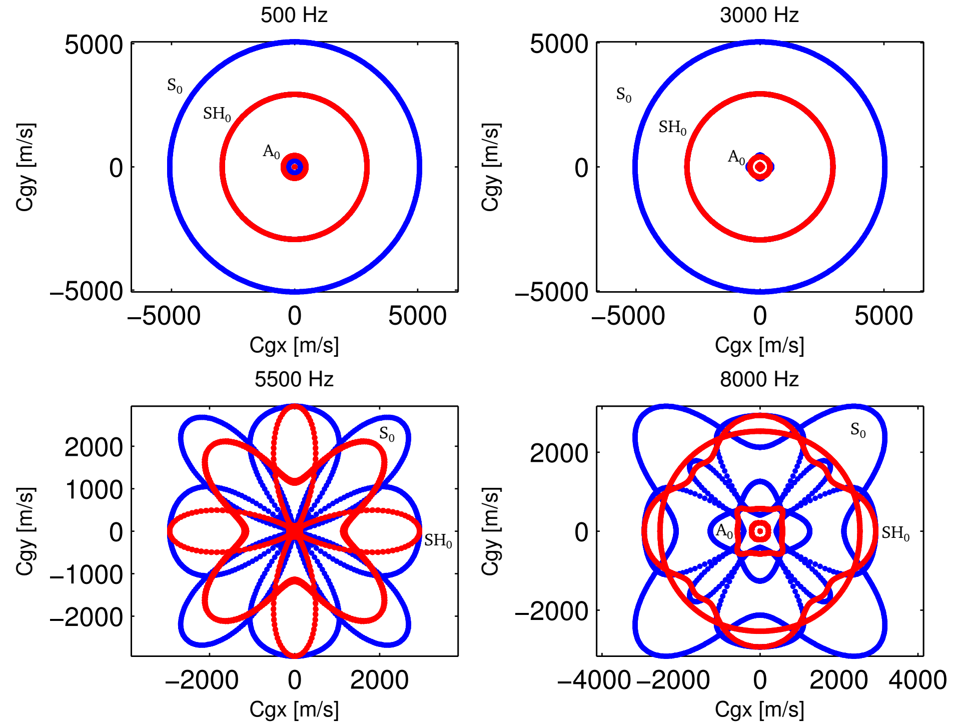

Figure 2.16: Group velocity directivity of the metacomposite for the reflecting configuration: uncontrolled system (blue dots), controlled system (red dots).

implementation of such interface allowing cancellation of structural transmissibility is then unrealistic since it leads to the implementation of only asymptotically stable system: the stability margins will be drastically reduced when negative resistance is implemented for controlling energy transmission.

This smart waveguide shows another interesting property: for specific frequency values the group velocity varies as the direction of propagation is modified. For example at 5000 Hz the energy flows isotropically in all direction whereas at 5500 Hz or 8000 Hz a concentration of energy is observed along the 45 degrees direction, Figure 2.16.

2.6.3 Damped Power Flow Maximization (Absorbing Configuration)

Another strategy for optimizing the adaptive metacomposite consists in focusing on the damped power flow inside the electric shunts by using the criteria $Crit_2$ given in equation (2.55). In this case, the objective is to improve the absorption capability of the smart structure. This effect is

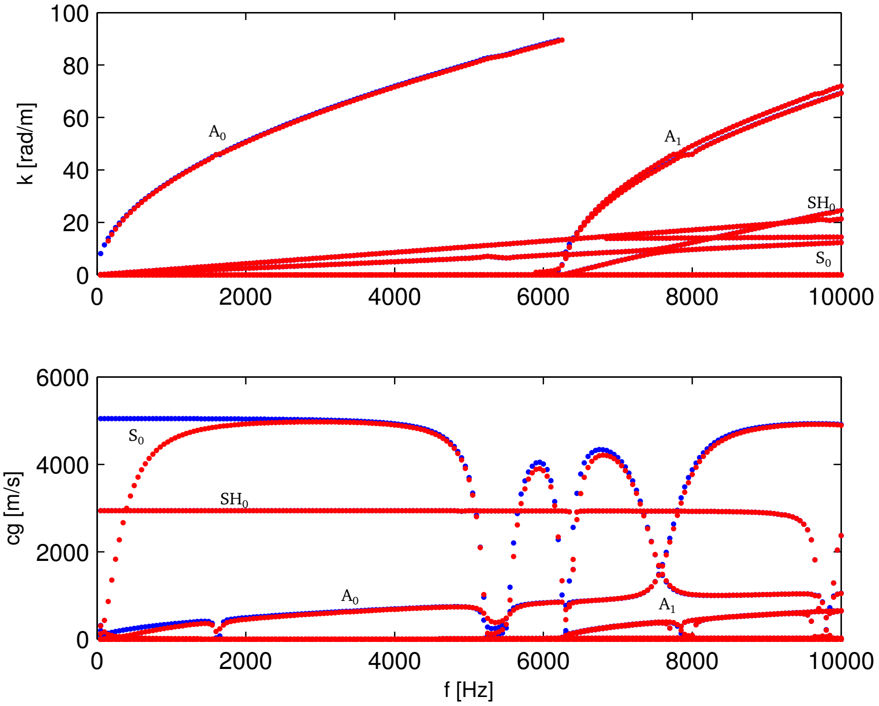

Figure 2.17: Dispersion curves (top) and group velocity (bottom) of the metacomposite for the absorbing configuration: uncontrolled system (blue dots), controlled system (red dots).

achieved acting on the external electric circuit, properly choosing the resistance and capacitance value it is hence possible to increase the overall damping of the structure. The vibrational energy of the waveguide is transformed in electric power dissipated by Joule effect within the external resistance.

The propagative parts of the wave number $k_x(\omega)$ along Ox axis appear as shown in Figure 2.17. The first observation is that the optimization of the shunt impedance for improving the absorption characteristics of the system induces no modifications in the propagative part of the wave numbers. This can be explained by a large improvement of the ratio between the real and imaginary parts of the wave numbers, which physically corresponds to the forcing of propagating effects to increase damping effects: energy can propagate inside the periodically distributed set of active cells for allowing electrical energy conversion. This figure also underlines the ability of the procedure to catch all Bloch's solutions including evanescent ones that generally do not appear in literature because of their imaginary character. In the context of structural dynamics,

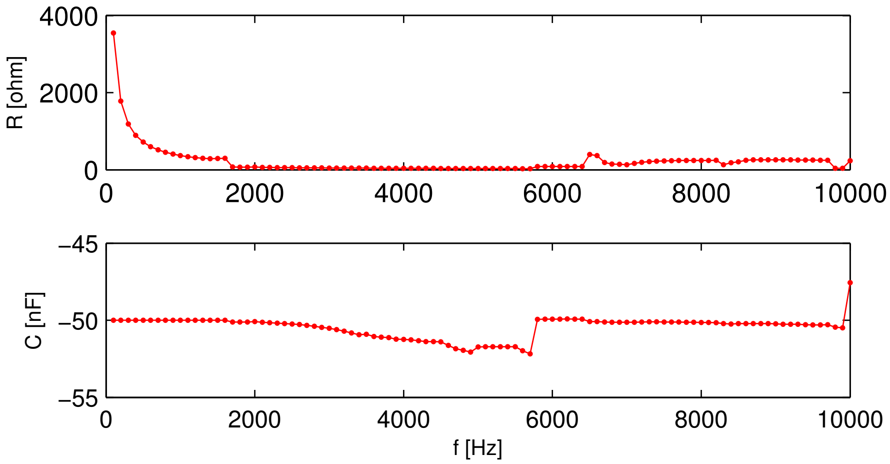

Figure 2.18: Optimal electric impedance expressed in term of the equivalent resistance and capacitance. The optimization (damped power flow maximization) is carried out considering waves propagating in x direction.

including damping effects is mandatory for real-life applications and all wave numbers become complex, which constitutes a key point in our analysis as underlined in Collet et al.[26] and Gavric [43]. By using a suitable wave filter based on the group velocity, it is possible to retain for presentation only propagative solutions responsible for energy transport. For a sake of clarity, the following results will be presented by showing only propagative waves.

The optimal impedances of the electric shunts are plotted in Figure 2.18. The optimal impedance values correspond to an almost constant negative capacitance (bottom of Figure 2.18) of $-52\ nF$. The equivalent resistance (bottom of Figure 2.18) corresponding to the active part of the shunt impedance are positive, which is in accordance with the fact that a damping effect is expected. Again, the problems related to model discretization reduce the smoothness of the solution.

Figure 2.19 finally shows the effect of the external circuit on the damping capabilities of the smart metacomposite. By comparing the absorbed electric power for the uncontrolled system (blue dots) and the controlled one (red dots) it is clear that the external circuits to add an extra amount of damping increasing the energy consumed by Joule effect.

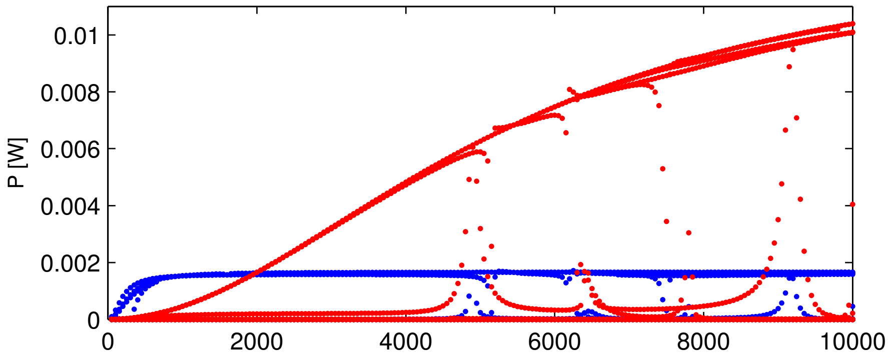

Figure 2.19: Dissipated power flow of the metacomposite for the absorbing configuration: uncontrolled system (blue dots), controlled system (red dots).

2.6.4 Harmonic Response of a Finite-extent Plate

The optimizations of the smart metacomposite that have been proposed were carried out by considering infinite periodic structures. The objective of this section is to illustrate the applicability of the designs for integration into real-life finite structures.

The optimal impedance is then applied on a finite set of shunted piezocomposite cells distributed on a part of a free plate system submitted to a point force in one corner. Material damping is introduced throughout a constant imaginary part of the elasticity tensor. The harmonic response of this system is then compared in the $0 - 5000\ Hz$ frequency band for different circuit configurations, namely the open circuit, the optimal impedances obtained by using criterion $Crit_1$ and the optimal impedances obtained by using criterion $Crit_2$.

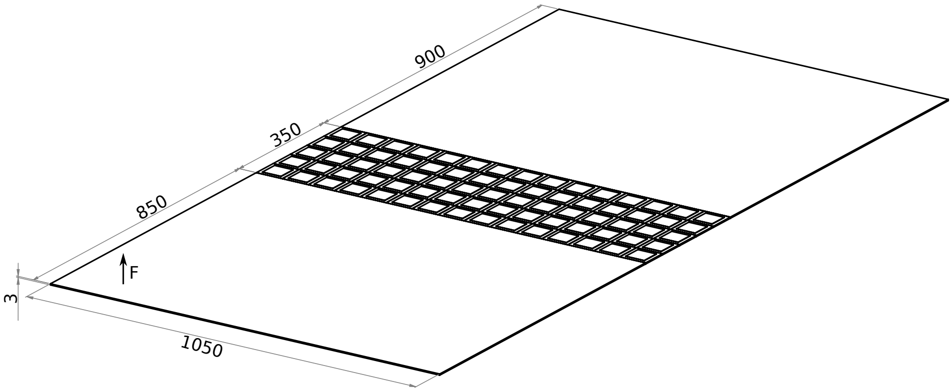

Figure 2.20: Plate with periodic semidistributed set of cells (measures in mm).

A suitable indicator that qualifies the attenuation capabilities of the smart metacomposite is the loss factor. Estimation of the loss factor requires the calculation of the time-averaged power input to the system, and the total time-averaged energy of the system (potential plus kinetic energy).

$$P_0 = real\left(\frac{1}{2}F \cdot v^*\right). \tag{2.57}$$

By integrating the plate's velocity field it is possible to calculate the plate's time-averaged kinetic energy

$$T_0 = \int_\Omega \rho v v^* dV, \tag{2.58}$$

and the time-averaged total energy E_0,

$$E_0 = T_0 + U_0 \simeq 2T_0. \tag{2.59}$$

The loss factor of the plate is then calculated by

$$\eta = \frac{P_0}{\omega E_0}, \tag{2.60}$$

where P_0 also represents the time-averaged power dissipated in the system.

Figure 2.21 presents the loss factor for the considered system with open circuit, $Crit_1$ and $Crit_2$ optimal shunts connected to each piezoelectric patch. The first configuration, associated to $Crit_1$, prevents the energy transfer of the flexural waves. The mechanical response of the system is strongly modified. The second configuration, based on $Crit_2$ optimal shunt, forces energy dissipation into the resistive part of the electric shunt, this observation is supported by an increase in the loss factor.

Another system's performance indicator is the kinetic energy ratio that indicates how the vibrational energy is distributed into the considered system also shown in Figure 2.21. For sake of convenience the kinetic energy associated to the lower part of the plate is considered. The minimization of the flexural wave group velocity ($Crit_1$) leads to an increase of the kinetic energy reflected by the smart interface, while the maximization of the damped energy ($Crit_2$) only slightly modify this distribution. The modification of the energy distribution into the system is very important after 200 Hz and increase with the frequency when the energy is globally

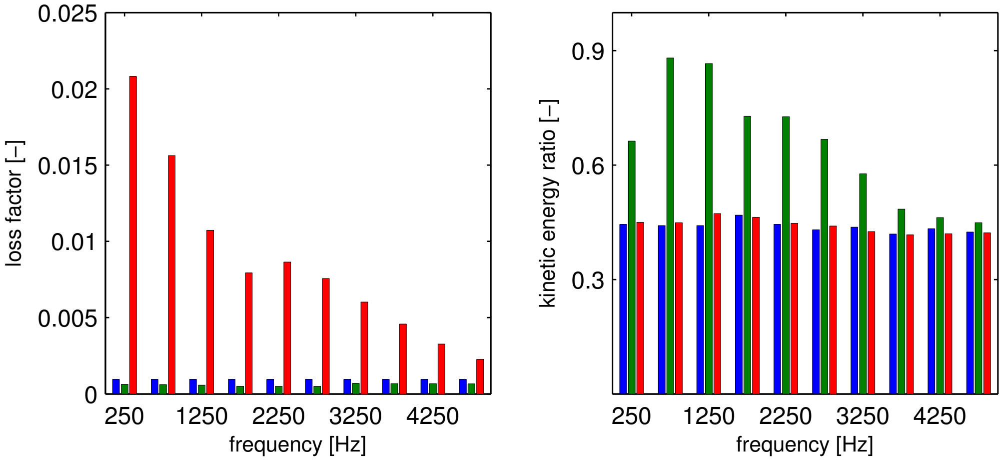

Figure 2.21: Loss factor (left) and kinetic energy ratio (right) for three different circuit configuration: uncontrolled (blue bar), controlled reflective configuration (green bar) and controlled absorbing configuration (red bar).

transported by A_0 mode. This is not the case in the lower frequency band when the interface works in the near-field domain of the applied point force.

Figure 2.22 shows the corresponding results in terms of velocity field. These numerical results clearly show a strong influence of the modifications of the wave dispersion characteristics on the standing wave responses, especially when $Crit_1$ is used. In particular, at 45 Hz, a large attenuation of the dynamic response of the system can be observed when optimal shunts are connected. In this case, when the shunts are optimized for flexural energy flow cancellation ($Crit_1$), the location of the nodal lines is also modified, this fact indicates a modal restructuring, the resonance peaks are moved far from the open circuit configuration, this trend may indicate a modification of the internal dynamics of the waveguide. At the same frequency the system's response associated to $Crit_2$ is almost not affected by the action of the piezoelectric actuators, just a small vibration reduction is observed. This optimization procedure has the aim to mitigate the structural vibrations by adding a certain amount of damping in the form of electrical energy dissipated by the electric circuit. At 1390 Hz, when $Crit_1$ optimal shunts are connected, a large part of the system energy remains in its lower part where the applied force is located. The smart metacomposite interface is able to filter wave diffusion by increasing its reflection properties. The $Crit_2$ optimal shunts determine a evenly reduction of the system response. The most important difference between the two control strategies is possibility or not to create a wave confinement.

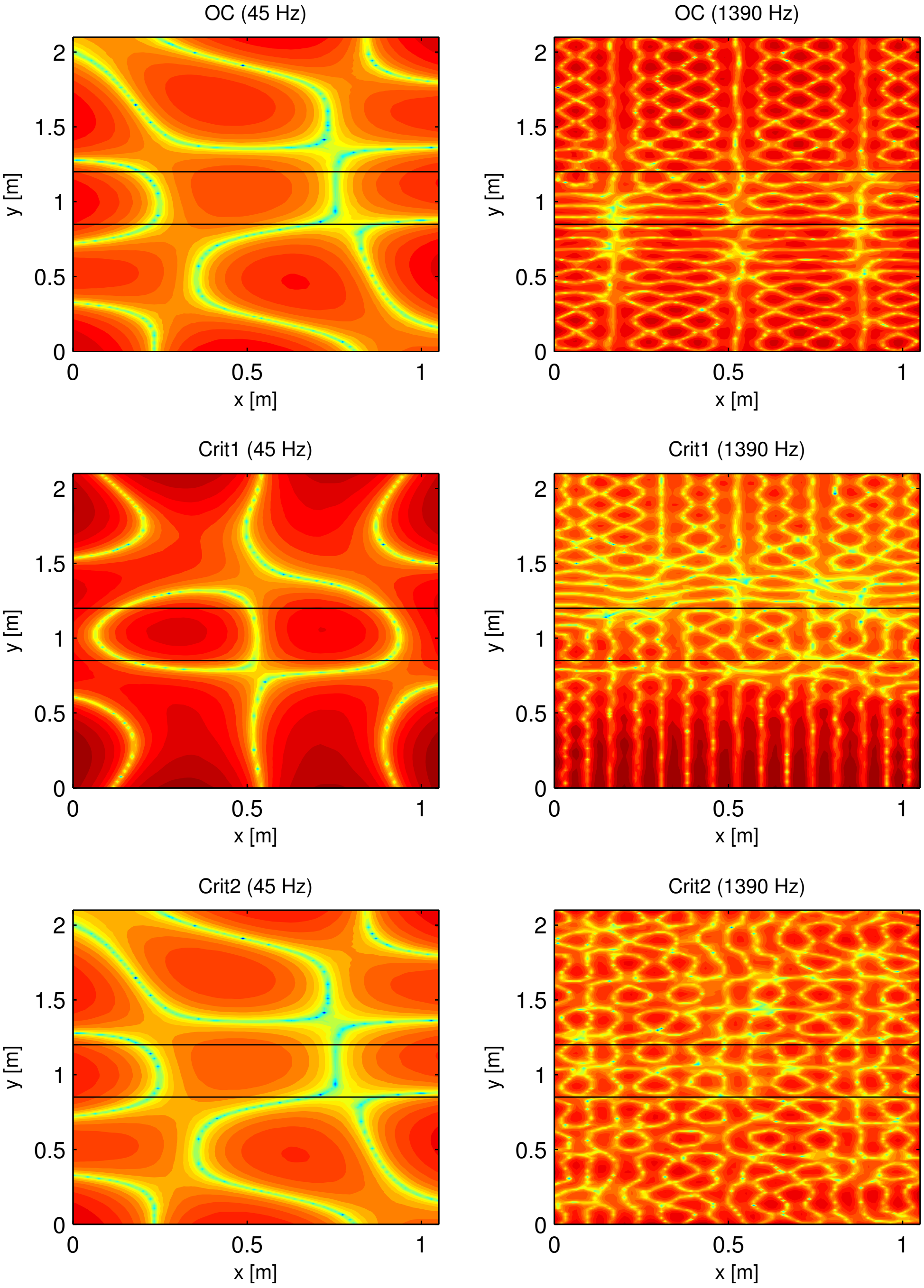

OC (45 Hz)

OC (1390 Hz)

Crit1 (45 Hz)

Crit1 (1390 Hz)

Crit2 (45 Hz)

Crit2 (1390 Hz)

Figure 2.22: Velocity field of the system excited by a point force at 45 Hz (left) and 1390 Hz (right) for three different circuit configuration: uncontrolled (top), controlled reflective configuration (center) and controlled absorbing configuration (bottom).

2.7 Conclusions

This section presents a numerical procedure able to compute the dispersion relation of a multi-dimensional waveguide in the whole first Brillouin zone.

The method has been verified by evaluating the dispersion relation of the bare plate. Subsequently a periodic array of material inclusion (stubbed plate) has been considered in order to show the filtering capabilities of the passive waveguide at high frequencies. Based on this approach, a suitable criterion indicating the evanescence ratio of computed waves has been proposed. The damping operator introduced in the formulation can be frequency dependent as viscous one but can also be much more complicated. It can compass specific dissipation phenomena such as those induced by distributed shunted piezoelectric patches as proposed by Beck [11], Casadei et al. [20].

The method was applied for determining the optimal shunt impedance allowing the minimization of the group velocities of the flexural waves or the maximization of the damping capability of the distributed system.

The smart array of piezoelectric patches can be included in a finite structure to confer on it new functionalities. Some numerical tests on a finite dimension system incorporating a distributed set of shunted piezoelectric cells have been performed. A strong influence of the shunt circuits has been underlined in the dynamical response of the system, the modification of the energy distribution into each structural sub-domains has eventually shown the filtering capabilities of the smart waveguide. However, additional work has to be done for: optimizing the complete interface scattering and controlling the evanescent waves playing an important role in this frequency range (LF band).

Furthermore, robustness of the proposed methodology has to be proven under different operative conditions.

Chapter 3

Prototyping and Testing the Adaptive Metacomposite

3.1 Overview

Chapter 2 presented the design of adaptive metacomposite for the control of propagating waves in two-dimensional waveguide.

This chapter illustrates the practical implementation of a such a device, providing some recommendation for the correct design of the sub components such as the periodic array of piezoelectric ceramics and the external electric circuit.

Controlling performance of the produced prototype is evaluated experimentally on a small plate possessing just one patch in the presence of a random broadband excitation. More precisely, the frequency response function of controlled plate is measured under different operating configuration. The obtained results are used in order to select the more appropriate set of parameters used in the subsequent chapter with the distributed control system.

3.2 Electromechanical Interface Design

This section introduces the design of the smart metacomposite, including the plate structure, design criteria leading to selection of the piezoelectric patches used in the active interface, and the design and impedance characteristics of the shunting circuit. The basic structure of the

Plate	Length	2100	mm
	Height	1050	mm
	Thickness	3	mm
	Mass density	2700	kg/m^3
	Young's modulus	$70 \cdot 10^9$	N/m^2
	Poisson's ratio	0.33	–
Piezo	Length	50	mm
	Height	50	mm
	Thickness	0.5	mm
	Mass density	7650	kg/m^3
	Poisson's ratio	0.31	–
	Dielectic loss	< 0.05	%
	Coupling factor	0.31	–

Table 3.1: Geometry and physical properties of the system.

metacomposite comprises an aluminum plate and array of piezoelectric patches as depicted in Figure 3.1. The geometry and material properties for the plate and piezoelectric materials are listed in Table 3.1. The plate is suspended from a rigid frame by metallic wires in order to approximate free-free boundary conditions. The plate is equipped with 75 piezoelectric patches (Ferroperm Industries $PZ26$ series) arranged in a regular 15 × 5 array as seen in Figure 3.1 and Figure 3.2. The dimension of the piezoelectric patches are listed in Table 3.1. The patches and the depth of the patch array were selected based on consideration of their size relative to the shortest structural wavelength of interest. The array was intended to be effective up to a frequency of 5000 Hz. The plate's dispersion relation for the A_0 flexural mode at 5000 Hz has a wavelength of 30 cm. With patches having dimensions of 50 × 50 mm, there will be no charge cancellation on an individual patch as would occur if the patch dimensions were comparable to a wavelength. Further, the depth of the patch array is 350 mm such that it spans more than a wavelength at 5000 Hz. Since the array elements are uncoupled electronically, each element within the array would still function at the highest frequency of interest, even though the entire array depth would be comparable to a wavelength. The thickness of the patch was selected considering the constraints of the electric circuit and the nature of the control technique. Different authors have shown that the best controlling effect is obtained when the negative impedance shut circuit is tuned close to the inherent patch capacitance [40, 59]. This property strongly depends on the material properties and the geometry of the patch. Once the material properties and the two

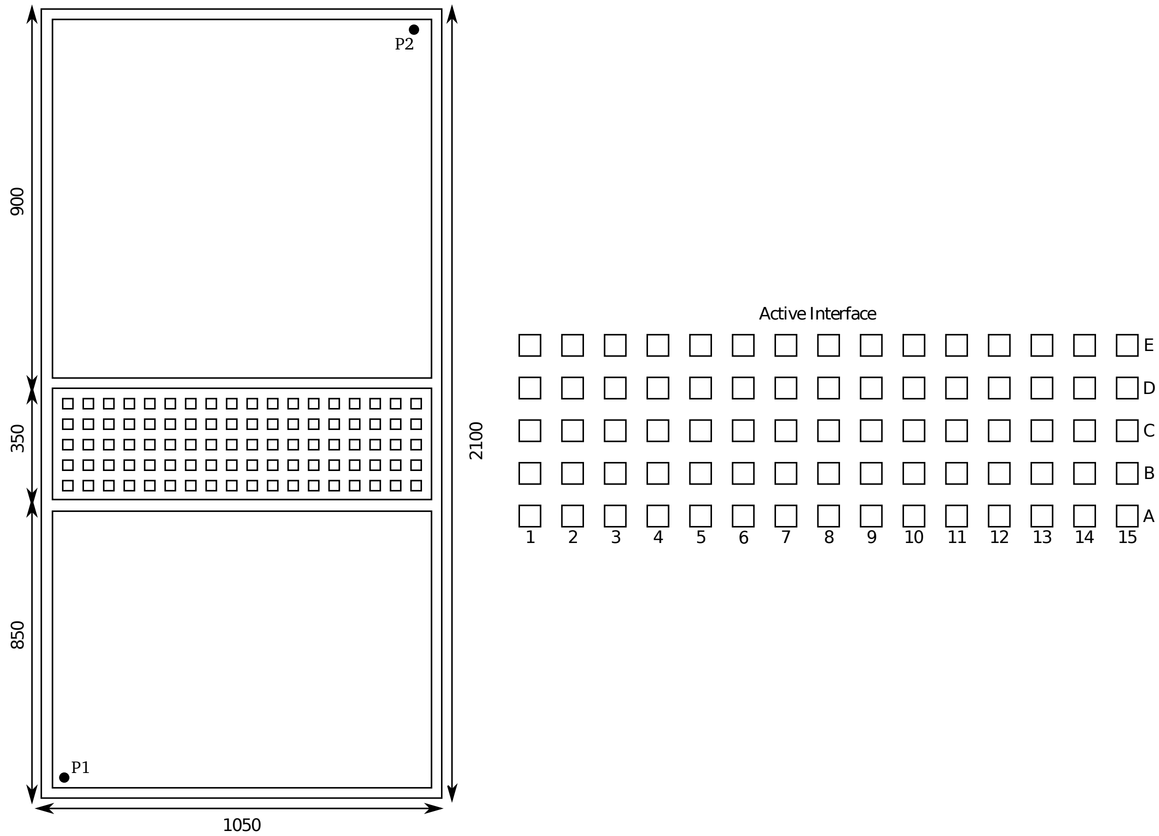

Figure 3.1: Schematic of the plate with its dimensions. Input force applied at point P_1. Single-point response measurement at P_2.

dimensions of the piezoelectric patch are chosen, the only parameter which remains for selection is the thickness. Thin patches exhibit larger values of intrinsic capacitance which would yield increased control, however, this parameter cannot be reduced indefinitely due to the weakening of the piezoelectric patch itself. For these reasons, a thickness of 0.5 mm was selected.

For a correct analysis of this electromechanical system is often useful to introduce an equivalent electric model. The electromechanical interface formed by the plate and the piezoelectric ceramic is therefore modeled as a strain dependent voltage generator connected to a capacitive circuit. Classically, this model represent the electrical properties of patch as a pure imaginary part of an equivalent impedance, this is true when the real part of the patch impedance is several order of magnitude bigger than the imaginary part. Otherwise, a modified electrical model for the patch must be used to accurately describe the frequency response of the patch. This situation can occur for frequencies near DC, typically below 50 Hz, or when capacitance of the patch is

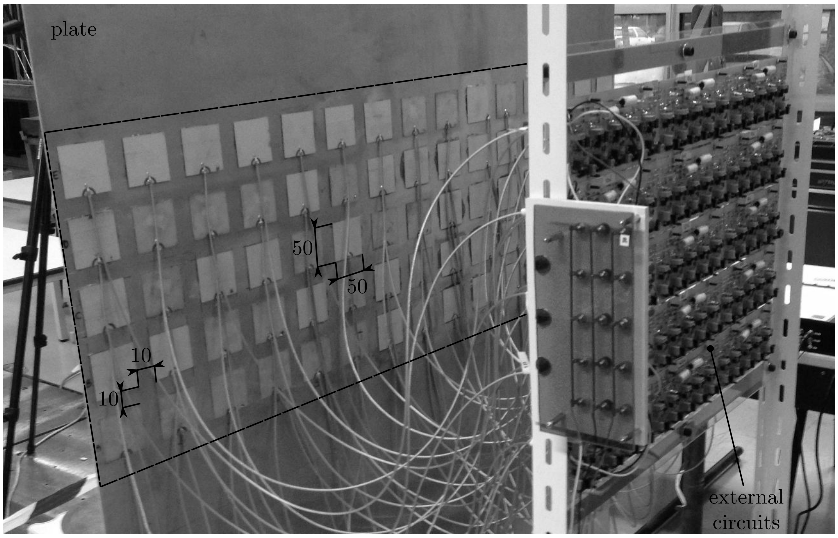

Figure 3.2: Photograph of plate with 75 element piezoelectric patch array comprising an active interface, connected to bank of 75 individual negative impedance shunt control circuits. Patch dimensions and spacing annotated on photograph.

small. In this modified model a resistor located in parallel with the capacitance of the patch is introduced. To determine the patch impedance, a simple experiment can be set-up by introducing a complementary electric circuit having the following transfer function

$$\frac{V_{out}}{V_{in}} = \frac{R}{R + Z_p} \tag{3.1}$$

R is a tunable resistance and Z_p is the impedance of the piezoelectric ceramic. In presence of a pure reactive behavior the circuit's response is equivalent to an high pass filter.

Equation (3.1) can be rearranged to solve for the impedance of the patch

$$Z_p = R\left(\frac{V_{in}}{V_{out}} - 1\right) \tag{3.2}$$

When using this method to determine the impedance of the patch, it is best to measure the patch impedance before bonding it to the vibrating system. For in-situ measurement of the impedance, the effects of the structure must be removed through a frequency-dependent model of the patch impedance that does not include the structural resonances. To approximate the impedance of the patch versus frequency, due to the non-ideal nature of the piezoelectric impedance, the resistor and capacitor are modeled as frequency-dependent components. The frequency-dependent resistor

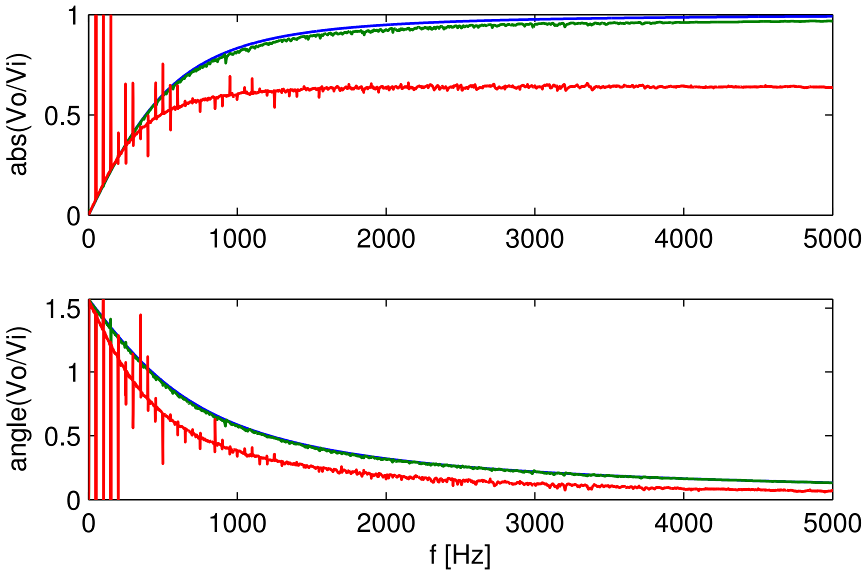

Figure 3.3: Piezoelectric ceramic characterization via high pass filter circuit technique. Theoretical curve (blue) is compared to the experimental measurements: high coupling (green) low coupling (red).

must be added in parallel with the capacitor in the traditional piezoelectric model

$$Z_p = \frac{1}{\frac{1}{R_p} + j\omega C_p} \tag{3.3}$$

where R_p and C_p are the frequency-dependent resistor and capacitor. This resistance can arise from the quality of the bond between the patch and substrate because the leads of the piezoelectric patches must be electrically isolated. When full electrical isolation is not present, some amount of inherent resistance may develop. The exact resistance and capacitance for each patch is measured. This method is used to determine the frequency-dependent patch impedance of all the patches in the array in-situ.

Figure 3.3 compares the experimentally-measured and the theoretical responses of the high pass filter connected to the piezoelectric patch. The blue line represent the theoretical response, the green line represents the experimental data for a piezoelectric ceramic correctly installed and the red line the piezoelectric ceramic exhibiting a poor-quality bonding. Both the magnitude and phase correctly match when the piezoelectric ceramic is properly installed on the surface of the plate, the matching between the two curve also indicates that the piezoelectric ceramic act as an almost pure capacitance, no parasitic dissipative effects are added.

Figure 3.4 shows the experimentally-measured response of the high pass filter connected to each piezoelectric patch, in the left column is depicted the magnitude of the response and in the right column its phase. By analyzing the different system's response (grouped in 5 lines of 15 specimens) we observe a moderate dispersion of the results. This fact is justified by the following remarks: the material properties of piezoelectric ceramic can fluctuate across the considered population, the degree of adhesion between the external surfaces of the plate and the piezoelectric ceramic can also vary inducing a variation in the overall electromechanical coupling.

Another test designed to verify the correct bonding between the piezoelectric ceramic and the top surface of the plate consists in the electric excitation of a given piezoelectric patch and the measurement of the velocity of some point belonging to the plate.

In Figure 3.5 are collected the transfer function of each piezoelectric ceramic, by comparison is possible to conclude that the electromechanical coupling is ensured for almost all the piezoelectric patches.

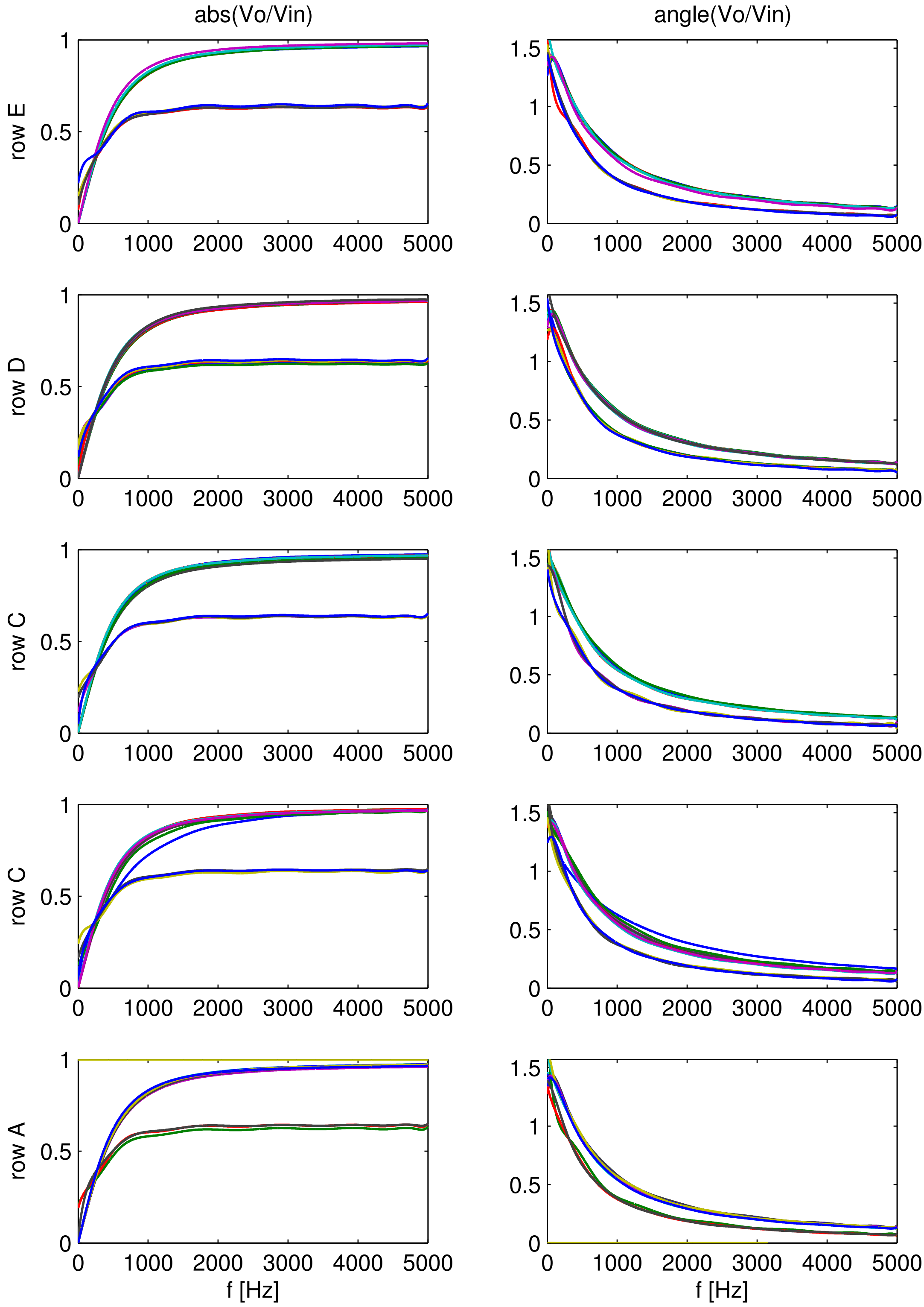

Figure 3.4: Piezoelectric ceramic characterization via high pass filter circuit technique.

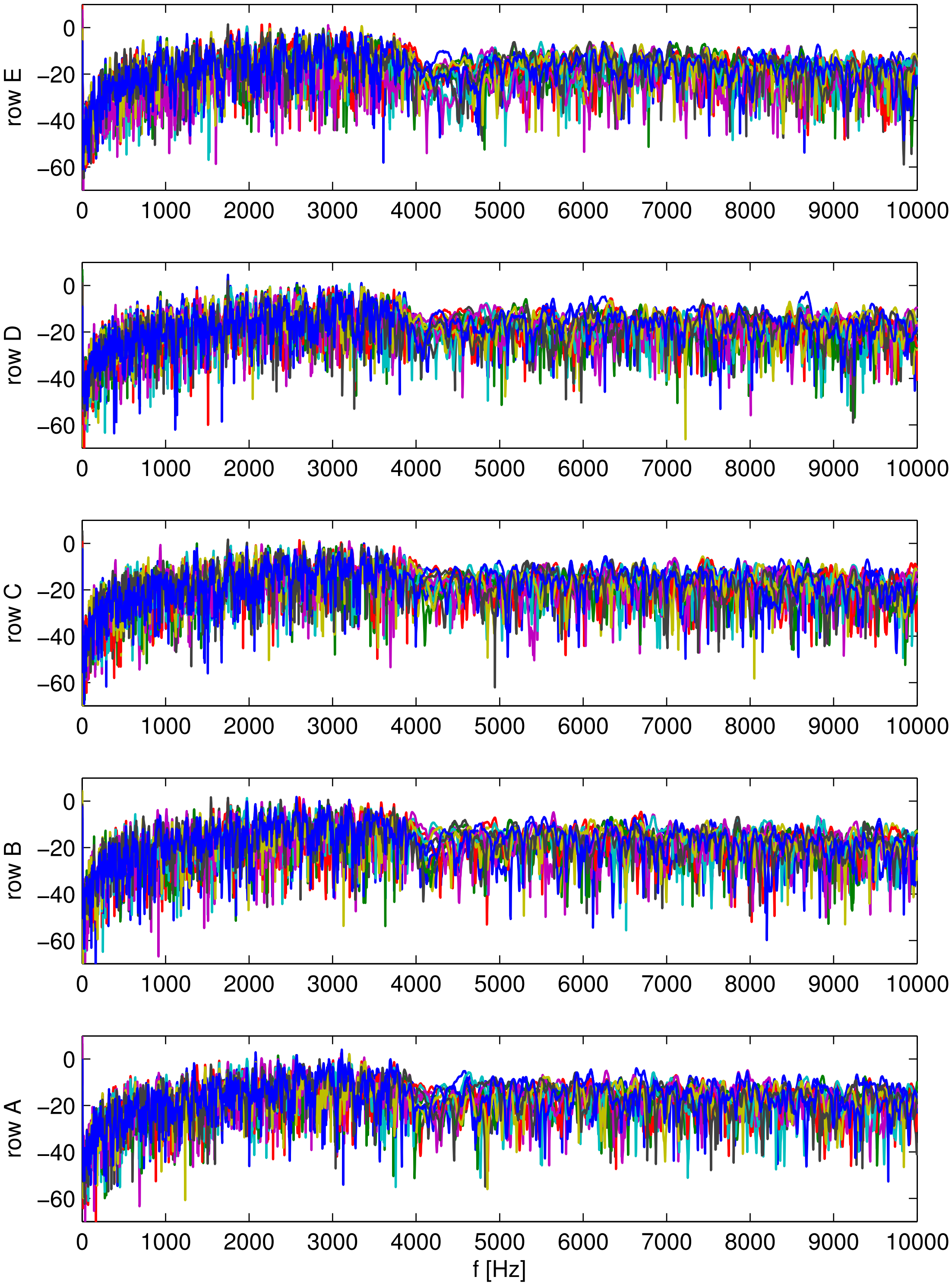

Figure 3.5: Frequency response function of the smart waveguide relating the voltage imposed to each piezoelectric ceramic (input signal) and the acceleration measured in P_2 (output signal). This test allows to verify the correct bonding of the patches.

3.3 Electric Circuit

The results presented in Chapter 2 provide an approach for optimization of the external shunt circuit in terms of the real and the imaginary parts of an imposed synthetic impedance. Two possible behaviors depending on the criterion used in the optimization have been identified. Minimizing the velocity of the energy propagation $Crit_1$ in the region of the active array it is therefore possible to limit the propagation of the wave beyond the active interface. The optimal circuit is also able to modify the transmission properties of the plate increasing the energy reflected from the active interface. The optimal controlling impedance for this approach requires a negative capacitance with a relatively small negative resistance. The negative value of the resistance is due to the control system suppressing the natural damping of the passive structure in order to create a fully reactive periodic system in which a perfect theoretical band gap would exist. As an alternative, choosing a criterion based on exploiting the effect of electrical damping $Crit_2$ it is possible to modify the dynamic properties of the plate by increasing the energy absorption properties of the active interface. Optimization of the electric synthetic impedance parameters for this criterion leads to design of an absorbing metacomposite able to reduce the vibratory energy flowing through it by increasing the power dissipated within the electric circuit. This optimal case requires a negative capacitance and a positive and larger resistance as compared to the reactive interface criterion described above.

However, the required electrical impedances for these two circuit optimization approaches cannot be readily reproduced experimentally because it is not possible to exactly recreate the optimal resistance and capacitance over the whole frequency range of interest. For the work presented here, the layout of the actual circuit implemented for control of the patches is presented in Figure 3.6. This circuit contains a number of passive components, including the resistances R_s, R_2, R_3, R_4, and the capacitance C_2, as well as an active component, specifically, an operational amplifier that is essential for the circuit to reproduce the desired behavior. This specific circuit layout was chosen as opposed to others [36, 38] because of its simplicity and its effectiveness in the frequency range of interest. The impedance of the circuit in Figure 3.6 is determined by the formula

$$Z_{eq}(\omega) = R_s - \frac{R_3 R_2}{R_4 (1 + i\omega R_2 C_2)}. \tag{3.4}$$

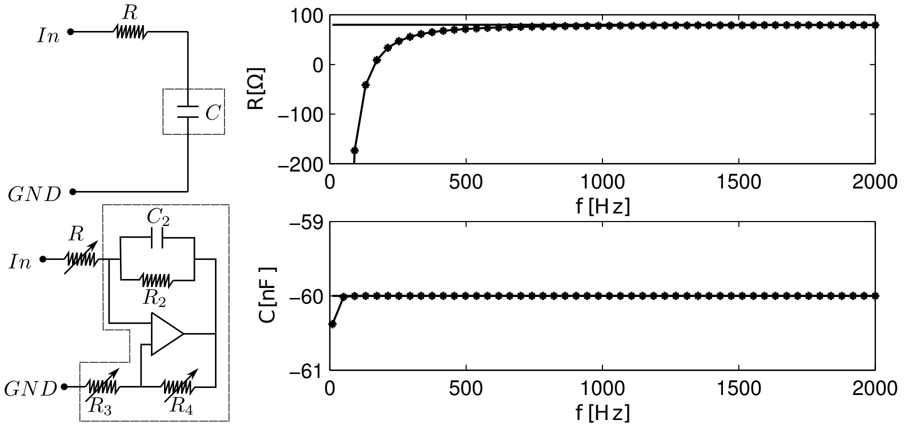

Figure 3.6: Comparison between the desired performance of the ideal circuit and that of the physically implemented circuit. On the left, basic architecture of circuit. On the right, the circuit's impedance depicted in terms of equivalent resistance (top) and equivalent capacitance (bottom).

Figure 3.6 depicts the frequency-dependent behavior of the actual impedance produced by the circuit (Equation 3.4); in the top of the figure is the equivalent resistance (real(Z_{eq})), and at the bottom the equivalent capacitance $(1/\left(-\text{imag}(Z_{eq})\omega\right))$. Both terms vary as a function of the frequency; in particular the resistance at low frequency presents a negative value that can introduce some instability which can degrade the overall performance of the control system. From the practical point of view, the circuit presented in Figure 3.6 is further modified by adding some diodes in order to protect the operational amplifier. The resistances R_3 and R_4 were implemented through a single potentiometer R_{pot} with the aim of simplifying the circuit layout. The negative impedance control technique requires tuning of the synthetic capacitance around the capacitance value of the piezoelectric ceramic at free stress condition [59]; this value is intrinsic to the electromechanical coupling and depends upon the material properties, the geometry of the patches and the plate stiffness. The intrinsic capacitance of the piezoelectric patch can be estimated by measurement using a capacitance meter when the specimen is free of external forces. In the present case the measured nominal patch capacitance is 52 nF. The actual circuit was tuned by varying the position of the potentiometer R_{pot} in small increments from high negative values of the synthetic capacitance to a value very close to the targeted intrinsic capacitance value.

Figure 3.7: Layout measurement system for a single patch.

3.4 Circuit Calibration

The circuit described in the previous section has been tested individually in order to calibrate each circuit's parameter. To do so an aluminum plate with the following dimension 120 × 150 × 1 mm was considered. The plate has a density of 2700 kg/m^3, a Young modulus of 70 GPa and a Poisson ratio of 0.33. The piezoelectric ceramic has the same dimensions and material properties of the piezoelectric ceramics described in table 3.1.

The frequency response function is calculated exciting the plate with a random broadband signal in the lower corner of plate 10 mm away from the edges. The plate's response is measured in the opposite corner by means of a piezoelectric accelerometer.

In Figure 3.8 the uncontrolled and controlled system's response are compared. In the reference configuration the control circuit (citcuit A table 3.2) has a resistance R_s of 40 Ω, a resistance R_2 of 15 $M\Omega$, a potentiometer R_{pot} of 10 $k\Omega$ and a capacitance C_2 of 108 nF. With these parameters

Circuit	R_s $[\Omega]$	C_2 $[nF]$	R_2 $[M\Omega]$	R_4/R_3 $[-]$	R_{pot} $[k\Omega]$	C_{neg} $[nF]$
A	40	108	15	2.04	10	-53
B	400	108	15	2.04	10	-53
C	40	42	15	0.79	10	-53
D	40	108	15	2.04	5	-53
E	40	108	0.68	2.04	10	-53

Table 3.2: Electric circuit's parameters.

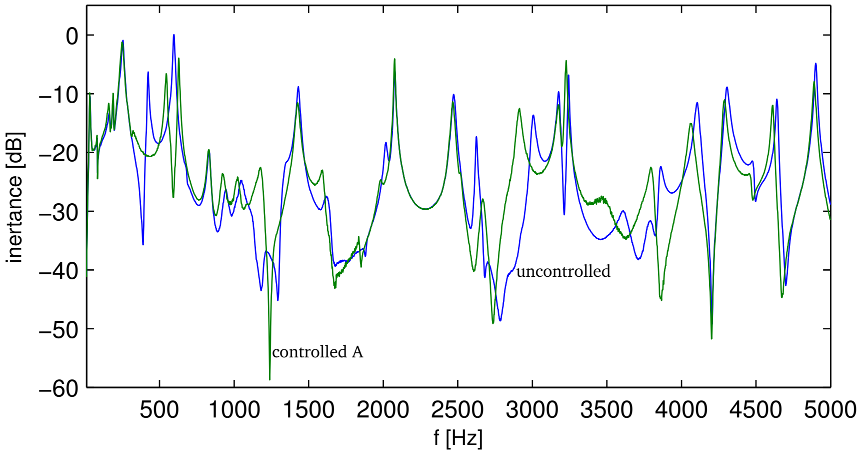

Figure 3.8: Inertance FRF plot of the aluminum plate: uncontrolled (blue line), controlled circuit A (green line).

the system's response is drastically modified as clearly depicted in Figure 3.8 the controlled system tends to shift the resonance peaks toward lower frequency values, this is particularly evident for the resonance placed at 3000, 4200 and 4300 Hz. Another interesting effect is observed at low frequency where in correspondence of the 500 Hz resonance the controlled response shows an hole, the resonant peak is completely suppressed. Likewise the resonance at 550 Hz is also modified, in this case the peak is splitted in two resonances at lower and higher values with respect the uncontrolled peak.

The response is attenuated at 2500 and 3700 Hz, all these evidences indicate that the external circuit is able to modify the dynamic behavior of the controlled structure, in particular a modal restructuring is observed over the whole frequency band.

The design of the control system requires an approach able to take into account all the couplings. The control system is sensitive to the underlying structure and its modal structure. By varying the geometry or the material of the structure the system's response is modified. As an example in Figure 3.9 the response of the uncontrolled and controlled system's is compared using a polycarbonate plate. This plate has the same dimensions of the aluminum specimen. The piezoelectric ceramic has geometric and material properties identical to those presented in table 3.1. The control circuit is tuned imposing the same components values described at the beginning of the section. In spite of this, we observe a modification of the response according to the

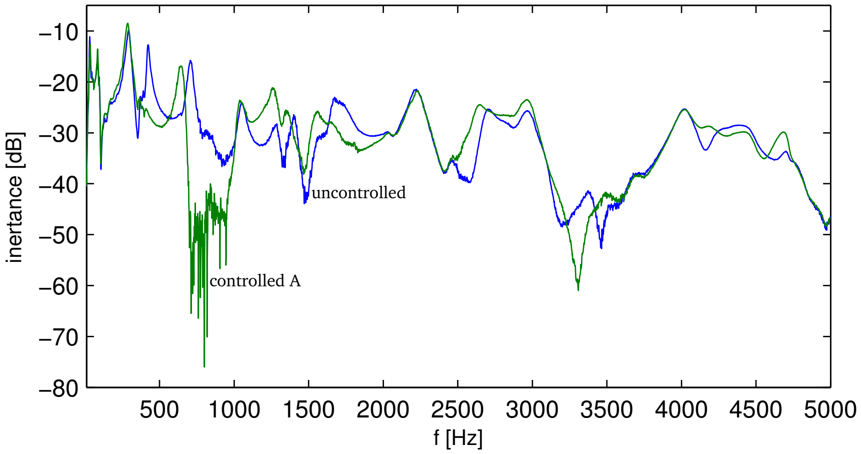

Figure 3.9: Inertance FRF plot of the polycarbonate plate: uncontrolled (blue line), controlled controlled circuit A (green line).

considered support. For example by using a polycarbonate plate we no longer observe the peak splitting effect obtained in Figure 3.8 and the hole reduction effect is even more evident in the $500-1200$ Hz frequency band. Contrary to other control techniques such as resonant circuits which provide almost the same performance (controlling around the tuning frequency) no matter the considered structure. By using a negative capacitance circuit we obtain a response that strongly depends on: the controlled structure, the piezoelectric transducer and the external circuit tuning. The performances of the control system can be modified by varying some component of the external circuit. In figure 3.10 three different configuration have been considered: the modification of the input resistance R_s, the capacitance C_2 and the potentiometer R_{pot}. In the top of Figure 3.10 the variation of the resistance R_s determines a modification of the system response: with small values of resistance R_s the system determines a frequency shifting (green line), an increase of the value of resistance determines an increase of the damping effect evidenced by a decrease of the response in correspondence of the resonances (red line).

This circuit layout is revealed to be very flexible and robust with exception of the stability issues related to the operational amplifier. In fact, the system's response is not affected by the choice of the potentiometer R_{pot} and the capacitance C_2. Analyzing the diagram at the center of Figure 3.10 we observe a system's response slightly modified by the introduction of a capacitance of 24 nF (green line) respect the reference control's response (red line), in both cases we observe a frequency shifting.

At the bottom of Figure 3.10 the uncontrolled and controlled responses are compared, in one case the potentiometer responsible for the tuning of the targeted negative capacitance has a total resistance of 5000 Ω (green line) in the other case 10000 Ω (red line). In both cases the variation in performances is barely appreciable.

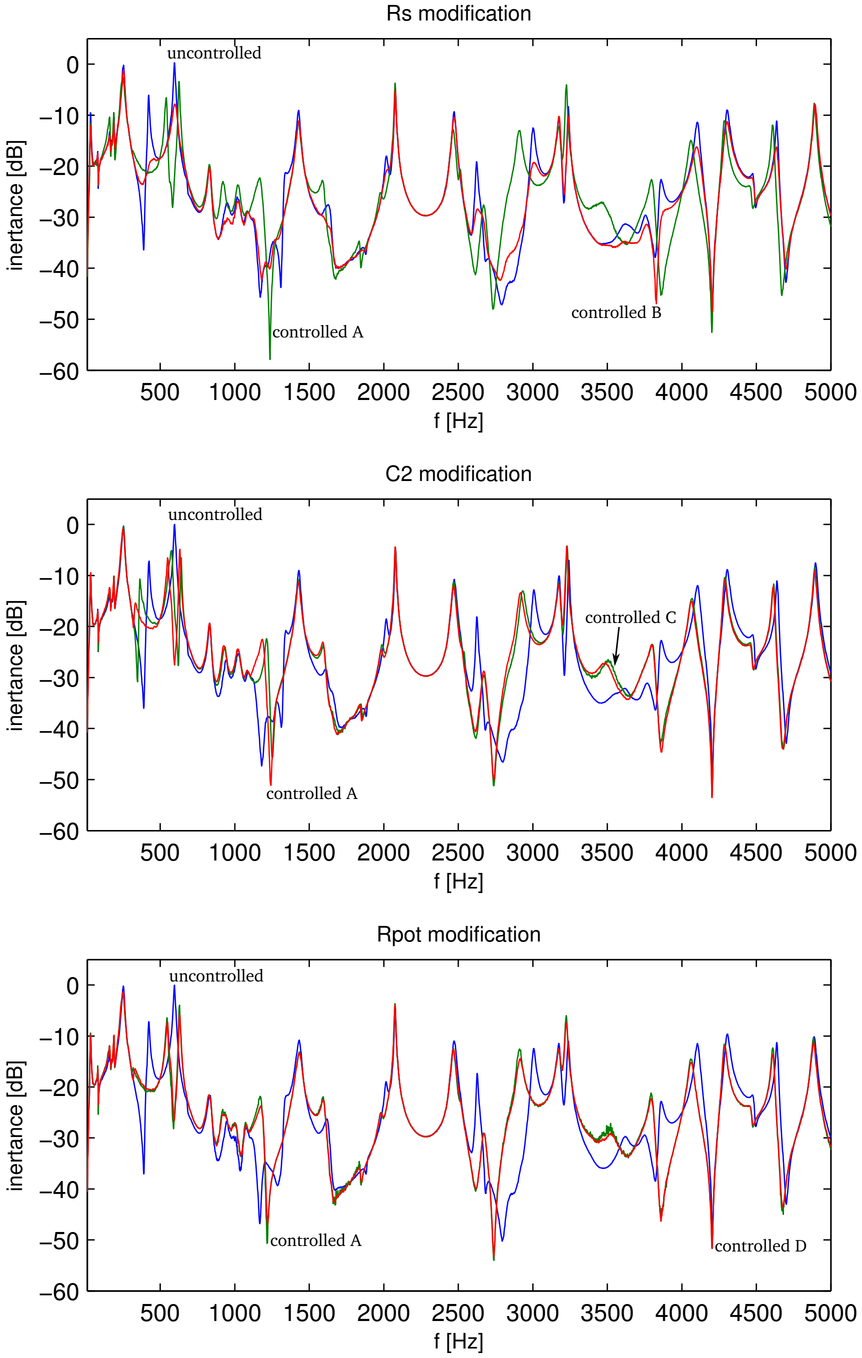

Figure 3.10: Inertance FRF plot of the aluminum plate. Top R_s modification: uncontrolled (blue line), controlled circuit A (green line), controlled circuit B (red line). Center C_2 modification: uncontrolled (blue line), controlled circuit A (red line), controlled circuit C (green line). Bottom R_{pot} modification: uncontrolled (blue line), controlled circuit A (green line), controlled circuit D (red line).

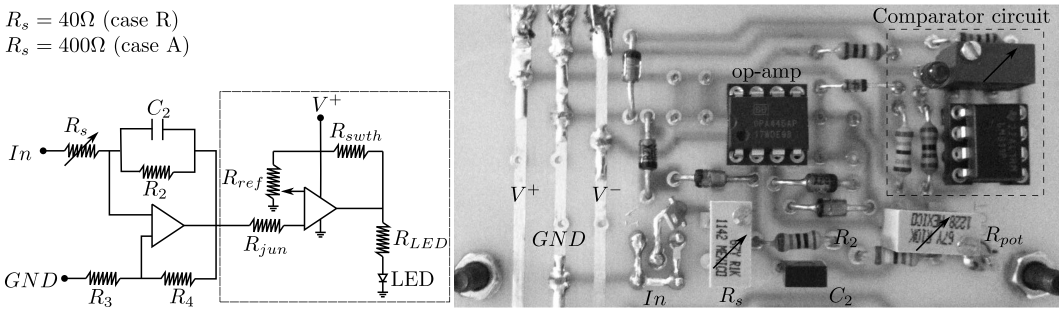

Figure 3.11: Layout of the electric control circuit. Schematic (left), photograph of physical circuit (right).

3.5 Op-Amp Instability Detector

When the external circuit approaches the set-point the system tends to be unstable and an increase of output voltage is observed [59]. If the output voltage reaches the limits of the op-amp's power supply voltage then the operational amplifier saturates and its output clips. In order to mitigate this effect, the circuit was modified by adding a complementary circuit able to detect saturation of the output.

A simple solution is represented by a complementary electric circuit able to detect the voltage variation of the driving signal above a specific threshold value. Once this condition is achieved a light emitting diode (LED) is activated, this architecture could be employed in order to detect the op-amp saturation. The performances of the master circuit strongly depend on the behavior of the operational amplifier, the controlling system is effective as long as the input voltage of operational amplifier is lower than the direct current power supplies voltages V^+ and V^-. This solution is simple and easy to implement but it presents some limitations. First of all the current involved in the overall process is very small. Therefore, the current delivered by the piezoelectric ceramics to the control circuit is not sufficient to excite the light emitting diode. Moreover the nature of the considered circuit impose a strong coupling between the master and the complementary circuit, during the regulation phase a part of the current is deviated toward the LED inducing a degradation of the performances. Another important issue related to this type of circuit is the lack of sensitivity to variation of the input voltage.

However several modification can be introduced in the design of this complementary circuit. In Figure 3.11 is illustrated the updated version of the circuit (on the right). This new design

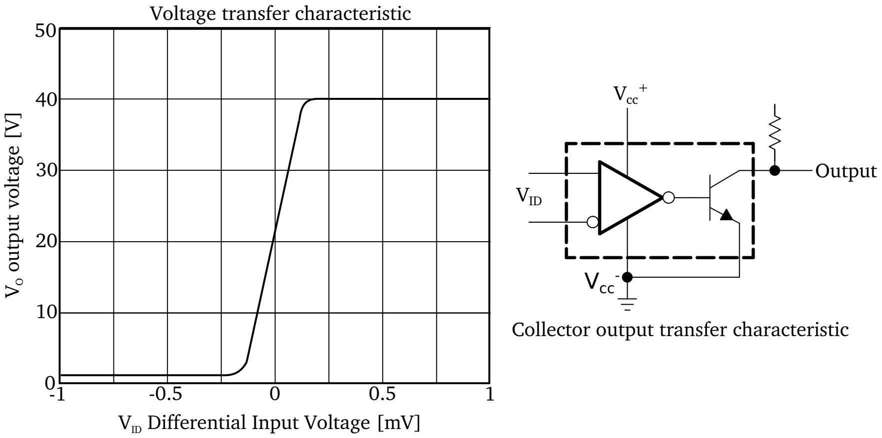

Figure 3.12: Block diagram and voltage characteristic of the comparator.

implies the utilization of another active component namely a differential comparator. This device allow one to compare an input voltage signal V_{in} against a reference voltage V_{ref}. In this particular case the input voltage V_{in} before passing in the non inverting terminal is deprived of its negative component thank to the Zener diode put between the ground and the inlet wire. In this way, at any moment, the comparator can take into account two signals of the same sign, the differential voltage $V_{ID} = V_{in} - V_{ref}$ can consequently be used to verify if the first signals exceed the reference signal. This threshold value V_{ref} can be easily modified using a trimmer, these values span from the saturation value V^+ to 0.

In Figure 3.12 is depicted the functional block diagram of the differential comparator along with its voltage transfer characteristic. In the diagrams is clearly show how the system will behave when a differential voltage V_{ID} of positive sign will occur. The output voltage V_{out} will immediately switch toward the voltage V^+, the current i_{out} prior to entering in the LED will be scaled using the resistance R_{LED} this solution will avoid dangerous working conditions for the other components. For the same reason a resistance R_{swth} is added in the branch connecting the power supply V^+ to the output. The comparator during the periods when is turned off is directly connected to the ground, under this condition the terminal V^+ and V^- are connected through a short circuit, the traversing current can be very high and very harmful for the integrity of the whole circuit.

The comparator circuit has shown to be very effective during the preliminary test, but once directly connected to the master circuit has modified the frequency response in a very negative

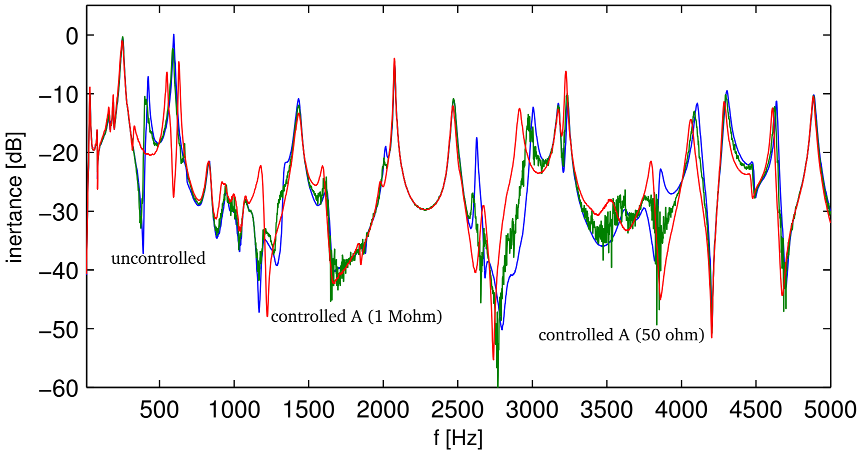

Figure 3.13: Inertance FRF plot of the aluminum plate: uncontrolled (blue line), controlled circuit A with $R_{jun} = 50\ \Omega$ (green line) and $R_{jun} = 1\ M\Omega$ (red line).

way as depicted in Figure 3.13. Comparing the different curves it is evident that best performance are obtained when the control system is deprived of the comparator circuit. However adding a considerably high resistance at the entrance of the comparator circuit it is still possible to obtain a very good response as sketched in Figure 3.13. Using a resistance R_{jun} of 1 $M\Omega$ one obtain a frequency response virtually identical to the reference solution and yet operative, unlike the frequency response for R_{jun} of 10 $M\Omega$. For values of R_{jun} too high the comparator circuit risk to be by-passed. Eventually, when everything is correctly sat-up one can obtain the behavior represented in Figure 3.14. When the output voltage of the operational amplifier is kept lower with respect the saturation voltage the LED emit no light, on the contrary when the the operational amplifier become instable the LED is finally activated warning the user. This specific vibration control technique require that the mechanical instability point is approached keeping the operational amplifier operating. Therefore, it results very convenient to monitoring the evolution of the output voltage of operational amplifier without looking at the oscilloscope during the whole experiment involving 75 actuator and circuits. In this manner will be a very straightforward task the detection of the occurring instability due to the interaction between two or more different piezoelectric shunt. This simple solution is very helpful since it allows one to detect this particular source of instability, therefore speeding the circuit tuning process. This feature becomes very useful in this context, where a large number of actuators is required. For

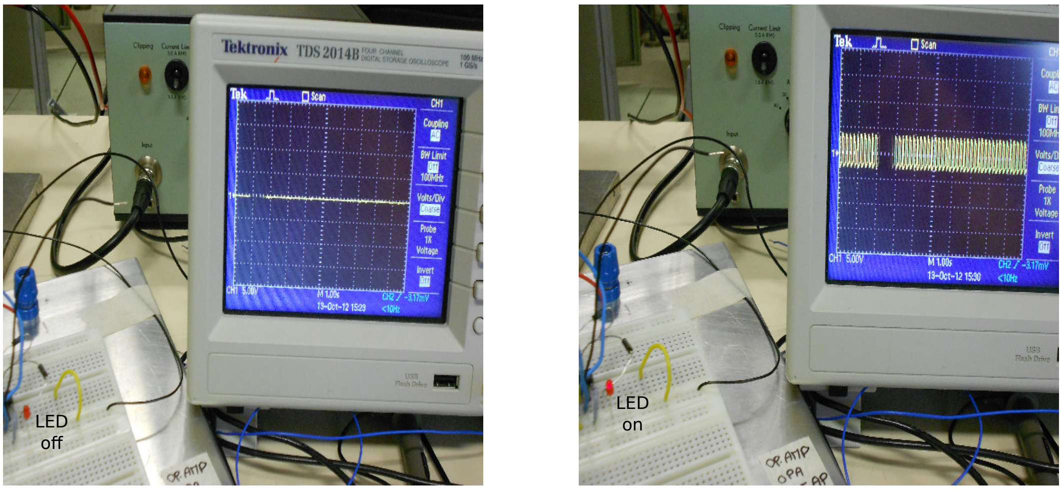

Figure 3.14: Op-Amp output voltage overload detector: operating condition (unsaturated signal and LED off), overload condition (saturated signal and LED on).

example, when several piezoelectric patches are excited, a loss of performance can be observed due to the electromechanical coupling occurring between adjacent patches. In this case, observing the state of the LEDs on the control panel it is possible to correctly and efficiently reset each control circuit.

For the work at hand, two configurations of the of circuit have been implemented in order to program two different vibroacoustic behaviors:

- Case 1 corresponding to a lightly-damped, reactive or reflective configuration, is obtained by tuning the negative capacitance C_{neg} very close to the instability point that corresponds to the opposite of the intrinsic capacitance of the piezoelectric ($C_{neg} = -62nF$). The resistance R_s is set to a small positive value able to reproduce the desired behavior (wave reflection) and still ensuring the stability of the control system ($R_s = 40\Omega$). In the context of shunted piezoelectrics, this control case implements a negative stiffness; in the absence of damping, this yields a more reactive interface than otherwise.

- Case 2: corresponding to an absorbing configuration, and is obtained by tuning the negative capacitance C_{neg} with the same value of case 1. The energy absorption enhancement is then obtained by imposing a larger resistance R_s ($R_s = 400\Omega$) at the input to the negative impedance shunt.

3.6 Circuit Stability

The reasons behind shunt parameters which yield unstable a negative capacitance circuit need to be identified and modeled to aid in the prediction of vibration suppression. A process is developed here that predicts the magnitude of negative capacitance that is attainable experimentally given the measured electrical impedance of a patch and uncontrolled voltage response. Two problems that limit the effectiveness of the overall control system are explored: the issues surrounding the variation in patch impedance and the voltage limitations of the op-amp. This section first defines the stability of the shunt, then discusses the impact of the voltage output of the op-amp. An experimental test structure is introduced and the variation in patch impedance is quantified. Finally, the results and analysis are given.

3.6.1 Stability Condition

To obtain maximum performance, appropriate circuit component values must be chosen to reach the necessary negative capacitance. The values of these components are limited by concerns regarding the stability of the circuit, where a stable circuit is considered a circuit configuration that has a non-saturated output. To determine stability of the circuit, one must consider the two following requirements [10]:

- For Direct Current signals there must be feedback current to the inverting terminal
- The voltage gain down the positive feedback path must be smaller than the voltage gain down the negative feedback path

The first condition prevents a bias voltage occurring that would cause the circuit output to drift until the output equaled the supply voltage. The second condition ensures that the harmonic feedback is stable according to the method proposed by Date et al. [30]. Date analyzed the negative impedance converter circuit in Figure 3.7, where the input to both the inverting and non-inverting terminals of the op-amp are considered as ideal voltage dividers from the output voltage to ground. The voltage gain for the non-inverting path is

$$V^{+} = \frac{Z_3}{Z_3 + Z_4} V_{out}. \tag{3.5}$$

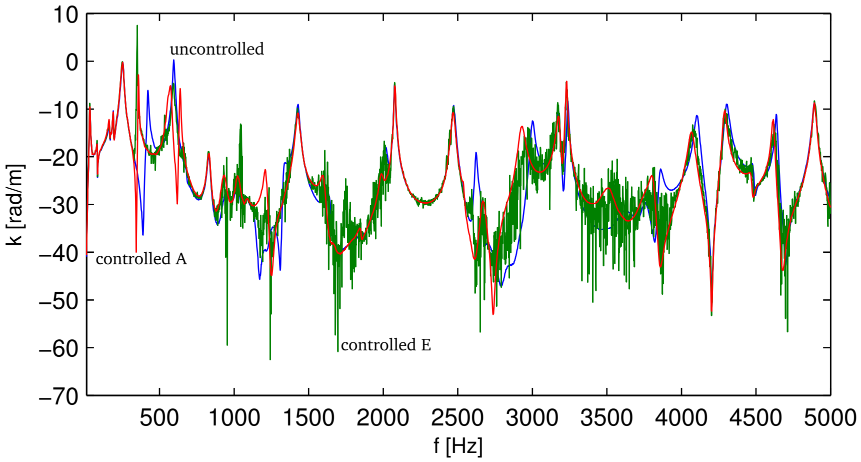

Figure 3.15: Inertance FRF plot of the aluminum plate: uncontrolled (blue line), controlled circuit A (red line) and controlled circuit E (green line).

The voltage gain for the inverting path is

$$V^{-} = \frac{Z_1}{Z_1 + Z_2} V_{out}. \tag{3.6}$$

The third voltage relationship considers the voltage difference across the inputs which is

$$\Delta V = V^{+} - V^{-} = \left(\frac{Z_3}{Z_3 + Z_4} - \frac{Z_1}{Z_1 + Z_2} \right) V_{out} \tag{3.7}$$

The voltage gain down the inverting path must be greater than the gain down the non-inverting path, thus, the sign of the coefficient of V_{out} in equation (3.7) must be negative

$$\Delta V = V^{+} - V^{-} = \left(\frac{Z_3}{Z_3 + Z_4} - \frac{Z_1}{Z_1 + Z_2} \right) V_{out} < 0 \tag{3.8}$$

Therefore, equation (3.8) can be simplified to

$$\frac{Z_3}{Z_3 + Z_4} - \frac{Z_1}{Z_1 + Z_2} < 0 \tag{3.9}$$

which can be reduced to

$$\frac{Z_2}{Z_1} - \frac{Z_4}{Z_3} < 0 \tag{3.10}$$

A stable circuit will have the expression above hold for all frequencies. If it is assumed for a negative capacitance circuit that both Z_1 and Z_2 are ideal capacitors only, the stability condition becomes

$$\frac{C_p}{C_2} - \frac{R_4}{R_3} < 0 \tag{3.11}$$

where C_p is the capacitance of the piezoelectric patch and C_2 is the reference capacitor, which is the definition of stability that is specified by Date et al. The determination of a stable circuit is straightforward because equation (3.11) is independent of frequency and purely real. This will be considered the traditional estimation of instability. Yet, if all the components of the circuit are included in Equation (3.11), the stability condition becomes

$$\frac{1}{(Z_p + R_s)(i\omega C_2 + 1/R_2)} - \frac{R_4}{R_3} < 0 \tag{3.12}$$

where Z_p is the frequency-dependent patch impedance, R_s is the series resistance and R_2 is the reference resistor in parallel with the reference capacitor C_2. The left-hand side of the expression is both frequency-dependent and complex while the right-hand side is purely real. The stability, therefore, needs to be defined in terms of a complex quantity. The stability condition is

$$angle\left(\frac{1}{(Z_p + R_s)(i\omega C_2 + 1/R_2)} - \frac{R_4}{R_3}\right) < 0 \tag{3.13}$$

which is analogous to the requirement in control theory that requires the poles be located in the left-half of the complex plane.

Equation (3.12) can be used to predict the values of negative capacitance and series resistance for which the circuit will be stable for a given patch.

3.7 Conclusions

This chapter has provided the basic tools necessary to correctly design a negative capacitance shunt. A negative capacitance once combined with a resistor determines large changes in both the stiffness and attenuation properties. Using its frequency dependent characteristics, the shunt can be designed to achieve certain control objectives.

The physical implementation of a negative capacitance circuit including a prototype circuit and the method for implementation was also presented. The components of the smart interface are individually analyzed in order to select the most appropriate set of parameters. Particular emphasis is given to the analysis of the electronic circuit synthesizing the negative capacitance effect. Experimental investigations shown that through selection of the passive elements of a negative capacitance inverter, the efficiency of the shunt can be increased.

Finally, a prediction method for determining the operating range of a negative capacitance shunt was developed. By measuring the impedance of the patch, the requirements of circuit stability and the op-amp voltage output limitations were modeled and predicted along with general recommendations on how shunt component values should be selected in order to increase control capabilities.

Chapter 4

Performances of the Adaptive Metacomposite

Overview

This study presents an experimental investigations of the application of a periodic array of shunted piezoelectric patches with negative capacitance for the broadband control of waves propagating on a flexible plate.

A 15×5 array of piezoelectric patches is bonded onto the top surface of a freely-supported rectangular plate. The patch array is intended to serve as an active interface between two regions of the plate, where one region has an input disturbance force and the other does not. Each patch is shunted through a single circuit, reproducing a resistance in series with a negative capacitance. The magnitude of the reactive part of the negative shunting impedance is tuned close to the intrinsic capacitance of the piezoelectric patch. The real part is adjusted for either light damping so as to induce a reactive (reflective) response, or with heavy damping to induce greater absorption.

The experimental responses of the system equipped with this active interface display a strong attenuation or reflection of vibrations, depending on the shunt resistance, over a large frequency range, including the mid-frequency regime.

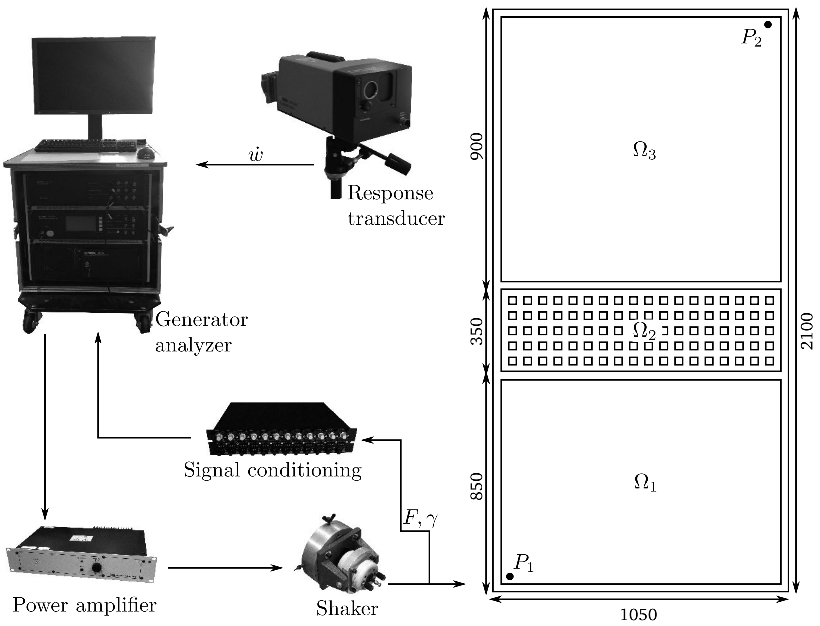

Figure 4.1: Layout of FRF measurement system. P_1 is the force input position, while P_2 used for a representative single-point transfer mobility measurement.

4.1 Experimental Set-up

The structure of interest, described in Chapter 3, consists of an aluminum plate equipped with 75 piezoelectric actuators connected to external circuits and arranged so as to form a periodic array of 5×15 units. Standard epoxy glue was used to bond the piezoelectric ceramics to the top surface of the plate.

Elastic waves are excited by a shaker located in the lower corner of the plate, 840 *mm* away from the active interface at the point labelled P_1 in Figure 4.1. The input transducer is driven by an input signal consisting of a random broad-band excitation and amplified by an LDS power amplifier. The response of the structure to the input disturbance and action of the active interface was measured with a scanning laser vibrometer (Polytec PSV-400). Measurements were conducted over a grid of 37×81 scan points with a spatial resolution of 20 *mm* in the horizontal and vertical directions. At each grid point, the laser measured the time history of the out-of-plane velocity $\dot{w}(x, y, t)$. The measured velocity signal was processed using a Fourier transform; the obtained signal $\dot{W}(x, y, \omega)$ depends on the coordinates x, y and the angular frequency ω. By means of an impedance head the input excitation force was also measured. The

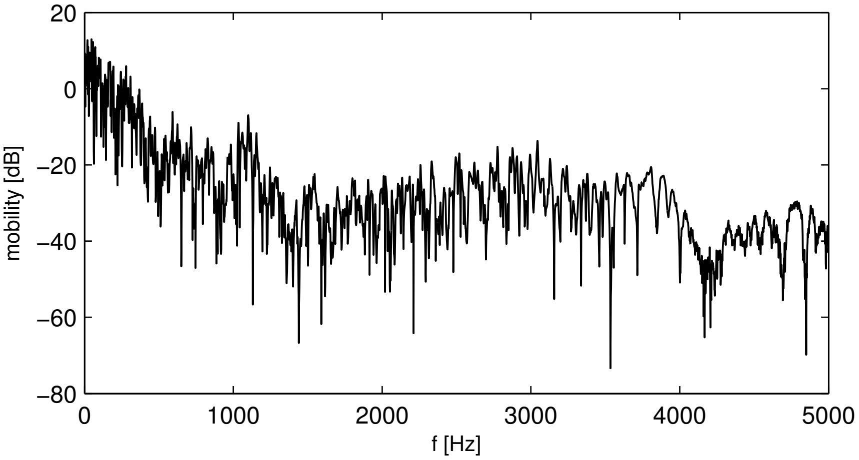

Figure 4.2: Reference frequency response function at the point P_2 (control off).

Fourier transformed signals $F(\omega)$ and $\Gamma(\omega)$, representing the excitation force and the acceleration at the force input point labeled as P_1 on Figure 4.1, were used for estimation of the power injected into the system. Another quantity of interest obtained during the post-processing is the mobility function given by

$$Y(x, y, \omega) = \frac{\dot{W}(x, y, \omega)}{F(\omega)}. \tag{4.1}$$

4.2 Results and Discussions

Selected experimental results are presented here in order to demonstrate the effectiveness of the proposed active interface and distributed control technique. First, the results obtained performing a single-point mobility measurement will be presented for introductory purposes. A full-field measurement will further illustrate the main features of the control system and finally some consideration of the energetics of the approach will conclude the section, characterizing the performance of the considered metacomposite.

4.2.1 Single-point Mobility Measurement

Mobility measurements permits a ready assessment of some specific features of the system. Figure 4.2 depicts the plate's transfer mobility frequency response function, measured at point P_2 of the controlled plate (Figure 4.1). The mobility function is measured over the frequency range of $0 - 5000$ Hz. In the low frequency range, $0 - 500$ Hz, the system shows a degradation of coherence; therefore, the value of the mobility function is less reliable in this frequency region. For this reason, in the following section, the analysis of the system for higher frequency values will be emphasized, focusing in particular on the $500 - 5000$ Hz frequency range. Moreover, the system's response function clearly shows a high modal density corresponding to mid-frequency behavior that makes classical control methods difficult to apply.

4.2.2 Third Octave Mobility Comparison

Due to the high modal density, comparing the different response functions while keeping the same frequency resolution will be quite problematic due to the action of the control restructuring the modal behavior of the plate. For this reason, a different approach has been employed. Each frequency response function or metric of interest (e.g., loss factor) has been expressed in terms of band-averaged third octave bands to lessen the impact of modal restructuring on the presentation of results, while still permitting assessment of important system features (an analysis of the modal density of the plate indicated that there were at least three modes per third octave band starting with the 40 Hz band).

Figure 4.3 depicts the difference in the third-octave band averaged mobility magnitude in dB between the reference response (control off) to the controlled response for the two cases presented in the previous section (cases 1 and 2). Positive values correspond to an attenuation of the system's response. The figure presents two plots: the upper plot is the difference in input mobility at the excitation point P_1, while the lower plot is the difference in the transfer mobility between the input point P_1 and a response point P_2 (Figure 4.1). The response point P_2 considered here is at the opposite corner of the plate from the input and located downstream with respect to the active interface. Considering the input mobility, the impact of the control for both cases is relatively minor, on the order of $\pm$ 1 dB in all bands. But, considering the response at P_2 on the downstream side of the active interface, we observe an enhancement of control capabilities in specific frequency ranges. For example in case 1 the performances of the control system, in terms of vibration supression, is almost always significantly lower compared to the case 2 except around 2000 Hz. For case 2 better performance is obtained, above about 100 Hz the system systematically adds at least 5 dB reduction. Some bands display significantly better results; for

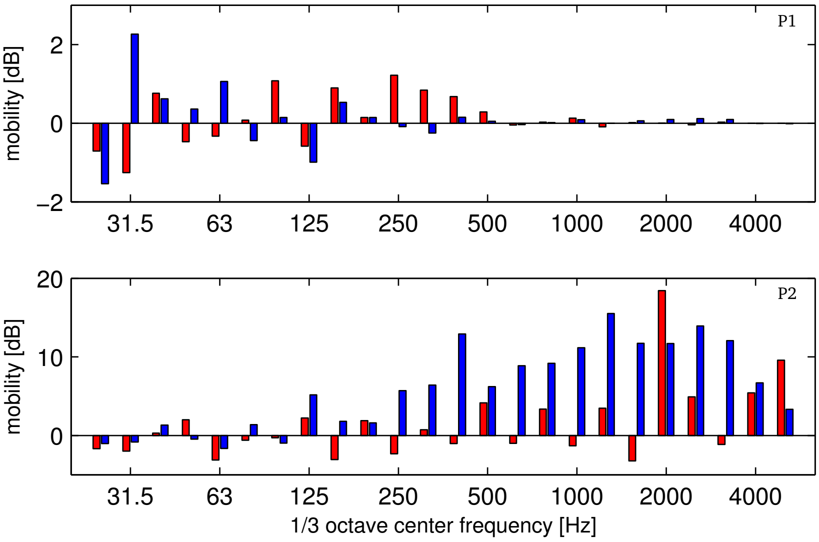

Figure 4.3: Difference in third-octave band averaged mobility magnitude between response with control off and responses for each case with control on, over the frequency range spanning third octave bands from 31.5-4000 Hz. (Top) mobility difference at P_1 located in the lower region of the plate: case 1 (red) vs. case 2 (blue); (bottom) mobility difference at P_2 located in the upper region of the plate: case 1 (red) vs. case 2 (blue). Positive values mean a reduction of the system response.

example, a 15 dB reduction around 2000 Hz for case 1, the most reactive control configuration. The control for case 2, the absorptive control configuration, does not achieve as great a maximum single-band control as does case 1 at 2000 Hz, but it exhibits a much broader frequency range of control. It is clear that in the frequency band $50 - 5000$ Hz the control system works effectively, reducing the magnitude of the vibrations. The frequency band where the control system actually reduces the vibrations depends on the circuit's configuration; small values of the input shunt resistance R_s (case 1) impact higher frequency values in a narrow band. Larger values of the input shunt resistance R_s (case 2) impact a broader frequency range.

These results illustrate an inherent difference between the control configurations between the two cases; the more reactive the boundary, the greater the possible control but in a relatively narrow frequency band; the more absorptive the boundary, the greater the bandwidth of control with some reduction of maximum achievable control. Further, these results show the effectiveness of the proposed control strategies, and illustrates a basis for selection between them for a given application; if one seeks to control a narrow-band disturbance, then the reactive control configuration would be appropriate. If the disturbance is broad-band, then the absorptive control would be appropriate.

4.2.3 Full-field Mobility Measurement

The results presented in the previous section can not fully demonstrate the impact or effectiveness of the control system because they are limited to selected single point measurements. Figure 4.4 presents measurements of the plate's mobility as a function of the spatial coordinates x and y at 25 Hz and at 1680 Hz. The top row of images presents, left to right, the mobility of the plate for the reference measurement (control off), the field with the case 1 control and the field for the case 2 control, all at 25 Hz. The control system acts differently according to the circuit's setting. For the case 2 control configuration the behavior of the plate is not affected by the control system, and the plate's operational deflection shape is unmodified, with only an incremental reduction of the vibration amplitude observed. In contrast, for case 1, the dynamic response of the plate is modified, and a different response shape is observed due to modal restructuring. The bottom of Figure 4.4 presents the mobility of the plate at 1680 Hz for the same configurations as above. The response of the plate is decreased in a uniform fashion over the whole surface of the plate. This reduction is particularly evident for case 2, where the response is uniformly decreased by about 15 dB. In case 1 this effect is less significant.

4.2.4 Loss Factor Estimation

It is informative to consider the loss factor exhibited in the plate response as a function of the control configuration. Estimation of the loss factor requires a measure of the time-averaged power input to the system, and the total time-averaged energy of the system (potential plus kinetic energy) [16]. The experimental set-up allows the measurement of the input force and the response velocity at the driven point, along with the velocity field over the entire plate. Using this information, it is possible to calculate the direct component (time-averaged) of the power flow into the system [14]:

$$P_0 = real\left(\frac{1}{2}F \cdot v^*\right). \tag{4.2}$$

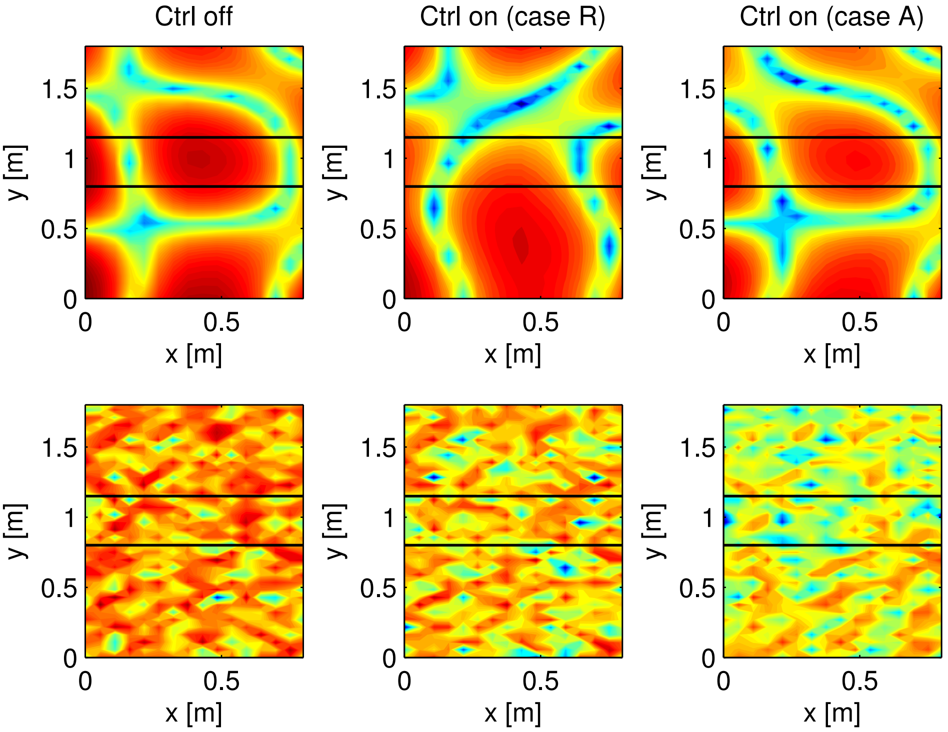

Figure 4.4: Control off vs. control on full-field mobility measurement. (Top) response at 25 Hz; (bottom) response at 1680 Hz. Horizontal black lines indicate location of active interface.

Further, the integration of the velocity field over the entire surface of the plate yields an estimate of the plate's time-averaged kinetic energy,

$$T_0 = \int_\Omega \rho v v^* dV, \tag{4.3}$$

and the time-averaged total energy E_0,

$$E_0 = T_0 + U_0 \simeq 2T_0. \tag{4.4}$$

E_0 is estimated by using SEA hypotheses that remain valid only at the resonance or for higher frequencies where the modal density is sufficiently high [14]. The loss factor of the plate is then calculated by

$$\eta = \frac{P_0}{\omega E_0}, \tag{4.5}$$

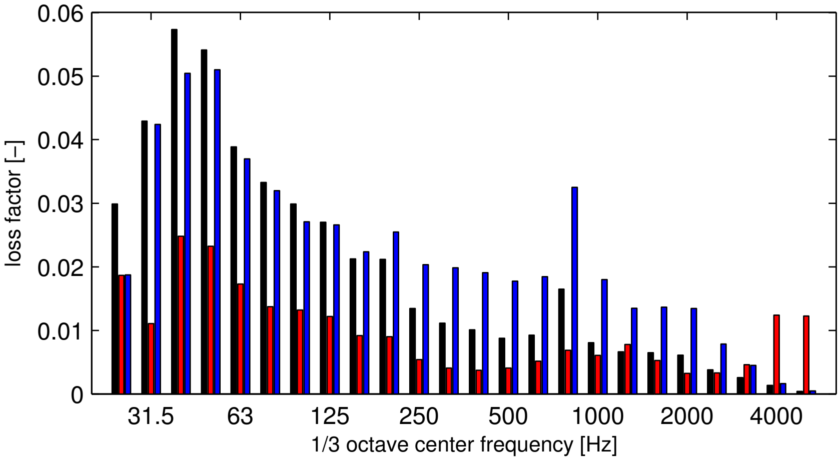

Figure 4.5: 1/3 octave band averaged loss factor of the structure: (black) control off; (red) control on case 1; (blue) control on case 2.

where P_0 also represents the time-averaged power dissipated in the system.

Figure 4.5 summarizes the estimated loss factor for the three different control conditions considered here; control off, case 1, and case 2. As with the mobility measurements presented earlier, the loss factor data is presented here in terms of third octave band averaged values. For the control off case, the loss factor is no more than 0.015 below 1000 Hz, and falls to lower values at high frequencies. For the reactive, low-damping configuration of case 1, the system is less damped than the uncontrolled configuration in all bands below 4000 Hz. For the 4000 Hz band and above, the damping increases from significantly less than 0.01 to slightly greater than 0.01. This behavior is a consequence of the frequency-dependent reactive nature of the control suppressing the plate's loss factor at lower frequencies, while the still non-zero dissipation of the control adds damping at the higher frequencies. For the higher resistance R_s configuration of case 2, the system is more strongly damped over the whole frequency band of interest. However, the best results are obtained over the bands from 200 Hz to 2500 Hz, where the loss factor with the control on exceeds that with the control off. Similar results where obtained by Beck [11] on a beam structure. To further illustrate the impact of the control on the system, consider Figure 4.6 which presents the difference, $\Delta\eta$, between the loss factors for each of the controlled systems (case 1 and 2) and the loss factor for the corresponding third-octave band for the control off condition. A positive value of $\Delta\eta$ means that the control system increased the loss factor for

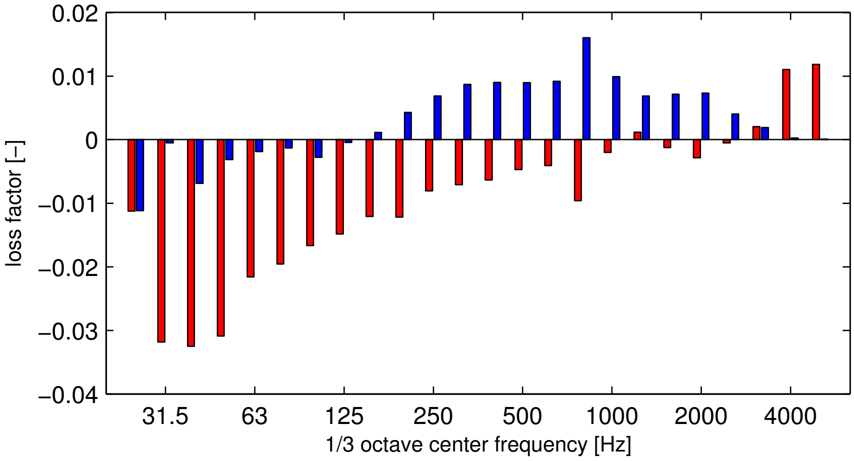

Figure 4.6: Difference in 1/3 octave band averaged loss factor between the control on and control off cases: (red) control on case 1 vs. control off; (blue) control on case 2 vs. control off.

the band, while negative value means that the control system has reduced the loss factor for the band. This presentation clearly brings out that the reactive configuration of case 1 reduces the loss factor for frequencies below 2000 Hz and increases it for the 4000 Hz and higher bands. The absorptive configuration of case 2 does decrease the loss factor below 125 Hz, but increases the loss factor from 200 Hz through the 3500 Hz band, reflecting the broader bandwidth of control of case 2.

4.2.5 Kinetic Energy Distribution

The loss factor evaluation presented in the previous section can be used to evaluate the fraction of energy dissipated in each cycle of vibration, but no information about the modification of the plate's internal dynamics within each of the regions of the plate (upstream of the active interface, within the active interface, and downstream of the active interface) can be obtained. In order to address this aspect of the influence of the control scheme, if one computes the time-averaged kinetic energy over a subdomain of the plate Ω_i, it is possible to evaluate the kinetic energy distribution within the system by calculating the ratio

$$\tau_i = \frac{T_0^{\Omega_i}}{T_0^{\Omega_{tot}}} \tag{4.6}$$

where Ω_{tot} represents the plate's total area and Ω_i the different sub-domains of interest on the plate; below the active interface (containing the force disturbance input point), within the active, interface, and above the active interface. These subdomains are labeled on Figure 4.1. Note that in proportion to the total area of the plate, each subdomain's fraction of the plate area are 0.33, 0.17, 0.50, for the upstream, interface, and downstream areas, respectively.
A clear depiction of the impact of the active interface may be obtained by considering the area distribution of kinetic energy (essentially plotting the square of the local velocity on the plate) as depicted in Figure 4.7. The top row of plots depict the kinetic energy distribution among the three control configurations at 2500 Hz. On the left, (control off) the kinetic energy is evenly spread over the entire plate. In the middle, the system's response is slightly modified by the low-damping, low resistance R_s control case 1. In contrast, as a result of increasing the value of the resistance R_s for case 2, there by increasing the damping, the kinetic energy distribution of the plate is clearly modified; the response is most strongly confined to the portion of the plate below the active interface. Considering a higher frequency example, for instance 3000 Hz as depicted in the lower plots of Figure 4.7, the behavior of the system is radically modified. For the lightly-damped control case 1, the vibratory energy of the plate is even more noticeably confined in the upstream subdomain Ω_1 as compared to the response at 2500 Hz. In fact the vibration amplitude is increased in the upstream region for case 1 as compared to the control off case. For the more heavily-damped control of case 2, the reflective behavior is no longer present, and the driving control mechanism is a dominantly dissipative effect that makes the kinetic energy field weaker everywhere through suppression of a reactive vibratory response.

Figure 4.8 depicts the difference in the kinetic energy ratio τ calculated for each of the subdomains of interest, and for each control circuit configuration with respect to the control off configuration. Negative values for the difference indicate that the kinetic energy has decreased in the subdomain relative to the control off configuration, while positive values indicates it has increased. While not evident from Figure 4.8, with the control off the kinetic energy ratio was roughly uniform with frequency and proportional to the area of each subdomain, as would be expected for a diffuse band-averaged wavefield. However, with the control on the vibratory energy of the plate is distributed differently within the plate as compared to the control off condition and differently for each control configuration.

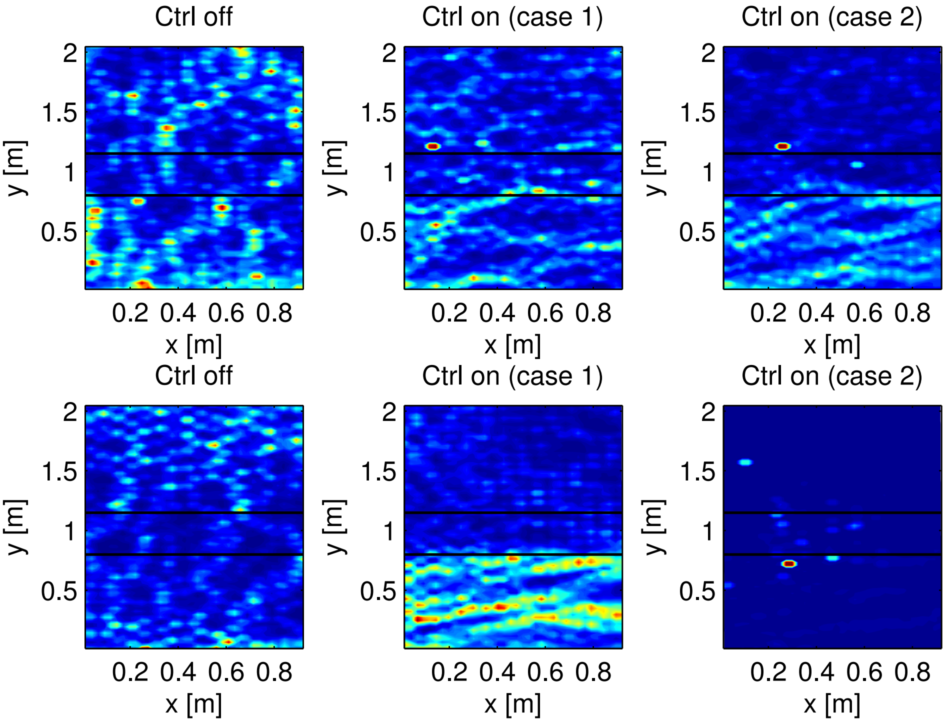

Figure 4.7: Plate kinetic energy field: (left) control off, (center) control on case 1, (right) control on case 2. (Top) 2500 Hz, (bottom) 3000 Hz. Horizontal black lines indicate location of active interface.

Considering each subdomain in turn, starting with the downstream area of the plate, represented by the top plot of Figure 4.8, with the case 1 control there is little impact on the kinetic energy distribution until above 3000 Hz, where the increasingly negative values of the difference indicates that less of the plate's total kinetic energy is in the downstream subdomain. However, for the higher-damped case 2 control, the negative values of difference in the kinetic energy distribution ratio within the downstream subdomain is reduced over a much broader frequency span from below 500 Hz to above 3000 Hz. An implication of the reduction of the kinetic energy distribution ratio, relative to the total for these two control cases, is that the kinetic energy distribution ratio had to increase elsewhere on the plate, that is, the energy was localized elsewhere.

Considering the subdomain comprising the active interface, addressed in the middle plot of Figure 4.8, the kinetic energy distribution within this subdomain as reflected by the plotted difference in the ratio is relatively unaffected to the state and configuration of the control.

Finally, considering the upstream subdomain containing the input force, addressed in the bottom plot of Figure 4.8, the behavior is effectively opposite of what is observed in the downstream subdomain, as it must in consideration of conservation of energy. For both control configuration cases, the fraction of the total kinetic energy of the plate is greater in this upstream subdomain, clearly indicating that the active interface is serving to isolate the downstream section from the energy in the upstream section. The degree of that isolation depends on the form of the control, with the absorbing configuration, case 2, yielding a greater degree of isolation over most of the frequency range, up to approximately 3000 Hz. Above 3000 Hz the case 1 configuration yields better isolation as compared to case 2; note that this frequency dependence is also reflected in the loss factors for these two cases, as discussed in the previous section.

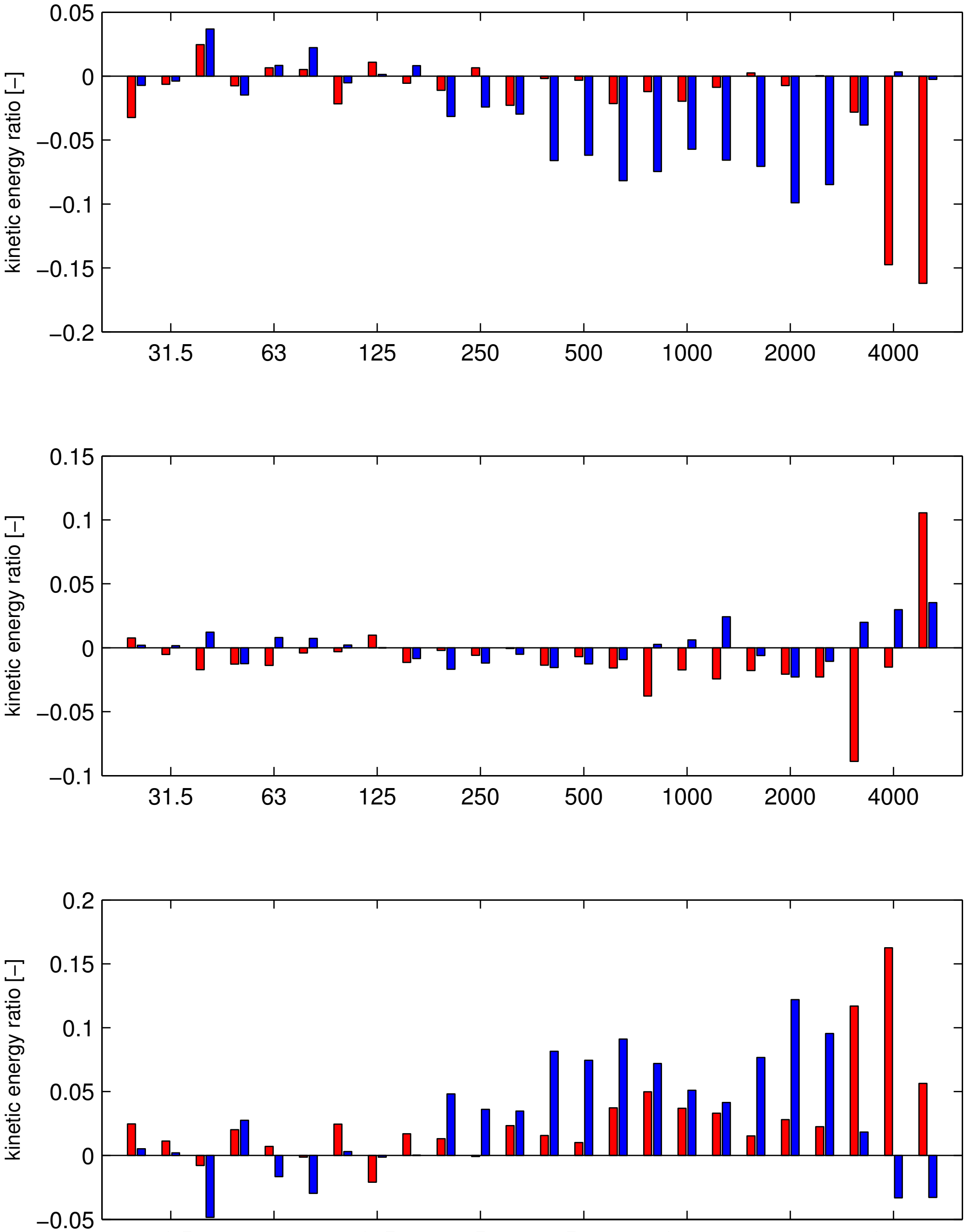

Figure 4.8: Difference in 1/3 octave band ratio of averaged kinetic energy distribution in each subdomain to the total kinetic energy: (red) control on case 1; (blue) control on case 2. (Top) subdomain 3, downstream of interface; (middle) subdomain 2, active interface; (bottom) subdomain 1, upstream of interface

.

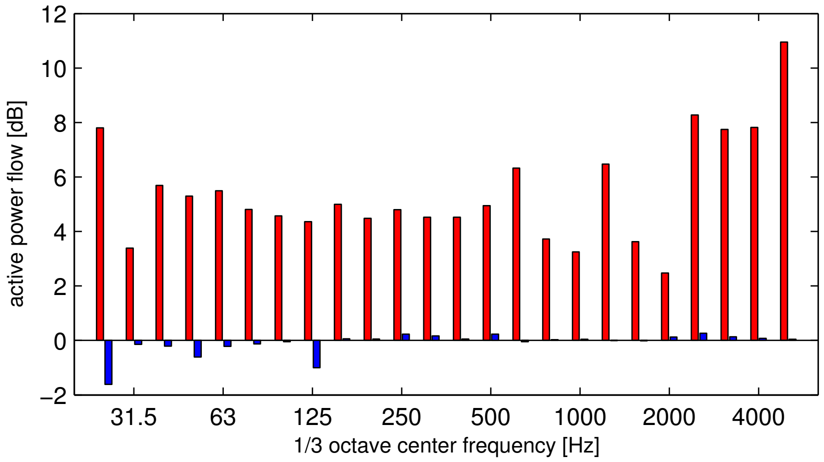

Figure 4.9: 1/3 octave band averaged and time averaged real power flow into the plate: (red) control on case 1; (blue) control on case 2.

4.2.6 Power Injected

Figure 4.9 depicts the frequency behavior of difference in the real injected power flow into the system in third octaves, while Figure 4.10 depicts the difference in the reactive power. As previously, the depiction is in terms of the difference between the control on cases and the control off case. As compared to the power injected with the control off, the power injection behavior is significantly different for the two control cases. For the reactive condition, case 1, the real and reactive input power actually increases, indicating a change in the input impedance presented to the forcing. For the damped case 2, there is almost no change in the real and reactive input power, indicating effectively no change to the input impedance.

4.3 Conclusions

The control capability of an active interface between two regions of a plate with either a lightly-damped or more heavily damped configuration has been demonstrated through experimental evidence.

The active interface and control technique strongly modifies the energy distribution properties of the structure. The introduction of the active interface allows one to enhance the absorbing or reflecting properties of the plate considered as a waveguide, particularly for higher frequencies. These properties strongly depend on the configuration of the control circuit, between lightly

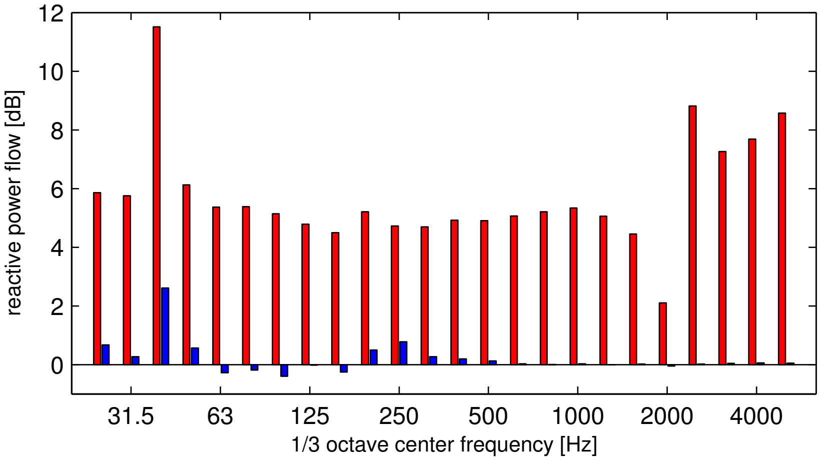

Figure 4.10: Difference in 1/3 octave band averaged time peak reactive power flow into the plate: (red) control on case 1; (blue) control on case 2.

damped and more heavily damped. Through analysis of these two control configurations (lightly damped case 1 and more heavily damped case 2), the following conclusions can be drawn:

- the absorption properties of this metacomposite are enhanced in both cases;
- the transmission of the power flow at the active interface can be controlled by manipulating the external circuit, i.e. modification of reflective properties versus added damping;
- the frequency band where the system is effective can be shifted by modifying specific values of the external circuit, i.e. 1000 – 3000 Hz (case 2) 3000 – 5000 Hz (case 1);
- it is possible to alter the elastic properties of the metacomposite (modal restructuring).

Therefore, this control technique could be used effectively in applications where the isolation of a source of disturbance is of paramount importance. This work shows that, under specific conditions, it is indeed possible on extended structures to isolate a disturbance response to a limited region of the overall structure, and to do so without significantly modifying the impedance perceived by the excitation source.

An implication of the results presented here on future research is that the reflective properties of the active interface could also be used in an energy harvesting context; a confinement of the kinetic energy at the position of an energy harvester would allow it to recover more energy in each cycle as compared to without such confinement.

Also with respect to future studies, it will be interesting to estimate the quantity of vibrational energy dissipated within the electric circuit and to characterize the control system from the perspective of wave propagation through measurement of wave dispersion and scattering.

Chapter 5

Investigations on the Finite-extent Plate with Periodic Shunts

5.1 Overview

In this section, a periodic 15 × 5 lay-out of negative capacitance circuit shunted piezoelectric transducer (PZT) patches is designed and applied to achieve broadband vibration reduction of a flexible plate over tunable frequency bands. Each surface-bonded PZT patch is connected to a single independent negative capacitance circuit. A finite element-based design methodology is used to predict the attenuation properties of the smart structure. The predictions are then experimentally validated by measuring the harmonic response of the plate and evaluating some derived quantity such as the loss factor and the kinetic energy ratio.

The validated model is also used to explore different configurations with the aim of defining some design criteria.

5.2 Numerical Model of the Smart Plate

5.2.1 Variational Formulation

Consider a flexible piezoelectric structure depicted in Figure 5.1 occupying the volume V_s and subjected to a prescribed displacement $\bar{u}$ on a part S_u and to surface force components f on the complementary part S_f of its external boundary. Let n be the unit normal external to V_s. The

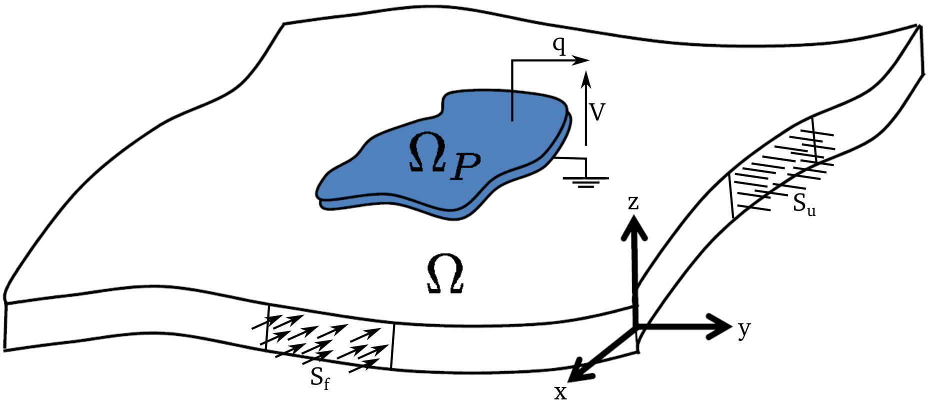

Figure 5.1: Plate with arbitrarily shaped piezoelectric patch bonded on the top surface and considered coordinate system.

electric boundary conditions are defined by a prescribed surface charge $\bar{q}$ on S_q and an electric potential $\bar{\phi}$ on the remaining part S_ϕ. The local equilibrium equations are given by

$$\begin{aligned} \rho\ddot{u} - \nabla \cdot \sigma &= f \\ \nabla \cdot D &= 0 \end{aligned} \tag{5.1}$$

along with the following boundary conditions:

$$\begin{aligned} &\sigma \cdot n = T && \text{on } S_f \\ &u = \bar{u} && \text{on } S_u \\ &D \cdot n = -\bar{q} && \text{on } S_q \\ &\phi = \bar{\phi} && \text{on } S_\phi \end{aligned} \tag{5.2}$$

where σ is the symmetric Cauchy stress tensor, D denotes the electric displacement vector components and ρ is the mass density of the structure.

The stress tensor and electric displacement are related to the linear strain tensor ε and electric field E through the constitutive laws for a piezoelectric materials [77]:

$$\begin{aligned} \sigma &= C_E\varepsilon - e^T E \\ D &= e\varepsilon + \epsilon_S E \end{aligned} \tag{5.3}$$

where C_E, e, ϵ_S denote the mechanical stiffness matrix evaluated at constant electric field, the piezoelectric stress coupling matrix and the permittivity matrix at constant strain, respectively. Finally, the strain tensor is calculated as follows:

$$\varepsilon = \nabla_s u = \frac{1}{2}\left(\nabla u + \nabla^T u\right). \tag{5.4}$$

The electric field and the voltage are related through the simple formula

$$E = -\nabla\phi. \tag{5.5}$$

For arbitrary admissible virtual displacements δu and electric potential $\delta\phi$, the equilibrium equations in (5.1) are equivalent to

$$\int_{V_s} \delta u\left(\rho\ddot{u} - \nabla\cdot\sigma - f\right) dV = 0 \tag{5.6}$$

and

$$\int_{V_s} \delta\phi\left(\nabla\cdot D\right) dV = 0. \tag{5.7}$$

Using the divergence theorem along with the piezoelectric constitutive relations, and taking into account the gradient relations and natural boundary conditions yields

$$\int_{V_s} \delta\varepsilon\left(C_E\varepsilon + e\nabla\phi\right) + \int_{V_s} \delta u\left(\rho\ddot{u}\right) - \int_{V_s} \delta u\left(f\right) dS = 0 \tag{5.8}$$

and

$$-\int_{V_s} \delta E\left(e\varepsilon - \epsilon_S\right) dS = 0 \tag{5.9}$$

Finally, equations (5.8) and (5.9) can be combined together yielding

$$\int_{V_s} \delta u\rho\ddot{u}dV + \int_{V_s} \delta\varepsilon C_E\varepsilon dV - \int_{V_s} \delta\varepsilon eEdV - \int_{V_s} \delta Ee\varepsilon dV - \int_{V_s} \delta E\epsilon_S EdV = 0 \tag{5.10}$$

where $u = [u_x, u_y, u_z]^T$ is the displacement vector, $E = [E_x, E_y, E_z]^T$ is the electric field vector and $\varepsilon = [\varepsilon_{xx}, \varepsilon_{yy}, \varepsilon_{zz}, \varepsilon_{xy}, \varepsilon_{xz}, \varepsilon_{yz}]^T$ is the strain vector.

5.2.2 Finite Element Formulation

Within a finite element framework, the field variables u and ϕ are related to nodal degrees of freedom d and V through a proper selection of shape functions N_u and N_V:

$$u = N_u d \quad \phi = N_V V. \tag{5.11}$$

Substituting equation (5.11) into equation (5.10) and assuming an harmonic motion

$$\begin{aligned} d &= \hat{d}e^{j\omega t} V = \hat{V}e^{j\omega t} \\ f &= \hat{f}e^{j\omega t} q = \hat{q}e^{j\omega t} \end{aligned} \tag{5.12}$$

yields the following electro-elastic system of equations:

$$\begin{aligned} K_{uu}\hat{d} + K_{uV}\hat{V} - \omega^2 M_{uu}\hat{d} &= \hat{f} \\ K_{Vu}\hat{d} + K_{VV}\hat{V} &= \hat{q} \end{aligned} \tag{5.13}$$

where

$$\begin{aligned} M_{uu} &= \int_{V_s} N_u^T \rho N_u dV \quad & K_{uu} &= \int_{V_s} B_u^T C_E B_u dV \\ K_{uV} &= \int_{V_s} B_u^T \rho B_V dV \quad & K_{VV} &= \int_{V_s} B_V^T \epsilon B_V dV \\ f &= \int_{S_s} N_u^T f dV & q &= -\int_{S_q} N_V^T q dV \end{aligned} \tag{5.14}$$

and $B_u = \mathcal{S}N_u$ and $B_V = \nabla N_V$ where $\mathcal{S}$ is the linear differential operator matrix which relates the strains to the structural displacements.

5.2.3 Application to Thin Plates with Piezoelectric Patches

The combination of the host structure and the piezoelectric patches is modeled using 4-node Kirchhoff plate elements [50]. According to Kirchhoff kinematic assumptions, the strain-displacement relations for the plate are written as

$$u_x = -z\frac{\partial w}{\partial x} \quad u_y = -z\frac{\partial w}{\partial y} \quad u_z = w \tag{5.15}$$

where w is the transverse displacement of the plate mid-surface and z is the distance form the mid-surface. The strain operator $\mathcal{S}$ reduces to

$$\mathcal{S} = [\partial^2/\partial x^2, \partial^2/\partial y^2, 2\partial^2/\partial x\partial y]^T. \tag{5.16}$$

The electric field is assumed to be constant on the surface of each piezoelectric patch and the electric potential is assumed to vary linearly through the thickness from zero at the bottom surface to ϕ_{p0} at the top electrode:

$$V_0 = \frac{z - h/2}{h_p} V_{p0} \tag{5.17}$$

where h and h_p are the plate and piezoelectric thickness.

Under these assumptions, the electrical equation becomes a scalar equation of the form

$$K_{\phi u}\hat{d} + K_{VV}\hat{V}_p = \hat{q}. \tag{5.18}$$

Application of the shunting circuit to the electrodes of the piezoelectric patch allows condensing out equations (5.13) to obtain

$$\left(K_{uu} - \omega^2 M_{uu} + S_{uu}\right)\hat{d} = \hat{f} \tag{5.19}$$

where S_{uu} is the shunting matrix describing the effect of the shunting circuits on the dynamic behavior of the structure. It is given by

$$S_{uu} = j\omega K_{uV}\left(j\omega K_{VV} - K_Z\right)^{-1} K_{Vu} \tag{5.20}$$

where K_Z is the matrix containing the terms related to the impedance Z of the shunting circuit. The impedance operator can displays different components normally shunted in series to the piezoelectric ceramic.

Different circuit's layout can be considered:

- resistive circuit: $Z = R$

	f_1	f_2	f_3	f_4	f_5	f_6	f_7	f_8	f_9	f_{10}
plate	3.58	4.43	9.94	9.76	14.68	17.35	16.93	19.81	24.05	26.73
OC	3.65	4.69	9.62	9.97	14.79	17.34	17.59	19.78	23.91	26.75
SC	3.64	4.69	9.60	9.97	14.72	17.33	17.59	19.73	23.79	26.67

Table 5.1: Plate's natural frequencies: bare plate, plate with the piezoelectric ceramics (Open Circuit/Short Circuit).

- inductive circuit: $Z = R + j\omega L$
- capacitive circuit: $Z = R + \dfrac{1}{j\omega C}$

It is clear that the shunting matrix can affect the inertial, the damping or the stiffness properties of the structure depending on the characteristic of the piezoelectric patch and the shunting circuit parameters.

5.3 Frequencies and Mode Shapes of the Smart Plate

In order to characterize the dynamic behavior of of the smart plate a preliminary eigenvalues analysis has been performed. The obtained natural frequencies have been compared with the natural frequencies identified during the experimental measurements. During the experiment the plate were excited at the bottom corner by a shaker generating a white noise signal in the $0-500$ Hz, the out-of-plane velocity component was measured with a frequency resolution of 0.25 Hz. The experimental procedure was affected by different problems that slightly perturbed the final results. For example was not possible to guarantee the ideal conditions of free boundaries since the plate was attached to the ceiling through thick metallic wires. Moreover the frequency response function measurement was performed keeping the piezoelectric ceramics connected to the electric circuits in position off. The calculated response were obtained considering two different conditions, namely an open circuit and a short circuit. In table 5.1 the first ten system's natural frequencies for the open circuit and short circuit configuration are collected along with the natural frequencies of the bare plate. The introduction of the piezoelectric ceramics tends to increase the stiffness of the plate without modifying the inherent mode-shape. In Figure 5.2 are presented the associated mode-shapes for the three considered conditions.

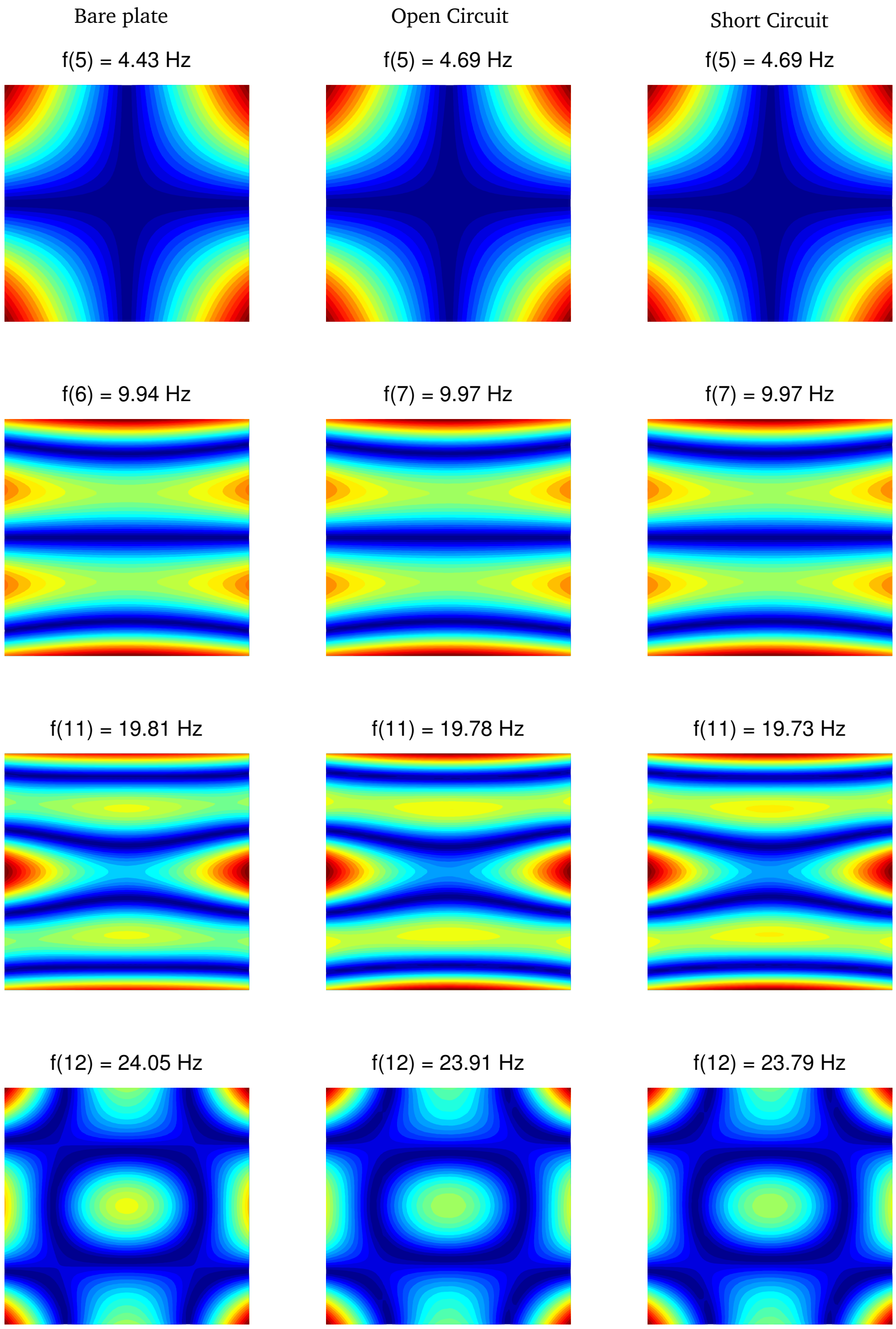

Figure 5.2: Natural frequencies and mode shapes of the smart plate: bare plate (left column), plate + active interface + Open Circuit (center column) and plate + active interface + Short Circuit (right column).

5.4 Some Energy Relation for Piezo-Mechanical Systems

To better understand the underlying physics of this control system a conservation laws involving time varying quantity such as velocities and forces has been set up [15].

Equation (5.19) represents a linear n-DOF mechanical system vibrating harmonically under the action of an external force. The main goal of this section is to recall some equation relating various energy characteristics such as the power flow, the kinetic energy and others.

The following developpement is based on the representation of linear quantity by a sum of two independent time alternating components and a quadratic quantity represented by three independent components.

In vibration mechanics the following quantities are usually considered:

- power flow $P = v^T F$;
- kinetic energy $T = \frac{1}{2} v^T M v$;
- potential energy $U = \frac{1}{2} u^T K u$;
- total energy $E = T + U$;
- Lagrangian function $L = T - U$;
- loss power $\Phi = \frac{1}{2} v^T C v$.

Each of these quantities can be represented as the sum of three components, as an example let us consider the power flow

$$P = P_0 + F_c \cos 2\omega t + F_s \sin 2\omega t. \tag{5.21}$$

The three components in equation (5.21) are independent in the sense that they are orthogonal in the time interval $2\pi/\omega$.

The terms P_0, F_c and F_s can be easily estimated using the complex numbers formalism, for example the alternating components of P in the frequency domain is simply the product of the complex amplitude of the velocity and the force

$$P = v^T F = P_c + j P_s. \tag{5.22}$$

likewise the continuous components are calculated as the product of the force and the conjugate of the velocity

$$P^* = v^{*T} F = P_0 + jP_q. \tag{5.23}$$

The term P_q do not relate to any significant physical quantity but rather represents the part of the velocity vector in quadrature with the external force.

Other quadratic quantities are represented in a similar manner. However, unlike the power flow, they all have zero reacting component. For example we can consider the kinetic energy

$$\begin{aligned} T &= \frac{1}{4} v^T M v = T_c + jT_s \\ T^* &= \frac{1}{4} v^{*T} M v = T_0 \end{aligned} \tag{5.24}$$

or the potential energy

$$\begin{aligned} U &= \frac{1}{4} u^T K u = U_c + jU_s \\ U^* &= \frac{1}{4} u^{*T} K u = U_0. \end{aligned} \tag{5.25}$$

All these quantities are linked to each others via the equation of conservation of energy

$$P = j\omega E + \Phi. \tag{5.26}$$

By comparison the following relations are established both for the:

- alternating components

$$\begin{aligned} P_c &= \Phi_c - 2\omega E_s \\ P_s &= \Phi_s + 2\omega E_c \end{aligned} \tag{5.27}$$

- continuous components

$$\begin{aligned} P_0 &= \Phi_0 \\ P_q &= -2\omega L_0. \end{aligned} \tag{5.28}$$

In particular, two relations will be further analyzed: the first one relate the time averaged power flow P_0 to the total averaged amount of dissipated energy Φ_0. the second one relates the reactive power flow P_q to the time-averaged Lagrangian function L_0.

The active power flow balance is presented in Figure 5.3. In the left column is easy to observe a

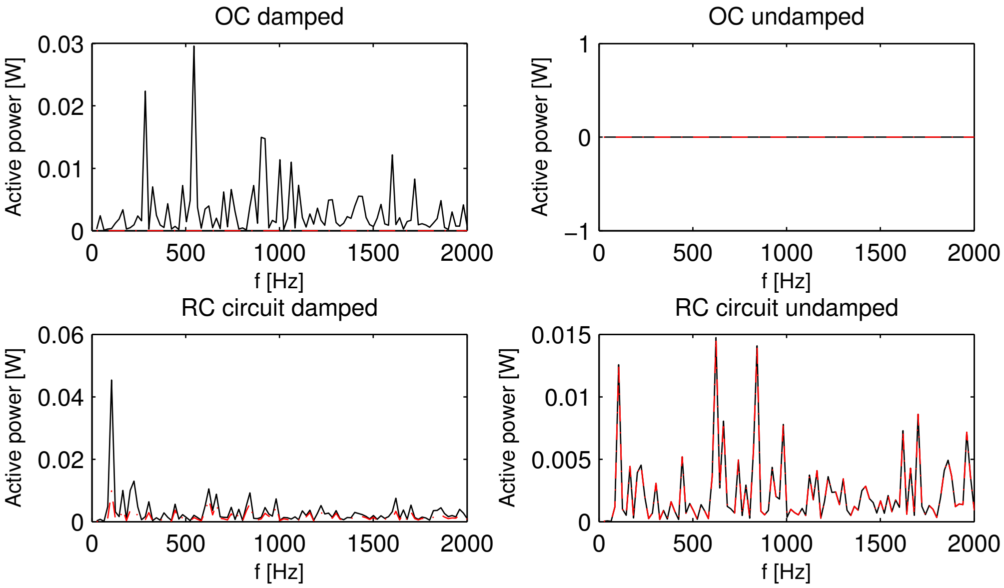

Figure 5.3: System's active energy balance for two different circuit configuration: open circuit and negative capacitance circuit. On the left the total amount of dissipated energy is due to the internal and circuit losses, on the right the internal losses have been neglected.

mismatching between the curve representing the the active power flow P_0 and the total amount of dissipated energy Φ. In this case the damping due to the losses in the plate is not neglected. An hysteretic damping is considered in order to reproduce the losses occurring within the plate. It is not possible to isolate the dissipative contribution present in the the stiffness matrix. The relations (5.27) and (5.28) only hold if the matrices M K are real. Therefore the calculation of these terms must be carried out following a different approach. Another source of dissipation is produced by the external circuit, this term can be calculated using the following relations:

$$\begin{aligned} V &= \left(K_Z - K_{VV}\right)^{-1} K_{Vu} u \\ i &= K_Z^{-1} V \end{aligned} \tag{5.29}$$

By knowing the voltage V and the current i for each circuit the calculation of the power consumed is straightforward

$$P_{el}^{*} = \frac{1}{2} V i^{*} \tag{5.30}$$

the real part of P_{el}^{*} corresponds to the energy dissipated within the circuit. In order to verify this statement we can neglect the dissipative term representing the internal losses of the plate.

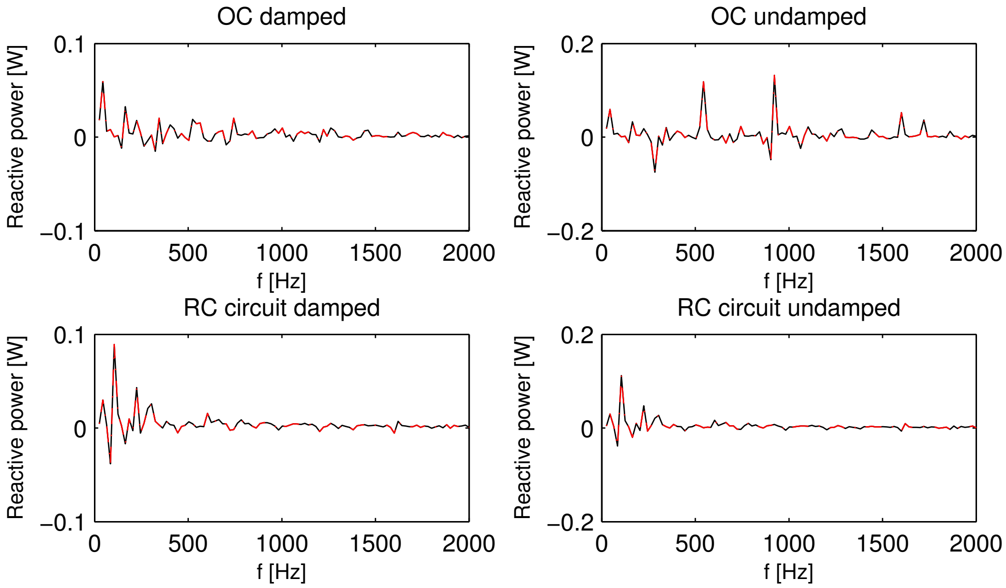

Figure 5.4: System's reactive energy balance for two different circuit configuration: open circuit and negative capacitance circuit. On the left the balance take into account the internal and circuit losses, on the right the internal losses have been neglected.

Under these assumption the matching between the aforementioned quantities is obtained over the whole frequency range as clearly depicted in Figure 5.3.

At each cycle the average energy dissipated by the excitation source exactly balance the total amount of energy consumed by the smart plate:

$$P_0 = \Phi_0^s + P_{el0}. \tag{5.31}$$

The balance of the reactive power flow turn to be very useful in the case someone need to exactly calculate the kinetic energy T_0 and the potential energy U_0.

In figure 5.4 the reactive power flow balance is presented assuming, in left column, the presence of internal and electrical damping and in the right column by just considering the damping due to the circuit for the open and shunted circuit (negative capacitance). The figure clearly shows that all the term in the equation have been correctly taken into account.

This approach allows us to validate the proposed approach providing some reliable tools for the energetic analysis of the smart system. Furthermore the calculation the active power flow P_0

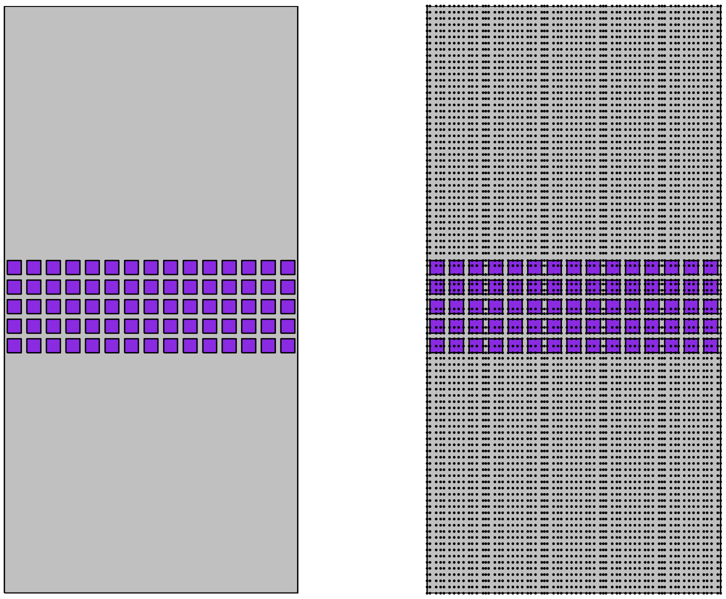

Figure 5.5: Geometry and mesh of the plate with 15 × 5 array of piezoelectric ceramic actuators.

and the total energy E_0 allows one to estimate the loss factor of the system

$$\eta = \frac{P_0}{\omega E_0}. \tag{5.32}$$

5.5 Harmonic Response of the Smart Plate

The host structure is a rectangular plate with geometrical and mechanical properties summarized in table 3.1. The plate dimensions are chosen in order to exactly reproduce the experimental rig described in Chapter 4. A periodic lay-out of 15 × 5 piezoelectric patches is placed on the top surface of the plate 850 mm away from the lower side.

The plate is excited by a point force located in the lower left corner of the plate, the response is evaluated in terms of out-of-plane displacement and its derived quantities such as the loss factor and the kinetic energy ratio. Figure 5.5 illustrates the FE mesh adopted for the analysis along with the considered boundary conditions. The FE mesh features 46 × 70 rectangular plate elements.

	f_1	f_2	f_3	f_4	f_5	f_6	f_7	f_8	f_9
Ref	3.65	4.69	9.62	9.97	14.79	17.34	17.59	19.78	23.91
Exp	-	4.62	-	9.81	-	-	-	19.90	23.40
Err %	-	1.50	-	-1.90	-	-	-	-0.60	2.13

Table 5.2: Comparison of the experimental and numerical plate's natural frequencies.

The present model has been validated by comparing the calculated and the measured natural frequencies. Table 5.2 summarizes the set of natural frequencies used for the comparison and shows that the relative error in less than 5% for all the values.

In figure 5.6 the calculated and the measured loss factors are compared for three different conditions. In figure the lines are associated to the experimental measurements while the bars are associated to the calculated solutions. The blue items represent the baseline solution, by comparison it is clear that the calculated solution underestimate the total amount of dissipated energy. For example is not easy to include in the considered model the dissipation mechanism associated to the friction of the electric wires with the plate's surface. Another neglected source of dissipation is the external electric circuit, in the theoretical model each circuit is assumed to be open but this is not the case since each circuit is still connected to the external circuit in absence of power. Under these conditions the circuit is not able to reproduce the negative capacitance effect but is reasonable to assume that each circuit can still add an extra amount of damping due to the current flowing within the circuit.

According to this interpretation the results calculated with a capacitance of $53nF$ and a resistance of $R = 40\ \Omega$ (green line) $R = 400\ \Omega$ (red line) appear more reliable. In fact the trend of the loss factor is correctly captured over the whole frequency band although underestimate.

In figure 5.7 the calculated and measured kinetic energy ratio is compared in three different conditions: open circuit OC, negative capacitance control strategy with $R = 40\ \Omega$ and $R = 400\ \Omega$. The results are collected in three different diagrams representing respectively the ratio of kinetic energy confined in the upper portion of the plate, within the plate and in the lower portion of the plate. If we consider the part of the plate under the smart interface larger values of the kinetic energy ratio are associated to an increase of kinetic energy in the considered area. Under these conditions the vibrating field is modified, the smart interface is capable to confines the kinetic energy in a specific portion of the plate. The active interface act like an electro-mechanical filter

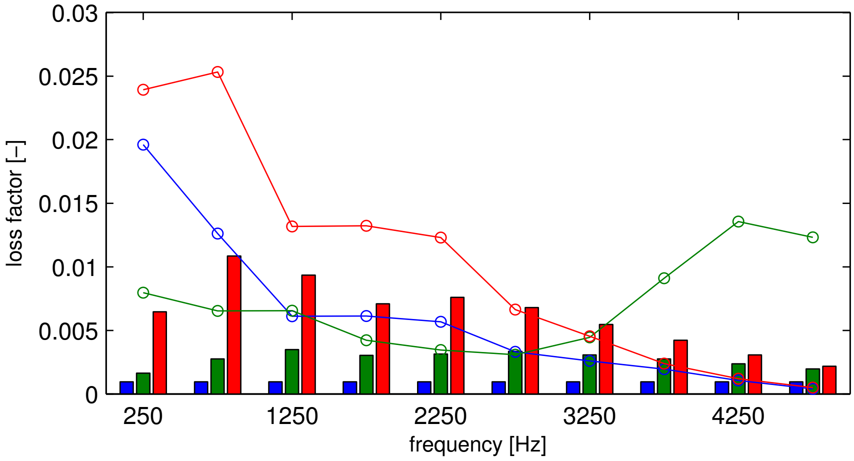

Figure 5.6: Loss factor of the 15x5 smart plate, in this figure the the lines represent the experimental data and the bars the calculated solutions. The color code indicates: the uncontrolled plate (blue), controlled plate with $R = 40\ \Omega$ (green) and $R = 400\ \Omega$ (red).

that prevent the occurrence of standing-waves characterized by certain wavelengths. Considering the figure at the top similar conclusions can be drawn, in this case, however, smaller values of the kinetic energy ratio correspond to the energy confinement effect. The obtained result are in good agreement with the experimental measurements even if the theoretical results constantly overestimate the confined energy. For higher frequencies the measurements and the calculated response seem to diverge but this is partly due to the problem experienced during the acquisition of the experimental data. For instance the coherence function varies as a function of the frequency and the position of the laser beam (plate's surface larger than 2 m^2).

The relevance of the mathematical model is finally proved comparing the velocity field of the controlled plate presented in Figure 5.8 for different excitation frequencies. At 25 Hz the response associated to the open circuit configuration is correctly captured by the mathematical model, the ODS are almost identical. The same trend is observed considering a negative capacitance circuit with a resistance of $R = 400\ \Omega$. However, with the negative capacitance circuit set with a resistance of $R = 40\ \Omega$ the results are less satisfactory since it is not possible to reproduce the same ODS. At 1680 Hz the measured and the theoretical responses are again comparable in all cases, here the comparison becomes more difficult since the spatial resolution is not sufficient to correctly describe the actual vibrating field, despite this limitation the similar repartition of the energy within the plate provide evidence about the quality of the mathematical model.

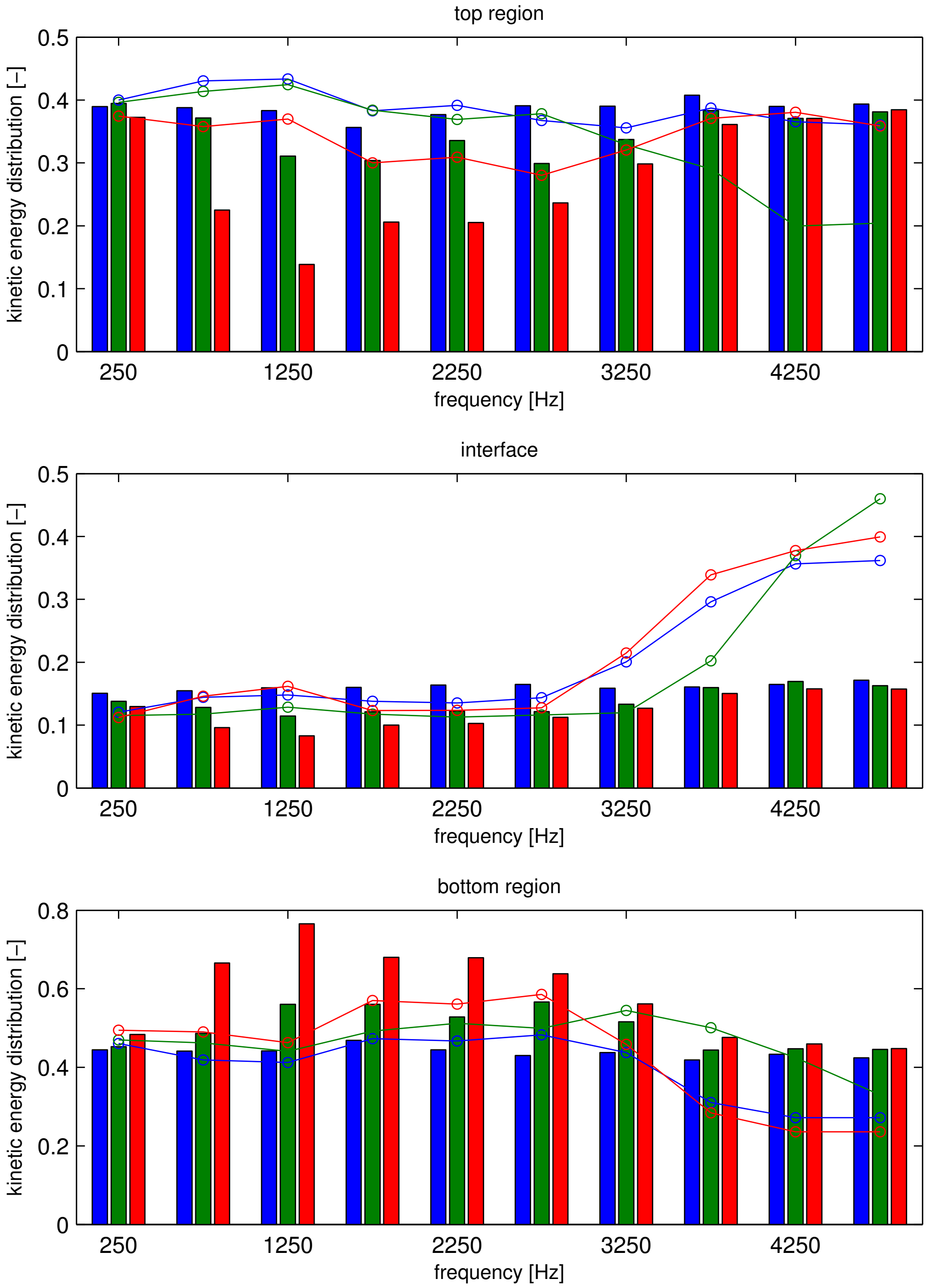

Figure 5.7: Kinetic energy distribution of the 15x5 smart plate, in this figure the the lines represent the experimental data and the bars the calculated solutions. The color code indicates: the uncontrolled plate (blue), controlled plate with $R = 40\ \Omega$ (green) and $R = 400\ \Omega$ (red).

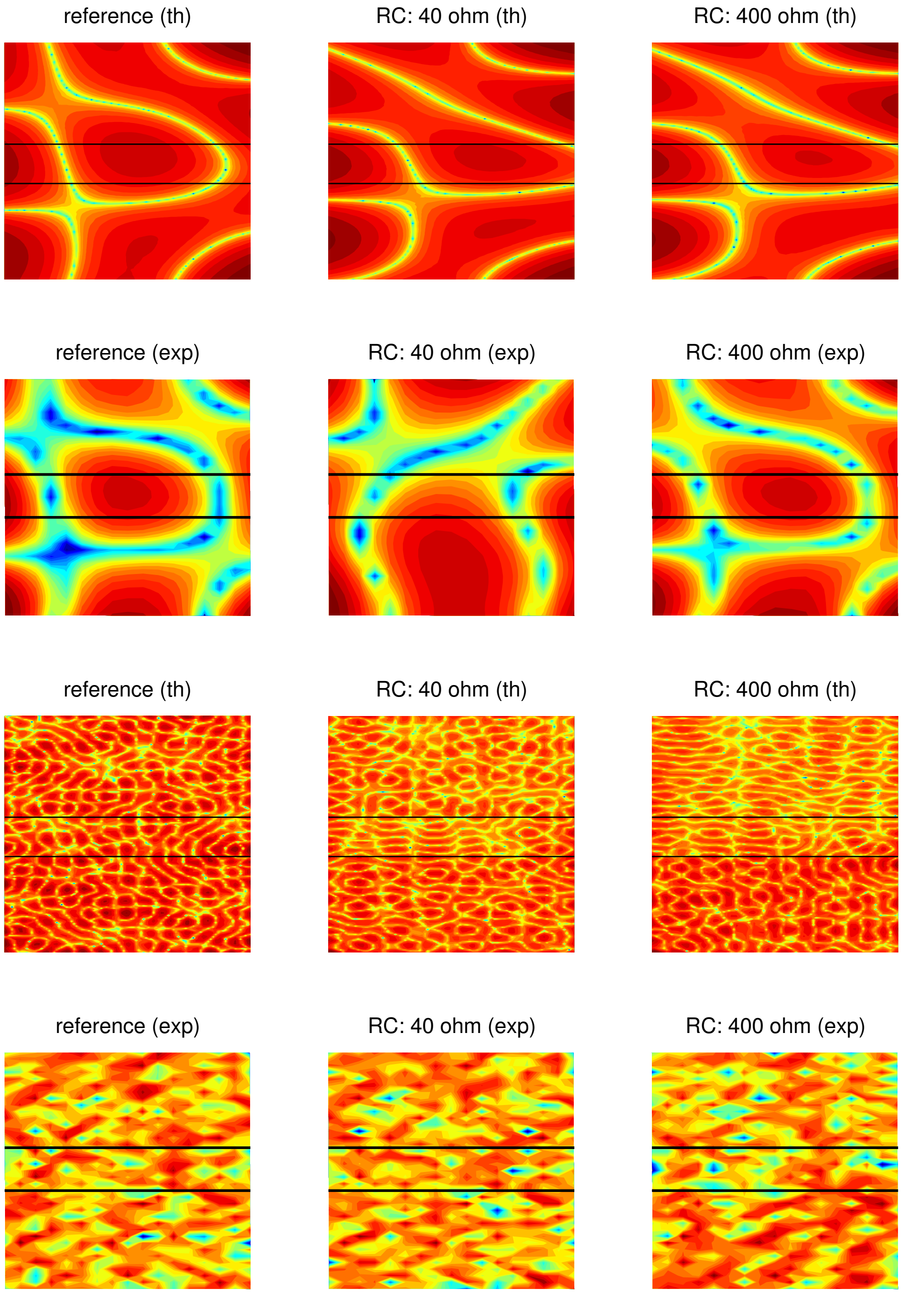

Figure 5.8: Two dimensional velocity field comparison (theoretical vs experimental data) of the 15x5 smart plate: uncontrolled plate (left), controlled plate with $R = 40\ \Omega$ (center) and $R = 400\ \Omega$ (right). Two excitation frequency have been considered: 25 Hz (top) and 1680 Hz (bottom).

5.6 The Effect of Negative Capacitance

In order to better match the experimental results, the influence of the different circuit's parameter on the overall system's performances have been investigated. To do so a parametric analysis has been performed considering the variation of the negative capacitance.

The performance of the control system has been analyzed considering two quantities: the loss factor and the kinetic energy ratio.

The first quantity gives a good estimation of the energy dissipated by the control system, therefore it qualifies the vibration attenuation capability of the control system.

In Figure 5.9 the loss factor of the controlled structure is opposed to the reference solution OC for three different values of negative capacitance. The green bar representing the best performances is associated to a negative capacitance very close to the estimated intrinsic capacitance C_p (it is related to the electromechanical properties of the piezoelectric ceramic) in this case is assumed to be 50 nF. The red and cyan bar represent a negative capacitance of 55.7 and 63 nF respectively. As expected the performance of the system degrade as one move away from the point of maximum effectiveness very close to C_p. An interesting feature is the fact that bigger attenuation is obtained for $C_{neg} = 51.3$ nF over a narrower frequency band, namely $0 - 1000$ Hz whereas for a bigger value of negative capacitance the overall performances are slightly reduced but broadened up to 5000 Hz. The filtering properties of the smart interface are enhanced introducing a negative capacitance control system. In particular with negative capacitance values closed to C_p the system is able to increase this indicator up to 0.8 in the 1000 Hz frequency band (Figure 5.10). The blue bar corresponding to $C_{neg} = 51.3$ nF shows better performance even though limited to a narrower frequency band. The red bar representing the biggest considered value of negative capacitance still shows acceptable performances, this fact can be used as evidence about the robustness of the proposed system.

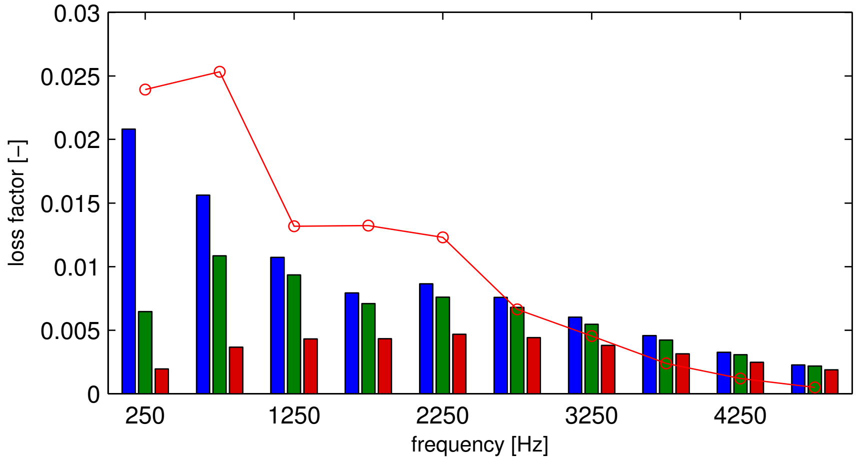

Figure 5.9: Loss factor of the 15x5 smart plate, in this figure the red line represent the experimental measurement of the controlled system with $R = 400\ \Omega$ and the bars the calculated solutions for different values of negative capacitance. The color code indicates: the controlled plate $C_{neg} = 51.3\ nF$ (blue), the controlled plate $C_{neg} = 55.7\ nF$ (green) and the controlled plate $C_{neg} = 63\ nF$ (red) in all cases a resistance of $R = 400\ \Omega$ has been chosen.

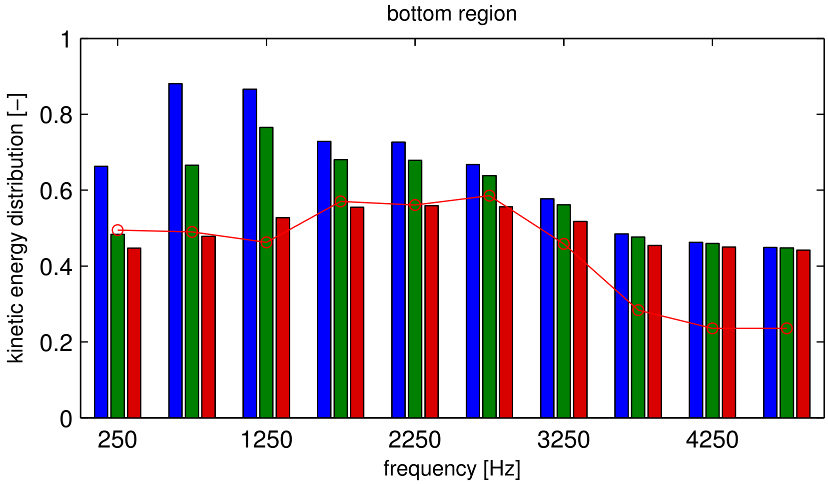

Figure 5.10: Kinetic energy distribution of the 15x5 smart plate, in this figure the red line represent the experimental measurement of the controlled system with $R = 400\ \Omega$ and the bars the calculated solutions for different values of negative capacitance. The color code indicates: the controlled plate $C_{neg} = 51.3\ nF$ (blue), the controlled plate $C_{neg} = 55.7\ nF$ (green) and the controlled plate $C_{neg} = 63\ nF$ (red) in all cases a resistance of $R = 400\ \Omega$ has been chosen.

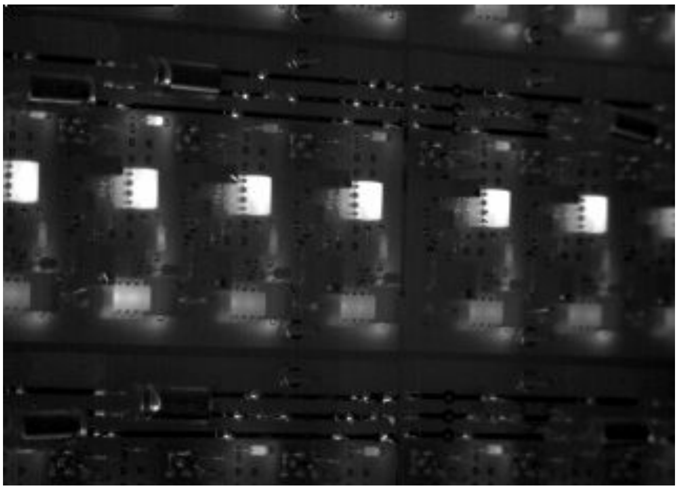

Figure 5.11: Infrared imagery of the control circuit during the operating phase. Lighter colors correspond to areas of high temperature.

5.7 The Effect of R

In the previous section we compared the theoretical and the experimental loss factor for different circuit parameters. The theoretical results were partially in agreement with the measurements, in particular the theoretical solution was always smaller than the measured response.

A possible explanation lies in the model used to describe the electric circuit. The real life circuit contains several passive components such as resistance and capacitance but also an operational amplifier intended for the creation of the suitable feedback signal whereas the theoretical circuit reproduces the desired function by means of a resistance and a negative capacitance. Moreover the presence of the instability detector circuit slightly modifies the main circuit adding an extra damping.

An experimental evidence that supports this thesis is presented in Figure 5.11 where an infrared picture shows which component is heated in response of the passage of the current during the control phase. As expected a large increase in temperature is observed for the operational amplifier, but also some secondary components such as the resistance belonging to the instability detector and the comparator increase their temperature. Unfortunately was not possible to estimate the energy radiated by the resistance R because of the external case of the potentiometer. The extra amount of damping has been taken into account by considering an external circuit having the following properties

$$Z = R. \tag{5.33}$$

Figure 5.12 shows the loss factor considering different circuit's configurations: open circuit, controlled system with a resistance of 40 and 400 Ω. Compared to the reference solution the addition of a resistance causes an increase in the loss factor proportional to its nominal value even in absence of the negative capacitance. For example introducing a resistance of 400 Ω (red bars) the loss factor is increased from 0.001 to 0.002. The difference between the two terms is associated to the losses due the the external electrical circuit, the residual part represented in blue reflects the losses present in the structure. However, by introducing the negative capacitance circuit the performances are further improved, rising from 0.002 to 0.01 in the 3000 Hz frequency band.

The addition of the resistance does not significantly change the kinetic energy ratio over the whole considered frequency range as clearly depicted in Figure 5.13.

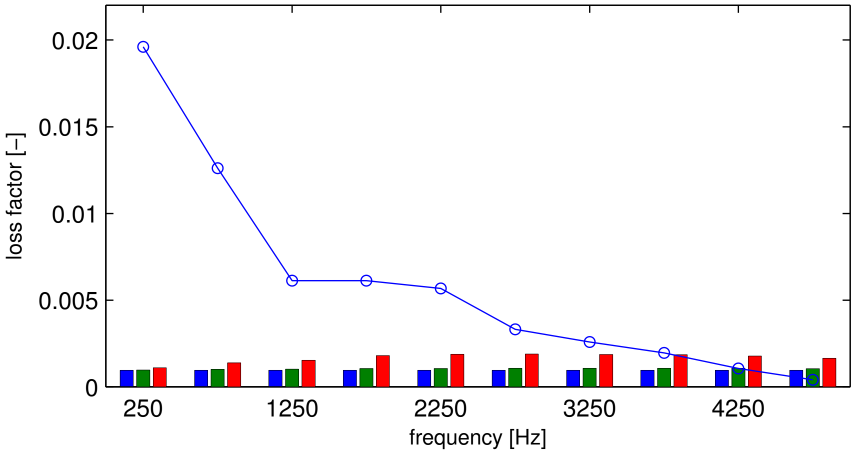

Figure 5.12: Loss factor of the 15x5 smart plate, in this figure the blue lines represent the measured response of the system with the circuit off and the bars the calculated solution. The color code indicates: uncontrolled plate (blue), controlled plate with pure resistive circuit $R = 40$ Ω (green) and $R = 400$ Ω (red).

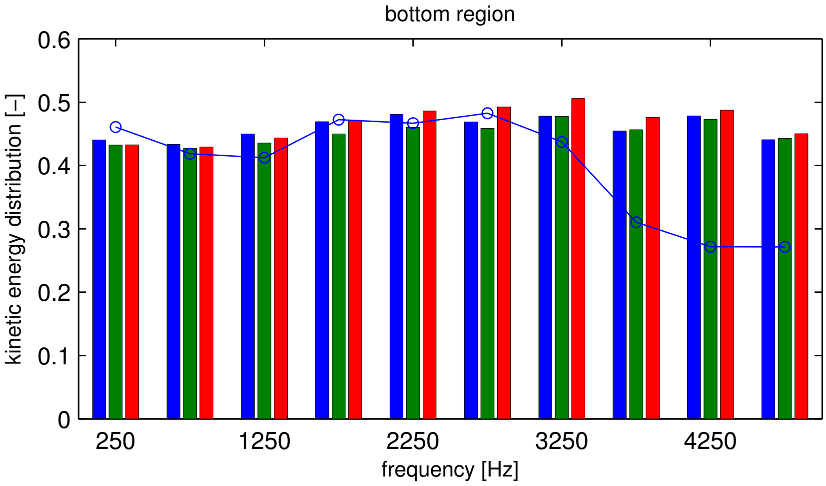

Figure 5.13: Kinetic energy distribution of the 15x5 smart plate, in this figure the blue lines represent the measured response of the system with the circuit off and the bars the calculated solution. The color code indicates: uncontrolled plate (blue), controlled plate with pure resistive circuit $R = 40$ Ω (green) and $R = 400$ Ω (red).

5.8 Real-life Circuit

In Section 5.5 the behavior of external circuits is approximated by an ideal impedance

$$Z = R + \frac{1}{j\omega C} \tag{5.34}$$

containing a resistance R and a capacitance C. The capacitance is tuned imposing values of C very close to the intrinsic capacitance of the piezoelectric ceramic C_p. As mentioned previously better performances are obtained when the capacitance C is tuned very closed to C_p. Unfortunately, this is not the only parameter that determine the relevancy of circuit model. In the real life circuit another effect occurs when the system approach to the intrinsic capacitance C_p, a self-excited vibrations take place because of the interaction of the two capacitance of opposite sign. Moreover the layout of the actual circuit used during the experiment include an operational amplifier employed as a gyrator. This specific circuit architecture originates a negative resistance at low frequencies that determine an energy increase detrimental for the system's stability.

In the frequency domain the real-life circuit assume the following form

$$Z_{re} = R - \frac{1}{\alpha\left(1/R_2 + j\omega C_2\right)} \tag{5.35}$$

for very low values of ω the active part of the impedance Z_{re} assume negative values since the ratio R_2/α is normally larger than R.

This effect is clearly observed in Figure 5.14 where the experimental loss factor in the 250 Hz frequency band assumes the value of 0.025, it increases up to almost 0.03 and then dramatically decreases increasing the excitation frequency. This trend is better observed for the real life circuit represented by the blue bars, in this case the loss factor is decreased at low frequencies in good agreement with the experimental data. At frequency values no differences between the two mathematical models are observed. This last evidence suggest that in most of the cases the former approach can be use without loss of reliability. We should pointing out that both approaches lack of some prediction capabilities due to the fact that is not easy to take into account each aspect of the actual circuit in particular the true behavior of the operational amplifier and the

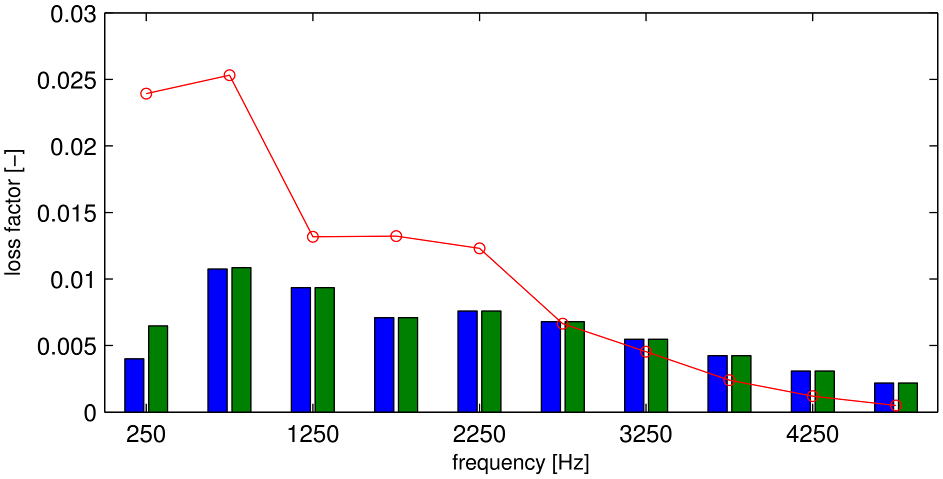

Figure 5.14: Loss factor of the 15x5 smart plate, in this figure the red line represent the experimental measurement of the controlled system with $R = 400\ \Omega$ and the bars the calculated solutions for different circuit layout. The color code indicates: the controlled plate with real-life circuit (blue) and the ideal circuit (green). The parameters of the real-life circuit have been chosen in order to reproduce the same set of parameters of the ideal one at higher frequency values.

contribution of the auxiliary circuit introduced in order to detect the occurring instability (LED circuit).

Regarding the kinetic energy distribution (Figure 5.15) the two models give the same results showing that the enhanced circuit model has an effect on the active part of the impedance leaving unchanged the reactive ones. It should be noted that the ideal and the real circuit model always overestimate the quantity of energy confined downward. The differences between the calculated and measured response can be justified considering the hypothesis made, for example in the mathematical model the the piezoelectric ceramic and the plate surfaces were considered perfectly attached, the presence of the glue was completely neglected. Moreover not all the external circuits are tuned at the same negative capacitance ratio and a certain dispersion in the material properties is observed. This aspect appears to be particularly interesting because in practice it is very difficult to ensure a perfect periodic assembly, for this reason this aspect will be further analyzed in the following section.

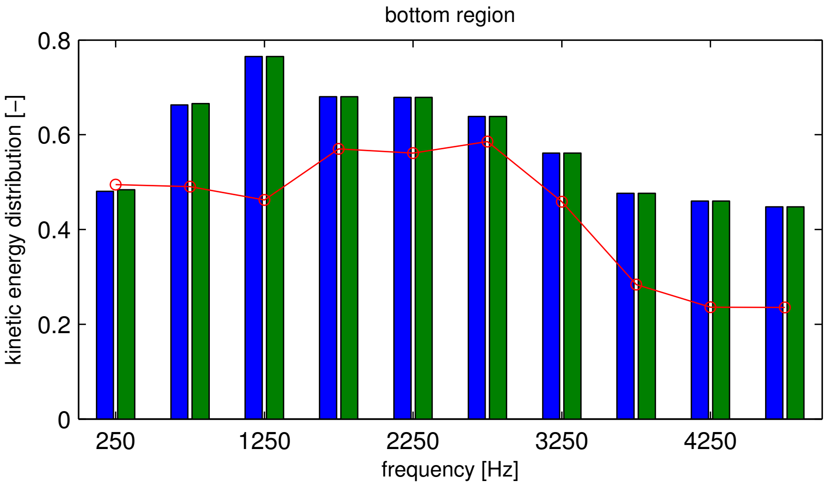

Figure 5.15: Kinetic energy distribution of the 15x5 smart plate, in this figure the red line represent the experimental measurement of the controlled system with $R = 400\ \Omega$ and the bars the calculated solutions for different circuit layout. The color code indicates: the controlled plate with real-life circuit (blue) and the ideal circuit (green). The parameters of the real-life circuit have been chosen in order to reproduce the same set of parameters of the ideal one at higher frequencies.

5.9 Some Issue on Robust Design

The finite element model considered so far rely on strong hypothesis not always respected in practice. For example is not possible to ensure the perfect bonding between the piezoelectric ceramic and the plate surfaces. Between these two surfaces is interposed a layer of glue of variable thickness that deteriorates the electromechanical coupling. Other sources of uncertainty are found in the dispersion of the mechanical properties of the actual piezoelectric ceramic. The same observation apply to the electrical components for which a nominal tolerance is provided by the manufacturers themselves.

With these premises is not possible to imagine a perfect periodic lattice of piezoelectric actuators but rather a network of co-localized actuator driven by an independent negative capacitance circuit.

These sources of uncertainty are taken into account introducing a random negative capacitance. This term varies according to an uniform distribution in a predetermined interval, we arbitrarily decided to set the interval between 51 and 53 nF.

In Figure 5.16 the loss factor is depicted assuming a resistance of $R = 40\ \Omega$ and $R = 400\ \Omega$

respectively. In both case a performance deterioration is observed, for example around 1000 Hz the loss factor associated to the electric circuit set at $R = 400\ \Omega$ (green bar) varies, respect to the ideal case with $C_{neg} = 51.3\ nF$ and $R = 400\ \Omega$, from 0.0011 to 0.0010.

The kinetic energy ratio associated to the lower part of the plate is not affected by the variation of the negative capacitance ratio for both configurations as clearly represented in Figure 5.17.

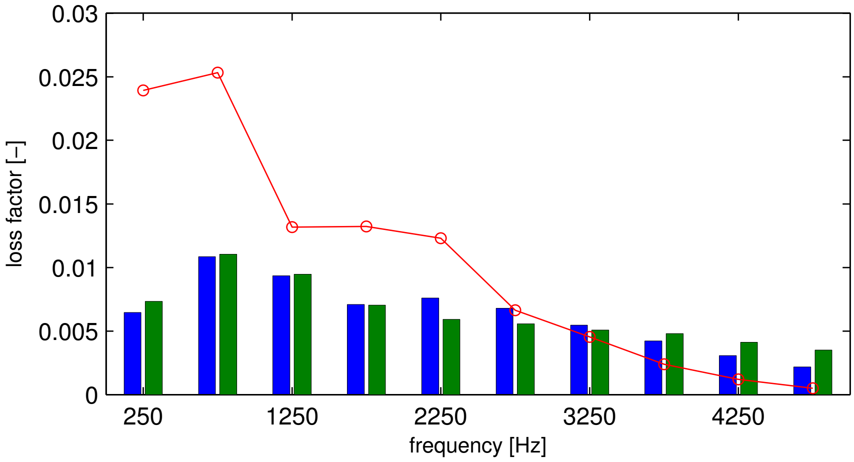

Figure 5.16: Loss factor of the 15x5 smart plate, in this figure the red lines represent the measured response of the controlled system $R = 400\ \Omega$ and the bars the calculated solution. The color code indicates: controlled plate with circuit with the same value of negative capacitance (blue) and controlled plate with circuit with the random value of negative capacitance (green). For both circuits $R = 400\ \Omega$ (red).

5.10 Topology of the Smart Interface

The section's main objective is to point out the relation between the topology of the smart interface and the overall performances of the control system. For instance the geometry of the piezoelectric actuators, the layout of the smart interface, among others, have a deep impact on the behavior of the control system. In particular these parameters have considerable influence on the frequency band where the system is more effective.

In order to better understand these mechanism a further analysis have been performed considering two different interface's layouts. In figure 5.18 the controlled plate is equipped with an 15×5 and 20×7 array of piezoelectric ceramics.

In figure 5.19 the structure's loss factor is compared for the two different interface layout.

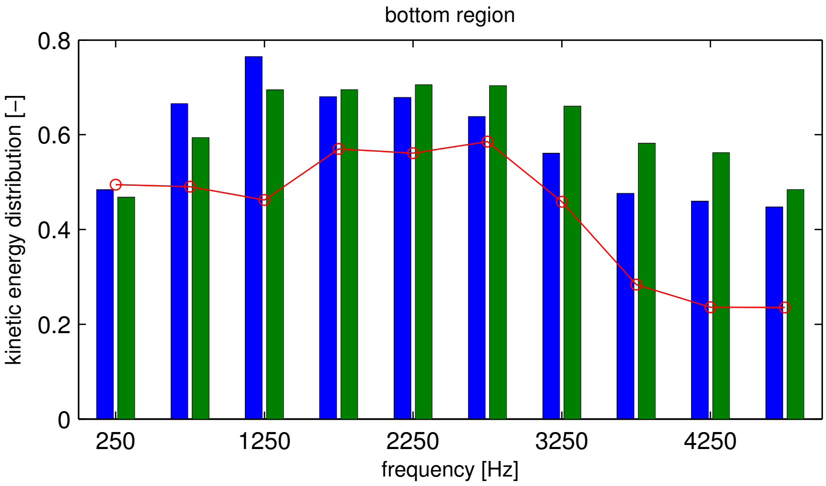

Figure 5.17: Kinetic energy distribution of the 15x5 smart plate, in this figure the red lines represent the measured response of the controlled system $R = 400\ \Omega$ and the bars the calculated solution. The color code indicates: controlled plate with circuit with the same value of negative capacitance (blue) and controlled plate with circuit with the random value of negative capacitance (green). For both circuits $R = 400\ \Omega$ (red).

The blue bar associated to the configuration 15×5 show higher loss factor values at very low frequencies, in the 250 Hz frequency band the averaged loss factor exceeds the value of 0.02 for higher values a deterioration in performance is observed in particular beyond 1000 Hz the 15×5 configuration appears less effective than configuration 20×7 (green bar). Configuration 20×7 provides good performances from 1000 to 10000 Hz. Moreover, respect to configuration 15×5 the value of the loss factor decrease less dramatically from one band to another, for instance a value of almost 0.01 is preserved over a frequency range of almost 5000 Hz. This behavior is justified by this simple observation: an array of several, relatively small, actuator is able to extract a comparable amount of energy from the occurring vibrating field composed by several standing waves having different wavelength. During the design of the smart interface is therefore fundamental to estimate this threshold values imposing certain restraints on the dimensions of the piezoelectric ceramic.

As a rule of thumb the length of the piezoelectric actuator should respect the following condition:

$$L < \frac{\lambda^*}{2} \tag{5.36}$$

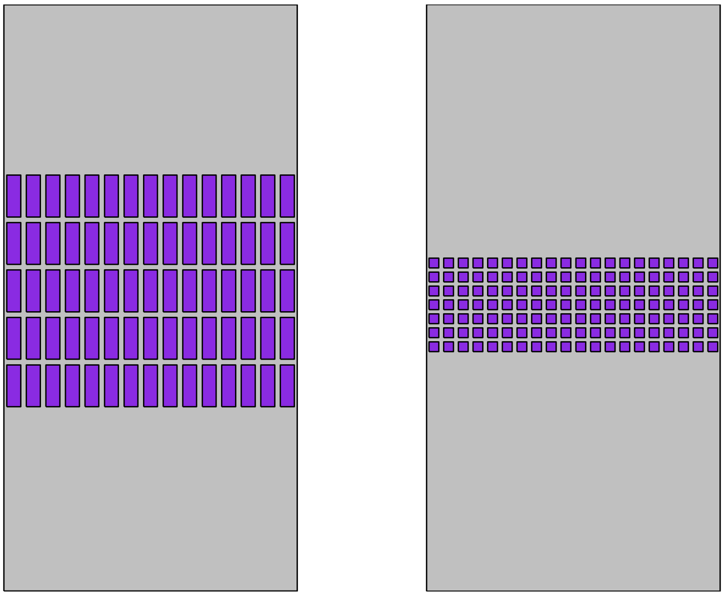

Figure 5.18: Finite element model' geometry for the two considered topologies: 15×5 array (left) and 20×7 array (right) of piezoelectric ceramic actuators.

where λ^* represent the wavelength of the targeted mode. For example examining the dispersion relation of the S_0 mode of the bare plate at 10000 Hz one obtains $\lambda^* = 120\ rad/m$, this means that the maximum length of the ceramic will be $L < 2.6\ cm$. This result is in good agreement with the calculated response. A 3 cm long ceramic is, in fact, not able to exert an appreciable control in this specific frequency band.

Similar considerations can be done about the averaged kinetic energy distribution within the plate. Configuration 15×5 represented by a blue bar in Figure 5.20 shows that the energy is evenly spread in the bottom part of the plate, there is not preferred frequency band, even if at very low frequencies the active interface seems to better filter the vibrating field increasing the ratio up to 0.6. Configuration 20×7 represented by green bars in Figure 5.20 behaves in a better way, in the $250 - 8250\ Hz$ the energy ratio is increased from 0.5 to 0.8.

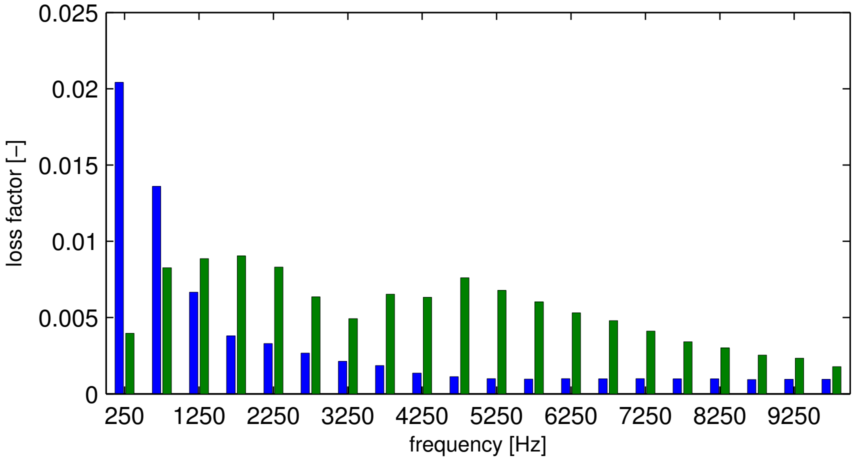

Figure 5.19: Loss factor of the smart plate. The blue line represent the 15 × 5 ideal negative capacitance configuration, the green line the 20 × 7 ideal negative capacitance configuration. For both cuircuits $R = 400\ \Omega$.

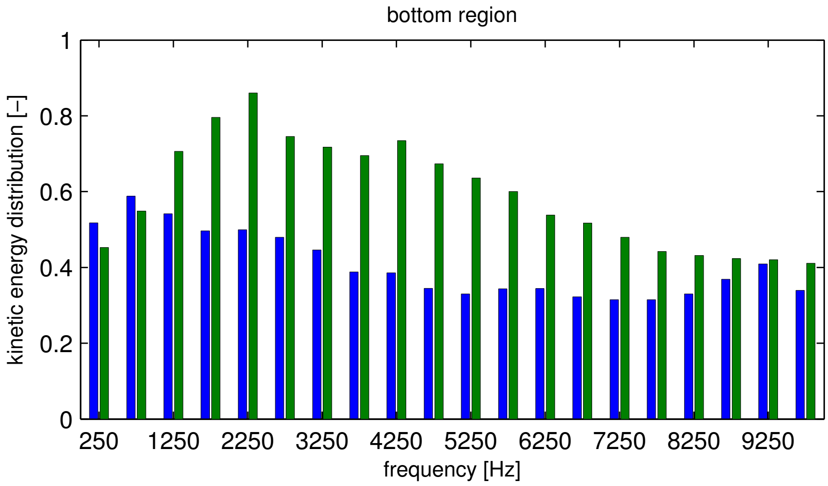

Figure 5.20: Kinetic energy distribution of the smart plate. The blue line represent the 15 × 5 ideal negative capacitance configuration, the green line the 20 × 7 ideal negative capacitance configuration. For both cuircuits $R = 400\ \Omega$.

5.11 RC-RL Performance Comparison

In this section two control strategy based on negative capacitance circuits and resonant circuits are compared. To do so a 15×5 array of piezoelectric patches is considered, for a sake of convenience the geometric properties of the smart interface are identical to the experimental layout described in Chapter 4.

For the resonant circuit two different tuning frequencies are arbitrarily selected at $f_{tun} = 1000$ and $f_{tun} = 3000$ Hz, the negative capacitance circuit is set imposing a negative capacitance value of 51.15 nF. For both layouts a resistance R of 400 Ω is selected.

The value of the inductance L is selected in order to tune the shunt circuit at the desired resonant frequency according to:

$$L = \frac{1}{\omega_{tun}^2 C_p} \tag{5.37}$$

where C_p is the inherent capacitance of the piezoelectric patch and $\omega_{tun} = 2\pi f_{tun}$ is the tuning angular frequency.

The loss factor show the presence of two attenuation frequency ranges centered at approximately 1000 and 3000 Hz. This behavior is attributed to the impedance mismatch in the mechanical properties of the assembly. These attenuation band can be shifted by simply varying the inductance of the electrical network without the need to modify the configuration of the structure, as explained in Chapter 1, the control capability will be always subject to the limitations associated to the geometry of the periodic assembly. Finally, it is interesting to observe how the value of the tuning frequency affects the shape of the attenuation bands. Figure 5.21 shows that higher frequency tuning values typically reduce the level of attenuation, but tend to broaden the range of effectiveness. Another evidence that show this fact is observed by analyzing the cyan bars associated to the tuning frequency of 1000 Hz. The averaged value of the loss factor suggest that the system in that band is less effective than the other configurations but this is not the case since the aforementioned quantity represent an averaged information, in a very narrow frequency band the circuit tuned at 1000 Hz provides very good performances if compared to the negative circuit configuration. On the other hand the negative capacitance circuit provide a good mitigation effect over a wider frequency band keeping larger values of loss factor. For instance an increase of 0.005 is observed from 250 Hz to 2250 Hz.

The wave filtering effect normally observed in control devices based on negative capacitance

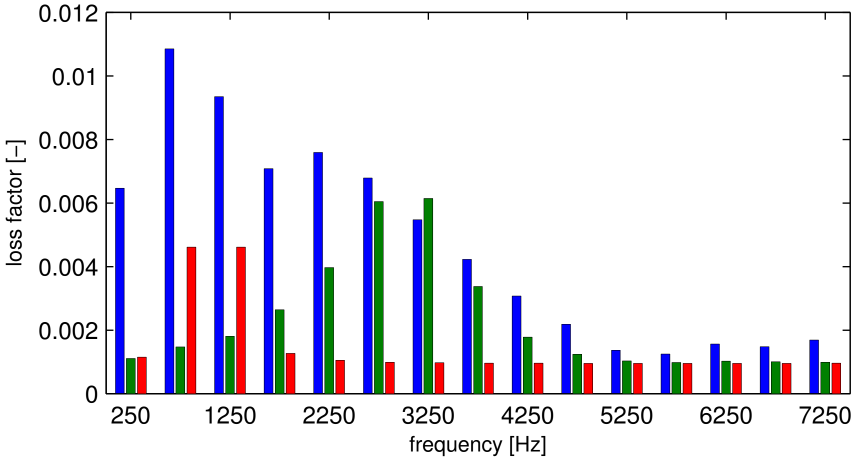

Figure 5.21: Loss factor of the 15 × 5 smart plate. The blue line represent the OC configuration, the green line the ideal negative capacitance configuration ($C_{neg} = 52$, $R = 400\Omega$), the cyan line the ideal RL configuration ($f_{tun} = 1000\ Hz$, $R = 400\ \Omega$) and the red line the ideal RL configuration ($f_{tun} = 3000\ Hz$, $R = 400\ \Omega$).

circuits is less evident in resonant circuit. In Figure 5.22 the kinetic energy distribution is compared the three considered cases. For the circuit tuned at 1000 Hz (cyan bars) the filtering effect appears slightly larger than the reference solution (open circuit) only in the vicinity of the tuning frequency an increase of the kinetic energy is observed. The same trend is also observed for the resonant circuit tuned at 3000 Hz. The best performances are provided by the negative capacitance circuit, in this case a larger amount of energy is confined in the the bottom region of the plate.

This arguments alone would be sufficient to show the effectiveness of the proposed control strategy but for a sake of comprehensiveness a local analysis has been performed in order to point out the global features of the response at certain excitation frequency. In Figure 5.23 the plate's velocity field is compared in the case of open, negative capacitance and resonant circuit for two different excitation frequency, namely 1000 and 3000 Hz. In the first case both the negative capacitance and the resonant circuit are able to reduce the system response and confine the kinetic energy in the bottom region of the plate. In the second case control system performances appear to be degraded.

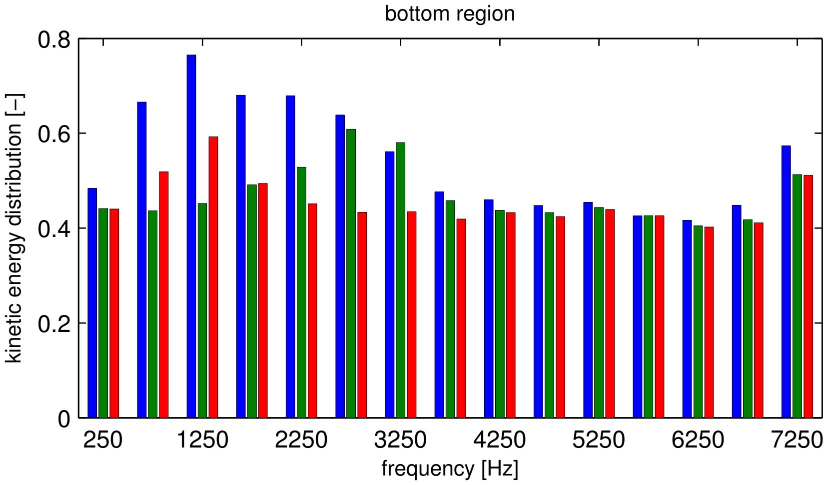

Figure 5.22: Kinetic energy distribution of the 15×5 smart plate. The blue line represent the OC configuration, the green line the ideal negative capacitance configuration ($C_{neg} = 52$, $R = 400\Omega$), the cyan line the ideal RL configuration ($f_{tun} = 1000\ Hz$, $R = 400\ \Omega$) and the red line the ideal RL configuration ($f_{tun} = 3000\ Hz$, $R = 400\ \Omega$).

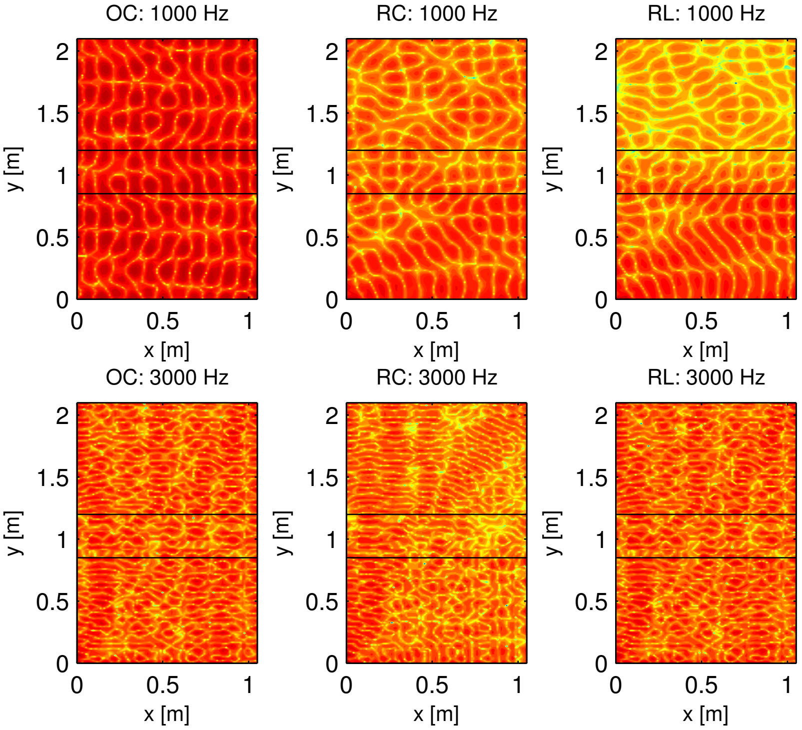

Figure 5.23: Two dimensional velocity field of the 15×5 smart plate. Left the OC configuration, center the ideal RC configuration ($C_{neg} = 52$, $R = 400\Omega$), right the ideal RL configuration ($f_{tun} = 1000\ Hz$, $R = 400\Omega$).

5.12 Conclusions

A periodic configuration of negative capacitance shunted piezoelectric patches is used to control vibrations of a freely suspended aluminum plate.

Numerical investigations demonstrated that the tuning capabilities of the negative capacitance networks can be effectively used to obtain a broadband control effect. The behavior of the smart plate is characterized by two different control mechanisms. The negative capacitance branch eliminates the parasitic effect due to the intrinsic capacitance of the piezoelectric ceramic enhancing the attenuation capabilities of the smart structure. The periodic lattice of piezoelectric actuator selectively filters the incident waves preventing the energy to pass through the smart interface.

The validated model also allows to draw some design criteria such as the choice of the electrical components, the size and the shape of the periodic lattice of piezoelectric patches. Some aspects of the robust design is also considered analyzing the effect of a randomly varying negative capacitance ratio on the overall performances of the system.

At the end of the chapter the negative capacitance control strategy is compared to the classical solution based on resonant circuits with the aim to show that the first solution offers numerous advantages such as the design simplicity and the effectiveness over a wider frequencies range.

Chapter 6

Conclusions

6.1 Summary

This research investigates the development of a new class of smart material called metacomposites. This appellation was chosen in order to emphasize two fundamental aspects that distinguish this strategy from other widespread solutions, namely:

- the use of a set of transducers periodically distributed over the surface of the controlled structure;
- the integration of the each transducer and the related control logic into the hosting structure.

From the theoretical point of view this two requirements are equivalent to impose specific conditions in correspondence of the boundaries (the active interface). If the interface is properly adjusted then the controlled structure can considerably modify its dynamic.

A rational design of such structure passes for the development of a mathematical model able to take into account the distributed and the multi-physic nature of the control system.

In this research a method based on the Bloch theorem has been proposed with the aim to describe the major feature of the smart metacomposite by just considering a representative portion of the interface. This procedures allowed us to identify two different operating conditions. Tuning the external circuit with a negative capacitance and a small resistance is possible to enhance the reflective properties of the structure, by increasing the value of the resistance is then possible to improve its absorbing properties.

These results were experimentally validated demonstrating the feasibility of proposed concept. Finally a multi-physic finite element model allowed us to analyze the complete structure under different conditions, in particular the layout of the array of piezoelectric transducer and the effect of each electric parameter on the overall performances have been investigated.

6.2 Contributions

The research presented in this work achieves the following contributions:

- a novel class of truly integrated smart active metamaterial called metacomposites;
- the design of the metacomposite's interface, characterized by excellent vibroacoustic performances over a wide frequency band;
- the experimental validation of the adaptive controlling interface concept;
- the metacomposite manufacturing, based on an array of piezoelectric ceramics periodically arragend over the top surface of a controlled structure and driven by a set of independent electronic circuits synthesizing a negative impedance;
- the experimental validation of the smart metacomposite in both reflecting and absorbing configuration.

6.3 Limitations & Challenges

The experimental tests performed on the actual structure confirm the theoretical hypotheses although the indicators chosen is not always the most appropriate, for example the loss factor calculated over the entire structure do not provide a satisfactory description of the absorbing capabilities of the control system at low frequencies.

From this point of view it is more appropriate to use some local method able to quantify the absorbing or reflecting properties of the metacomposite by restraining the analysis to the sole interface.

For example in the frequency domain the RIFF identification method seems to be very effective since it allows to identify the mechanical properties of the waveguide separating the effects due

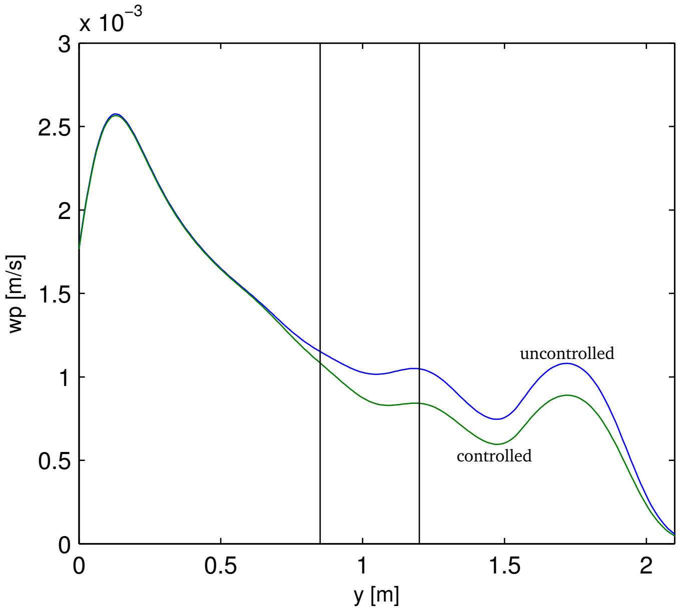

Figure 6.1: Spatial attenuation: uncontrolled system (blue line), controlled system (green line). The increase of the response observed in correspondence of 0.3 and 1.7 m is due to the boundaries reflections not filtered out by the used signal processing strategy.

to the surrounding environment. Similar results are obtained using an identification method based on the analysis of a time-varying wave-field propagating through the active interface.

Figure 6.1 present the results obtained using an identification method based on transient waves propagating along the smart waveguide. This method rely on the analysis of time varying waves modulated around a center frequency tuned at 3000 Hz (burst signal). The system response is recorded by means of a laser vibrometer. The obtained response is subsequently filtered in the wave-number domain in order to retain the sole flexural propagating term (S_0 Lamb wave). By means of an inverse Fourier transform the filtered signal is brought back in the spatial domain. This signal, having approximately the shape of a sinc function, is Hilbert transformed so as to obtain a bell shaped curve. The maximum of the response plotted as a function of the distance from the excitation source (y direction) provide an indication about the attenuation properties of the waveguide. In particular by comparing the uncontrolled (blue line) and the controlled (green line) responses it is clear that the external circuit is able to add a substantial amount of damping. This phenomenon is particularly evident once the wave crosses the active interface identified by two vertical lines. This method provides interesting results since it allows to evaluate the behavior of the waveguide to a multicomponent signal having a frequency content following a normal distribution. The drawback of the proposed method is the impossibility to filter out all the undesired wave components. For cylindrical waves it is possible to estimate the spatial attenuation by calculating the logarithmic decrement of the function relating the distance from the source and the level of the signal. Unfortunately this calculation can not be correctly performed since the measured response do not follow the expected response characterized by a $1/r$ decrement. For this reason further analysis must be done in order to avoid the problem related to parasitic terms which determine the response increase observed in Figure 6.1.

6.4 Conclusions & Future Works

This research has investigated the potential of the integrated electromechanical interface for the control of propagating waves. Effective vibration control capabilities have been illustrated through numerical models and experiments. The active interface metacomposite and its prototypes have attractive features which may be exploited for vibration mitigation in real-life applications. The smart metacomposite may be good candidates for industrial applications because of their hardware simplicity. In the field of aerospace structures, this device may be suitable for embedded installations on plate and shell-like structures, as wings and fuselages. They may be adopted both in reflecting and absorbing mode with the purpose of protecting some specific component from the surrounding environment or improve comfort for users.

However, much work is needed towards their practical implementation. In fact, the experiments performed in the laboratory were based on idealized setups and control system's performance evaluation on real structures is still required. Considerable work needs to be done to achieve in-service qualification of the active interface and associated hardware; other important issues to be addressed are discussed as follows.

The implementation of this smart interface on more complex structure represent a big challenge since it requires to overcome several technological difficulties. For example for curved surfaces, like the one depicted in Figure 6.2, the traditional piezoelectric ceramics are not adapted because of their inability to follow complex contour with varying curvature. In this case would be more appropriate the use *MFC* or piezoelectric polymers. However, the transition to this class of

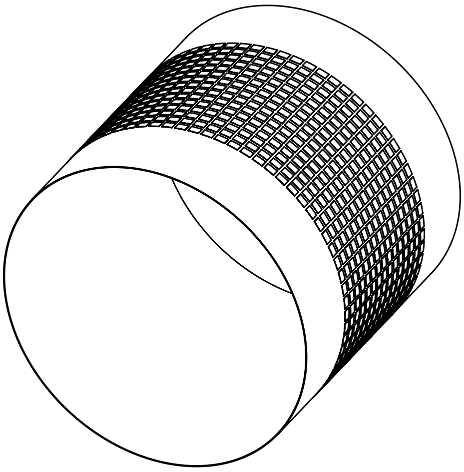

Figure 6.2: Periodic array of piezoelectric transducers installed on a cilyndrical structure.

material brings new questions such as: how much energy will be extracted by the active interface and will be available for the controlling system?

Moreover, to achieve a fully adaptable smart interface the analog circuit concept described in the previous chapter should be abandoned in favor of more flexible circuit based on micro-controller and digital circuits. The programming matter concept will be eventually achieved once the active interface will be able to modify some circuit parameters in response a variation occurring in the surrounding environment. The external circuit should be able to control not only one piezoelectric transducer at the time (co-localized solution) but also it should be able to control many other actuators in a clustered fashion so as to improve the performances at low frequencies. The integration of all the components in a embedded structure is achieved manufacturing electronic circuits at small scale over a printed board, this solution however requires a careful design of each subcomponent since a this scale the problem related to heat dissipation can create serious difficulties.

Of course all of these improvement can be more easily achieved if supported by an effective theoretical model able to correctly describe the main features of this complex structure. The Bloch theorem represent a good candidate for this purpose but several modification are required in order to describe more complex structures containing for example MFC actuators or complex electronic circuits. All this effort should converge toward a robust design of the structure including the uncertainties always present in such complex devices.

Appendix A

Miscellanea

A.1 Schematic of the Smart Metacomposite

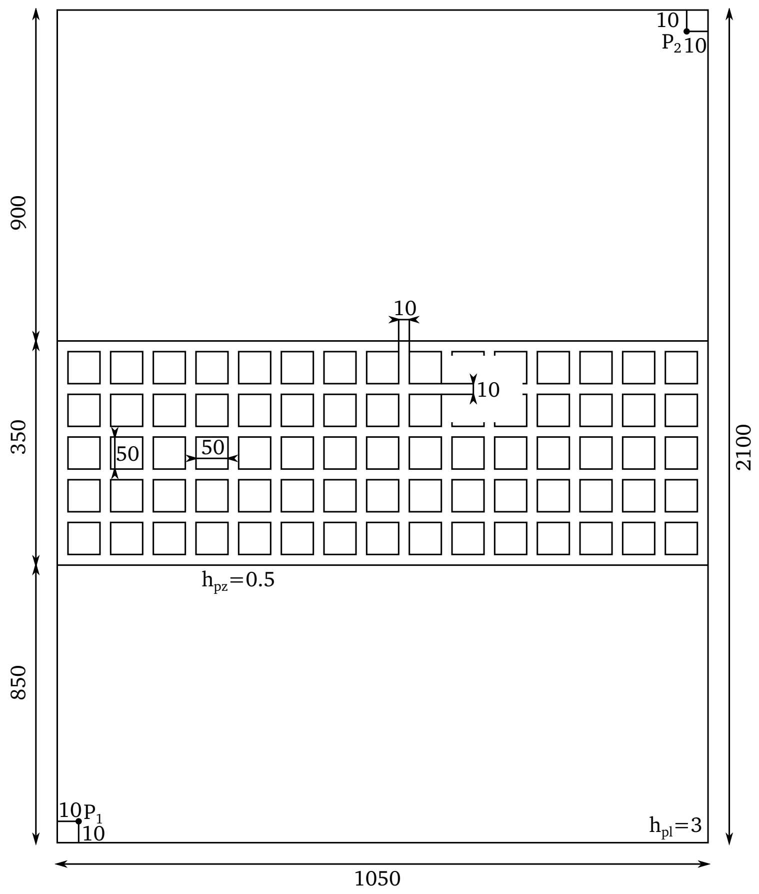

Figure A.1: Plate with periodic semidistributed set of cells (measures in mm).

A.2 Aluminum Properties

Parameters	Symbol	Units	Typical values
Young's modulus	E	N/m^2	$70 \cdot 10^9$
Density	ρ	kg/m^3	2700
Poisson's ratio	μ	-	0.33

Table A.1: Aluminum's properties.

A.3 Piezoelectric Ceramic Properties

Parameters	Symbol	Units	Typical values
Density	ρ	kg/m^3	7650
Poisson's ratio	μ	-	0.31
Dielectric constant	ϵ_{11}^S	-	1142
	ϵ_{33}^S	-	668
Voltage coefficients	e_{31}	C/m^2	-6.18
	e_{33}	C/m^2	12.79
	e_{15}	C/m^2	12.88
Elastic constants	C_{11}^E	GPa	153.7
	C_{12}^E	GPa	82.3
	C_{13}^E	GPa	80.6
	C_{33}^E	GPa	137.4
	C_{44}^E	GPa	45.9
	C_{66}^E	GPa	35.7

Table A.2: Piezoelectric ceramic's properties.

Bibliography

[1] J. Achenbach. *Wave propagation in elastic solids.* Elsevier, 1984.

[2] L. Airoldi and M. Ruzzene. Design of tunable acoustic metamaterials through periodic arrays of resonant shunted piezos. *New Journal of Physics*, 13(11):113010, 2011.

[3] L. Airoldi and M. Ruzzene. Wave propagation control in beams through periodic multi-branch shunts. *Journal of Intelligent Material Systems and Structures*, 22(14):1567–1579, 2011.

[4] G. Allaire and C. Conca. Bloch wave homogenization and spectral asymptotic analysis. *Journal de mathÃľmatiques pures et appliquÃľes*, 77(2):153–208, 1998.

[5] M. Ambati, N. Fang, C. Sun, and X. Zhang. Surface resonant states and superlensing in acoustic metamaterials. *Physical Review B*, 75(19):195447, 2007.

[6] N.W. Ashcroft and N.D. Mermin. *Solid state physics.* Harcourt College Publishers, 1976.

[7] B.A. Auld. *Acoustic fields and waves in solids.* Krieger, 1990.

[8] I. Bartoli, A. Marzani, F. Lanza di Scalea, and E. Viola. Modeling wave propagation in damped waveguides of arbitrary cross-section. *Journal of Sound and Vibration*, 295(3-5):685–707, 2006.

[9] W.T. Baumann, W.R. Saunders, and H.H. Robertshaw. Active suppression of acoustic radiation from impulsively excited structures. *The Journal of the Acoustical Society of America*, 90(6):3202–3208, 1991.

[10] B.S. Beck. *Negative capacitance shunting of piezoelectric patches for vibration control of continuous systems.* PhD thesis, Georgia Institute of Technology, 2012.

[11] B.S. Beck, K.A. Cunefare, M. Ruzzene, and M. Collet. Experimental analysis of a cantilever beam with a shunted piezoelectric periodic array. *Journal of Intelligent Material Systems and Structures*, 22(11):1177–1187, 2011.

[12] S. Behrens, A.J. Fleming, and S.O.R. Moheimani. A broadband controller for shunt piezoelectric damping of structural vibration. *Smart Materials and Structures*, 12(1):18, 2003.

[13] F. Bloch. Uber die quantenmechanik der elektronen in kristallgittern. *Zeitschrift fur Physik*, 52(7-8):555–600, 1929.

[14] Y.I. Bobrovnitskii. Some energy relations for mechanical systems. In F.J. Fahy and W.G. Price, editors, *IUTAM Symposium on Statistical Energy Analysis*, number 67 in Solid Mechanics and Its Applications, pages 37–46. Springer, 1999.

[15] Y.I. Bobrovnitskii. Conservation laws in vibration theory. *Doklady Physics*, 49(3):171–174, 2004.

[16] Y.I. Bobrovnitskii and M.P. Korotkov. Improved estimates for the energy characteristics of a vibrating elastic structure via the input impedance and mobility: experimental verification. *Journal of Sound and Vibration*, 247(4):683–702, 2001.

[17] A. Bocquillet, M.N. Ichchou, and L. Jezequel. Energetics of axisymmetric fluid-filled pipes up to high frequencies. *Journal of Fluids and Structures*, 17(4):491–510, 2003.

[18] M. Born and K. Huang. *Dynamical theory of crystal lattices.* Oxford University Press, 1988.

[19] L. Brillouin. *Wave propagation in periodic structures.* Dover, 1953.

[20] F. Casadei, B.S. Beck, K.A. Cunefare, and M. Ruzzene. Vibration control of plates through hybrid configurations of periodic piezoelectric shunts. *Journal of Intelligent Material Systems and Structures*, 23(10):1169–1177, 2012.

[21] F. Casadei, M. Ruzzene, L. Dozio, and K.A. Cunefare. Broadband vibration control through periodic arrays of resonant shunts: experimental investigation on plates. *Smart Materials and Structures*, 19(1):150, 2010.

[22] M. Castaings and M. Lowe. Finite element model for waves guided along solid systems of arbitrary section coupled to infinite solid media. *The Journal of the Acoustical Society of America*, 123(2):696–708, 2008.

[23] F. Chen and P.D. Wilcox. The effect of load on guided wave propagation. *Ultrasonics*, 47(1-4):111–122, 2007.

[24] S. Chen, G. Wang, J. Wen, and X. Wen. Wave propagation and attenuation in plates with periodic arrays of shunted piezo-patches. *Journal of Sound and Vibration*, 332(6):1520–1532, 2013.

[25] M. Collet, K.A. Cunefare, and M.N. Ichchou. Wave motion optimization in periodically distributed shunted piezocomposite beam structures. *Journal of Intelligent Material Systems and Structures*, 20(7):787–808, 2009.

[26] M. Collet, M. Ouisse, and M.N. Ichchou. Structural energy flow optimization through adaptive shunted piezoelectric metacomposites. *Journal of Intelligent Material Systems and Structures*, 23(15):1661–1677, 2012.

[27] M. Collet, M. Ouisse, M.N. Ichchou, and R. Ohayon. Semi-active optimization of 2D wave dispersion into shunted piezo-composite systems for controlling acoustic interaction. *Smart Materials and Structures*, 21(9):94, 2012.

[28] M. Collet, M. Ouisse, M. Ruzzene, and M.N. Ichchou. Floquet-bloch decomposition for the computation of dispersion of two-dimensional periodic, damped mechanical systems. *International Journal of Solids and Structures*, 48(20):2837–2848, 2011.

[29] C.J. Cross and S. Fleeter. Shunted piezoelectrics for passive control of turbomachine blading flow-induced vibrations. *Smart Materials and Structures*, 11(2):239, 2002.

[30] M. Date, M. Kutani, and S. Sakai. Electrically controlled elasticity utilizing piezoelectric coupling. *Journal of Applied Physics*, 87(2):863–868, 2000.

[31] B. de Marneffe and A. Preumont. Vibration damping with negative capacitance shunts: theory and experiment. *Smart Materials and Structures*, 17(3):350, 2008.

[32] F. dell'Isola, C. Maurini, and M. Porfiri. Passive damping of beam vibrations through distributed electric networks and piezoelectric transducers: prototype design and experimental validation. *Smart Materials and Structures*, 13(2):299, 2004.

[33] J.P. Den Hartog. *Mechanical Vibrations.* Dover Publications, 1985.

[34] N. Fang, D. Xi, J. Xu, M. Ambati, W. Srituravanich, C. Sun, and X. Zhang. Ultrasonic metamaterials with negative modulus. *Nature Materials*, 5(6):452–456, 2006.

[35] M. Farhat, S. Guenneau, and S. Enoch. Ultrabroadband elastic cloaking in thin plates. *Physical Review Letters*, 103(2):024301, 2009.

[36] A.J. Fleming, S. Behrens, and S.O.R. Moheimani. Synthetic impedance for implementation of piezoelectric shunt-damping circuits. *Electronics Letters*, 36(18):1525–1526, 2000.

[37] A.J. Fleming, S. Behrens, and S.O.R. Moheimani. An autonomous piezoelectric shunt damping system. *Smart Structures and Materials 2003*, 5052(6):207–216, 2003.

[38] A.J. Fleming and S.O.R. Moheimani. Improved current and charge amplifiers for driving piezoelectric loads, and issues in signal processing design for synthesis of shunt damping circuits. *Journal of Intelligent Materials Systems and Structures*, 15(2):77–92, 2004.

[39] G. Floquet. Sur les equations differentielles lineaires a coefficients periodiques. *Annales scientifiques de l' ENS*, 12(1):47–88, 1883.

[40] R.L. Forward. Electronic damping of vibrations in optical structures. *Applied Optics*, 18(5):690–697, 1979.

[41] E. Fukada, M. Date, K. Kimura, T. Okubo, H. Kodama, P. Mokry, and K. Yamamoto. Sound isolation by piezoelectric polymer films connected to negative capacitance circuits. *IEEE Transactions on Dielectrics and Electrical Insulation*, 11(2):328–333, 2004.

[42] P. Gardonio and S.J. Elliott. Smart panels for active structural acoustic control. *Smart Materials and Structures*, 13(6):1314–1336, 2004.

[43] L. Gavric. Computation of propagative waves in free rail using a finite element technique. *Journal of Sound and Vibration*, 185(3):531–543, 1995.

[44] K.F. Graff. *Wave motion in elastic solids.* Dover Publications, 1991.

[45] N.W. Hagood and A. von Flotow. Damping of structural vibrations with piezoelectric materials and passive electrical networks. *Journal of Sound and Vibration*, 146(2):243–268, 1991.

[46] J.J. Hollkamp. Multimodal passive vibration suppression with piezoelectric materials and resonant shunts. *Journal of Intelligent Material Systems and Structures*, 5(1):49–57, 1994.

[47] L. Houillon, M.N. Ichchou, and L. Jezequel. Wave motion in thin-walled structures. *Journal of Sound and Vibration*, 281(3-5):483–507, 2005.

[48] X. Hu, C.T. Chan, and J. Zi. Two-dimensional sonic crystals with helmholtz resonators. *Physical Review E*, 71(5):556, 2005.

[49] T.L. Huang, M.N. Ichchou, O.A. Bareille, M. Collet, and M. Ouisse. Traveling wave control in thin-walled structures through shunted piezoelectric patches. *Mechanical Systems and Signal Processing*, 39(1-2):59–79, 2013.

[50] T.J.R. Hughes. *The finite element method linear static and dynamic finite element analysis.* Dover Publications, 2000.

[51] J.B. Hunt and J.C. Nissen. The broadband dynamic vibration absorber. *Journal of Sound and Vibration*, 83(4):573–578, 1982.

[52] M.N. Ichchou, S. Akrout, and J.M. Mencik. Guided waves group and energy velocities via finite elements. *Journal of Sound and Vibration*, 305(4-5):931–944, 2007.

[53] J.D. Joannopoulos, S.G. Johnson, J.N. Winn, and R.D. Meade. *Photonic crystals: molding the flow of light.* Princeton University Press, 2008.

[54] J. Kim and Y.C. Jung. Broadband noise reduction of piezoelectric smart panel featuring negative-capacitive-converter shunt circuit. *The Journal of the Acoustical Society of America*, 120(4):2017–2025, 2006.

[55] C. Kittel. *Introduction to solid state physics.* Wiley, 2005.

[56] R.S. Lakes, T. Lee, A. Bersie, and Y.C. Wang. Extreme damping in composite materials with negative-stiffness inclusions. *Nature*, 410(6828):565–567, 2001.

[57] R.S. Langley. The response of two-dimensional periodic structures to point harmonic forcing. *Journal of Sound and Vibration*, 197(4):447–469, 1996.

[58] Z. Liu, X. Zhang, Y. Mao, Y.Y. Zhu, Z. Yang, C.T. Chan, and P. Sheng. Locally resonant sonic materials. *Science*, 289(5485):1734–1736, 2000.

[59] S. Livet, M. Collet, M. Berthillier, J. Pierrick, and J.M. Cote. Structural multi-modal damping by optimizing shunted piezoelectric transducers. *European Journal of Computational Mechanics*, 20(1-4):73–102, 2011.

[60] M.P. Marder. *Condensed matter physics*. Wiley, 2010.

[61] A. Marzani, E. Viola, I. Bartoli, F. Lanza di Scalea, and P. Rizzo. A semi-analytical finite element formulation for modeling stress wave propagation in axisymmetric damped waveguides. *Journal of Sound and Vibration*, 318(3):488–505, 2008.

[62] W. Maysenholder. *Korperschallenergie*. Hirzel, 1994.

[63] D.J. Mead. A general theory of harmonic wave propagation in linear periodic systems with multiple coupling. *Journal of Sound and Vibration*, 27(2):235–260, 1973.

[64] J.M. Mencik and M.N. Ichchou. Multi-mode propagation and diffusion in structures through finite elements. *European Journal of Mechanics - A/Solids*, 24(5):877–898, 2005.

[65] J.M. Mencik and M.N. Ichchou. Wave finite elements in guided elastodynamics with internal fluid. *International Journal of Solids and Structures*, 44(7-8):2148–2167, 2007.

[66] S.O.R. Moheimani, A.J. Fleming, and S. Behrens. On the feedback structure of wideband piezoelectric shunt damping systems. *Smart Materials and Structures*, 12(1):49, 2003.

[67] S.O.R. Moheimani, A.J. Fleming, and S. Behrens. Dynamics, stability, and control of multivariable piezoelectric shunts. *IEEE/ASME Transactions on Mechatronics*, 9(1):87–99, 2004.

[68] F.R. Montero de Espinosa, E. Jimenez, and M. Torres. Ultrasonic band gap in a periodic two-dimensional composite. *Physical Review Letters*, 80(6):1208–1211, 1998.

[69] A.B. Movchan, N.V. Movchan, and S. Haq. Localised vibration modes and stop bands for continuous and discrete periodic structures. *Materials Science and Engineering: A*, 431(1-2):175–183, 2006.

[70] D. Niederberger, A. Fleming, S.O.R. Moheimani, and M. Morari. Adaptive multi-mode resonant piezoelectric shunt damping. *Smart Materials and Structures*, 13(5):1025, 2004.

[71] G. Papanicolau, A. Bensoussan, and J.L. Lions. *Asymptotic Analysis for Periodic Structures.* Elsevier, 1978.

[72] C.H. Park and A. Baz. Vibration control of beams with negative capacitive shunting of interdigital electrode piezoceramics. *Journal of Vibration and Control*, 11(3):331–346, 2005.

[73] E. Plum, J. Zhou, J. Dong, V.A. Fedotov, T. Koschny, C.M. Soukoulis, and N.I. Zheludev. Metamaterial with negative index due to chirality. *Physical Review B*, 79(3):035407, 2009.

[74] A. Preumont, J.P. Dufour, and C. Malekian. Active damping by a local force feedback with piezoelectric actuators. *Journal of Guidance, Control, and Dynamics*, 15(2):390–395, 1992.

[75] R. Rana and T.T. Soong. Parametric study and simplified design of tuned mass dampers. *Engineering Structures*, 20(3):193–204, 1998.

[76] M.C. Ray and A. Baz. Optimization of energy dissipation of active constrained layer damping treatments of plates. *Journal of Sound and Vibration*, 208(3):391–406, 1997.

[77] D. Royer and E. Dieulesaint. *Elastic waves in solids.* Springer, 2000.

[78] M. Ruzzene and F. Scarpa. Directional and band-gap behavior of periodic auxetic lattices. *physica status solidi (b)*, 242(3):665–680, 2005.

[79] M. Ruzzene, F. Scarpa, and F. Soranna. Wave beaming effects in two-dimensional cellular structures. *Smart Materials and Structures*, 12(3):363, 2003.

[80] M. Senesi, B. Xu, and M. Ruzzene. Experimental characterization of periodic frequency-steerable arrays for structural health monitoring. *Smart Materials and Structures*, 19(5):055026, 2010.

[81] T.T. Soong, A.M. Reinhorn, S. Aizawa, and M. Higashino. Recent structural applications of active control technology. *Journal of Structural Control*, 1(1-2):1–21, 1994.

[82] A. Spadoni, M. Ruzzene, and K.A. Cunefare. Vibration and wave propagation control of plates with periodic arrays of shunted piezoelectric patches. *Journal of Intelligent Material Systems and Structures*, 20(8):979–990, 2009.

[83] A. Spadoni, M. Ruzzene, S. Gonella, and F. Scarpa. Phononic properties of hexagonal chiral lattices. *Wave Motion*, 46(7):435–450, 2009.

[84] A. Sukhovich, L. Jing, and J.H. Page. Negative refraction and focusing of ultrasound in two-dimensional phononic crystals. *Physical Review B*, 77(1):014301, 2008.

[85] J. Tang and K.W. Wang. Active-passive hybrid piezoelectric networks for vibration control: comparisons and improvement. *Smart Materials and Structures*, 10(4):794, 2001.

[86] O. Thorp, M. Ruzzene, and A. Baz. Attenuation and localization of wave propagation in rods with periodic shunted piezoelectric patches. *Smart Materials and Structures*, 10(5):979, 2001.

[87] O. Thorp, M. Ruzzene, and A. Baz. Attenuation of wave propagation in fluid-loaded shells with periodic shunted piezoelectric rings. *Smart Materials and Structures*, 14(4):594, 2005.

[88] T. Toffoli and N. Margolus. Programmable matter: Concepts and realization. *Physica D: Nonlinear Phenomena*, 47(1-2):263–272, 1991.

[89] J.P. Wolfe. *Imaging Phonons: Acoustic Wave Propagation in Solids*. Cambridge University Press, 2005.

[90] S. Yang, J.H. Page, Z. Liu, M.L. Cowan, C.T. Chan, and P. Sheng. Ultrasound tunneling through 3D phononic crystals. *Physical Review Letters*, 88(10):104301, 2002.

Résumé:

Le domaine des matériaux intelligents et des structures adaptatives constitue un domaine de recherche consacré à la conception de structures architecturées ayant la faculté de modifier leur comportement en réponse à un stimulus externe.

Le travail proposé dans cette thèse porte sur l'analyse et la conception d'un système pour le contrôle vibroacoustique adaptatif. Il s'attache à la conception d'une interface active faite de transducteurs piézo-électriques disposés en réseau bidimensionnel. Chaque transducteur est shunté individuellement par un circuit électronique externe synthétisant une capacité negative. Cette stratégie de contrôle se base sur le couplage multipysique entre la plaque et les circuit électroniques mis en communication et permet de contrôler les ondes se propageant au sein de la structure. Le dispositif ainsi créé est qualifié de métacomposite.

La performance du metacomposite a été évaluée par le biais de nombreux essais numériques et expérimentales. Du point de vue modélisation, l'analyse a été réalisée à l'aide du théorème de Bloch adapté aux systèmes piézo-élastiques à deux dimensions. Par la suite, une procédure d'optimisation a été utilisée dans le but de sélectionner les paramètres de shunt électrique les plus appropriés.

Un prototype du guide d'ondes a été fabriqué et testé. Les résultats montrent clairement que ce dispositif permet de modifier les propriétés vibratoires de la structure porteuse, que ce soit en terme d'atténuation ou de trasmission.

Enfin, un modèle éléments finis de la plaque a été utiliser afin d'évaluer la robustesse de la stratégie de contrôle proposée vis-à-vis d'une modification des paramètres du circuit, de la topologie de l'interface active ou des propriétés de la plaque contrôlée.

Mots clés: métacomposites, structures périodiques, propagation d'ondes en milieux complexes, matériaux intelligents, contrôle vibratoire.

Abstract:

Smart materials is an active research area devoted to the design of structured materials showing physical properties that can be modified in response to an external stimulus.

This study focuses on the analysis and design of adaptive system for vibroacoustic control. The research investigates the design of a active interface made of piezoelectric transducers arranged in a two-dimensional lattice. Each transducer is individually shunted to an external electric circuit synthesizing a negative capacitance effect. It allows to control waves propagating inside a structure taking advantage of the multi-field coupling between the structural plate and the electrical circuits shunting the piezoelectric patches.

The performance of the metacomposite has been evaluated through numerous numerical and experimental tests. The smart wave-guide has been analyzed by using the Bloch theorem applied to two-dimensional piezo-elastic systems. Subsequently an optimization procedure has been used with the purpose to select the most appropriate set of circuit's parameters.

A prototype of the smart waveguide has been manufactured and tested. The results results clearly show the filtering and attenuating capabilities of this device.

Finally a finite element model of the finite extent smart plate has been considered in order to asses the robustness of the proposed control strategy respect to a modification of the circuit's parameters, the topology of the active interface and the properties of the controlled plate.

A brief review conclude the work delineating which aspects of the design should be modified in order to obtain a device suitable for industrial applications.

Keywords: metacomposites, periodic structures, wave propagation in complex media, smart materials, vibration control.

■ Ecole doctorale SPIM 16 route de Gray F - 25030 Besancon cedex

■ tel. +33 (0) 3 81 66 66 02 ■ ed-spim@univ-fcomte.fr ■ www.ed-spim.univ-fcomte.fr